1-1-2010

# Two Particle Correlations And The Ridge In Relativistic Heavy Ion Collisions

George Stevens Moschelli
*Wayne State University*

# TWO-PARTICLE CORRELATIONS AND THE RIDGE IN RELATIVISTIC HEAVY ION COLLISIONS

by

**GEORGE MOSCHELLI**

**DISSERTATION**

Submitted to the Graduate School

of Wayne State University,

Detroit, Michigan

in partial fulfillment of the requirements

for the degree of

**DOCTOR OF PHILOSOPHY**

2010

Major: PHYSICS

Approved by:

_____

Advisor Date

_____

_____

_____

## DEDICATION

*For my family, from whose examples of fortitude and devotion,*

*a son and brother can learn to examine the world.*

## ACKNOWLEDGEMENTS

There is a necessity for mentors and pupils to have a relationship built on a desire to attain professional goals. Special gratitude should go to those whose character naturally drives them beyond mere professionalism. First and foremost, not just because of his position as my adviser where he has shaped my intuition and understanding of physics, but Sean Gavin deserves first mention because his influence is limited only to those who have not walked past his door. I believe his concern for my future goes beyond that of a mentor. I would also like to acknowledge Rene Bellwied who has supported my career, though it is not his obligation. J.S. Payson also deserves credit for much advice during my term as a teaching assistant when I was a beginning graduate student.

No less thanks should go to Claude Pruneau, and Alexey Petrov who have influenced both my education and research. I thank all of the WSU Heavy-Ion and High-Energy groups for discussions, guidance, and support.

Many thanks go to the other students and postdocs with whom I have shared and learned with during our time at WSU. particularly Ron Tackett, Sarah LaPointe, and Muhammad Elnimr who started the journey with me, Rajendra Pokarehl and Mike Catanzaro, who I have worked along side and shared many fun moments, Anthony Timmins who has introduced me to many new friends and colleagues as well as provided much provisions, Andrew Blechman for introducing the "W Friday" tradition, as well as Larry Tarini, Monika Sharma, and Chanaka DeSilva.

The support staff also deserve mention. They take care of all of the grad students in ways not commonly recognized. For their helpfulness to me over the years, I would like to thank Deloris Cowen, Marquia Ziyad, and Wynell Pitts.

The character of the department is well displayed by the sense of community

extending from staff, undergraduates, graduates and professors alike. This has atmosphere has grown considerably during my time as a graduate student and I will surly miss and remember it fondly.

I have been fortunate enough to have too many colleagues and examples of professionalism to thank individually. This work is not without your influence. Finally, special thanks go to my family and friends – you are the most important people in my life.

*Still it came passing by*
*The pieces weaved together rose the sun*
*And fooled me with another day*
*The knocking message called for my life*
$\sim$ *Opeth*

## TABLE OF CONTENTS

## LIST OF FIGURES

# Chapter 1

# Introduction

Correlation measurements have played an integral role in the most exciting discoveries at the Brookhaven Relativistic Heavy Ion Collider (RHIC) [9, 30, 31, 32]. Correlation measurements teach us how the particles produced in a high energy collision influence each other. RHIC correlation measurements such as flow and jet quenching, have demonstrated that these interactions are extremely strong, perhaps as strong as possible. The success of these measurements has inspired other correlation studies such as forward-backward correlations [33, 34, 35], and the so-called "ridge".

We begin with a motivation for ridge related studies, a description of ridge features, and general concepts behind the ridge formation. We then provide a general background to relativistic heavy ion collisions in Ch. 2, and theoretical backgrounds of the effects of flow and freeze out and the initial state of the collisions in Ch. 3 and Ch. 4 respectively. In Ch. 5 we follow Refs.[36, 37] and detail our theoretical description of specific ridge features highlighting the long rang behavior and importance of our choice of particle production mechanism. We extend this framework in Ch. 6 to discriminate between different ridge measurements and show they all result from the same phenomenon. Chapter 7 adds insight into the shape of the ridge based on the effects of viscous diffusion and focuses on changes in freeze out conditions related to viscosity [38, 39]. Finally in Ch. 8 and 9 we discuss aspects of the ridge not addressed

in this work and summarize our results.

## 1.1 Motivation

A range of measurements indicate that relativistic heavy ion collisions produce a fluid that flows collectively, see Ref [40] for recent review. In particular, elliptic flow measurements are described at the 10% level by hydrodynamics. This implies that the fluid is very nearly that of an ideal (viscosity-free) liquid. In this sense the collective interactions are as strong as possible.

One observes elliptic flow with a two particle correlation measurement [40]. A comparison of hadron momenta shows an asymmetry in the azimuthal distribution of final state particles in off-center, peripheral collisions. In head on, central collisions, particle momenta are, on average, uniform in all directions; the azimuthal distribution is circular. In peripheral collisions, however, the azimuthal distribution is football shaped. The famous result is that this asymmetry is correlated to the geometry of the colliding nuclei, and that as collisions become more peripheral, this effect increases.

Jet quenching measurements demonstrate that the fluid medium influences jet production [7, 41, 42, 43, 44]. Naively, perturbative Quantum Chromodynamics (pQCD) would suggest that such effects should be very small. Specifically, the factorization theorem of pQCD implies that any effect of the medium on the inclusive cross section for $AA \to jet + X$ be small and vanish as $p_t \to \infty$ [45, 46, 47]. Correlation measurements escape this restriction.

Jet quenching is also observed with a two particle correlation measurement. Here the momentum of a high $p_t$ trigger particle is compared with the momenta of particles in an associated $p_t$ range - the supposed $p_t$ range of jet fragments [41, 42, 43, 44, 7]. At small azimuthal angular differences, on the "same side" as the leading jet particle, measurements find particles with momenta in a similar direction as the jet in excess of the background. However, similar correlations with particles $\sim 180^\circ$ are missing

or suppressed. This is unique to heavy ion collisions where, unlike in proton-proton (p+p) collisions, the momentum conserving "away side" jet must pass through and is quenched by the comparatively large and dense medium.

If the medium influences jet production, one can then ask to what extent the jets influence the medium. This has been much harder to demonstrate. The search for the jets' impact on the medium inspired a range of correlations studies such as the (hard) ridge.

Separate ridge measurements highlight different aspects of heavy ion collisions including medium response to a high $p_t$ trigger [2, 3, 4, 5, 48, 49, 50], bulk medium evolution [1, 26, 51], and the $p_t$ dependent evolution of the system [28, 52, 53, 54, 55]. We call the first the "hard ridge" due to its examination of particle pairs selected by a high $p_t$ trigger and lower $p_t$ associates also in a "hard" region of the particle spectrum. The latter two untriggered measurements fall in the category of the "soft ridge" since all possible particle pairs contribute; this measurement is made with and without $p_t$ weighting of correlated pairs. All ridge measurements indicate that two particle correlations extend to a long range in relative (pseudo)rapidity. Understanding this phenomenon is one of the primary goals of this work, and requires study of both the initial conditions of the collision and the following evolutionary dynamics.

To study the response to the medium to the passage of jets, correlation measurements compare both azimuthal and longitudinal distributions of momentum. After accounting for expected sources of correlation including elliptic flow, jet fragmentation, and global momentum conservation, an excess correlation structure remains. These unexplained excess correlations are important because they can provide additional insight to the connection between the initial state of the collision and the dynamics and modifications to the produced medium. Such measurements comparing the relative momentum differences of all possible pairs of produced hadrons find the striking result that excess correlations exist over large separation in (pseudo)rapidity.

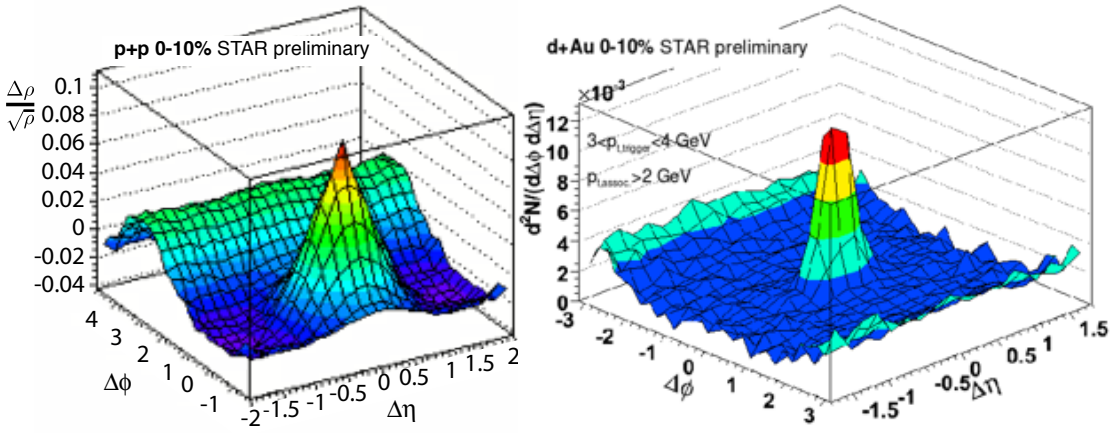


Figure 1.1: Two particle correlation measurements for Left: p+p (Soft Ridge) [1], and Right: central d+Au (Hard Ridge) [2].

These long range correlations are exciting because causality limits the interactions of partons to $\sim 1-2$ rapidity units, meaning correlations beyond this limit must result from correlations at the point of particle production rather than from kinematic transport.

## 1.2 Description of Ridge Features

Two particle correlation measurements such as the ridge examine the distribution of final state particle pairs by counting the number of pairs with the same azimuthal separation $\phi = \phi_1 - \phi_2$ and same (pseudo)rapidity separation $\eta = \eta_1 - \eta_2$. As shown in Fig. 1.1, in p+p, deuteron-gold (d+Au), and very peripheral gold-gold (Au+Au) collisions, these measurements find a "near side" peak centered at $\phi = \eta = 0$ that is similarly narrow in both $\phi$ and $\eta$. This peak is representative of the columniation in the spray of particles coming from jet fragmentation. The momenta of these particles point in the direction of the leading jet particle, meaning the jet fragments have small $\phi$ and $\eta$ separations. The "away side" structure, centered at $\phi = \pi$, appears flat in $\eta$. This structure is due momentum conservation and longitudinal asymmetry of jet

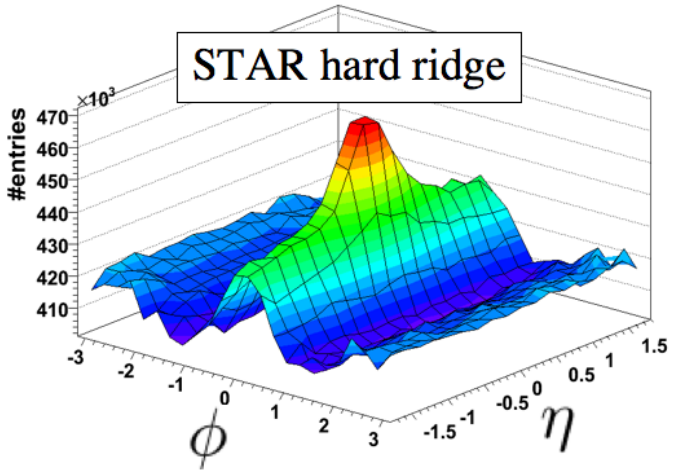


Figure 1.2: STAR hard ridge, Au+Au, 200 GeV, $0-10\%$ central [3]. The "*#entries*" on the vertical axis represents the yield of correlated pairs per jet trigger, with the trigger in the range $3 < p_{t,trigg} < 4$ GeV and paired with a particle in the associated range $2 < p_{t,assoc} < 3$

locations.

The triggered hard ridge measures the correlated yield of associates per jet trigger, $(1/N_{trig})dN/d\phi d\eta$. The intention is to isolate jet effects by specifically examining correlations of trigger particles in a high $p_t$ range with associated particles in a lower $p_t$ range. Conversely, the untriggered soft ridge measurement studies all possible particle pairs $\Delta\rho(\phi,\eta)/\sqrt{\rho_{ref}} = (\rho_{sib} - \rho_{ref})/\sqrt{\rho_{ref}}$ where $\rho_{sib}$ is the distribution of particle pairs from the same event and $\rho_{ref}$ is the distribution of particle pairs from mixed events. Although these measurements are related, the observables are not directly comparable; understanding this relationship is one of the goals of this thesis.

In Au+Au collisions, jets are expected to modify the hot dense medium. Therefore, one might expect to find a change in the 2-D $(\phi,\eta)$ correlation structure. Perhaps such changes would provide clues into the mechanism causing jet energy loss and a quantification of the modification to the medium.

The near side jet-triggered correlation structure for central Au+Au collisions is shown in Fig. 1.2. A jet peak near $\eta = \phi = 0$ likely consists of particles from the fragmenting jet trigger, assuming the high $p_t$ trigger particle is indeed from a jet. The

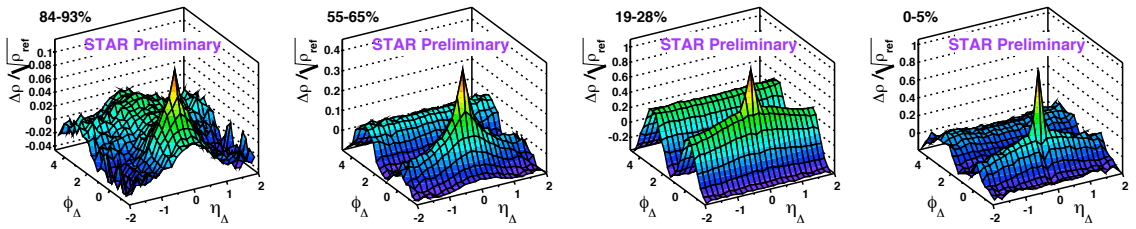


Figure 1.3: Minimum-bias soft ridge correlations for several centralities from peripheral (left) to central (right) in 200 GeV Au+Au collisions from [1].

hard ridge appears in Au+Au collisions as a pedestal-like enhancement of the yield at small $\phi$ under the jet peak. The ridge is much wider in $\eta$ than the jet peak and is absent from d+Au collisions.

This pedestal is broad and seemingly flat in $\eta$ but shares the same narrow $\phi$ profile as the jet peak. This structure gains the title of "the ridge" because of its resemblance to a mountain ridge. The further designation of "hard ridge" refers to its examination of jets which come from "hard" scatterings. The striking and unexpected feature of the STAR hard ridge is that correlations of high $p_t$ particles with a jet trigger extend up to 2 units in rapidity (the entire STAR acceptance). The main question here is, if the jet somehow induces correlations with the medium during its passage, how large is this effect, and how far in rapidity does it reach? To answer this question one can study the correlation structure from the medium itself, without the isolation of high $p_t$ particles.

STAR also makes separate correlation measurements without a jet trigger. Unlike the hard ridge measurement, correlations of all possible pairs of particles with any $p_t$ show a similar 2-D correlation structure. Like the hard ridge, the soft ridge has a near side peak centered at $\phi = \eta = 0$ that is narrow in $\phi$ and broad in $\eta$. The soft and hard ridges have been considered separate phenomenon because of the difference in the dominant particle production mechanisms in the two $p_t$ regimes.

The momentum spectrum in relativistic Au+Au collisions seems to follow a power law past $\sim 2GeV$ which is described nicely by jet production. Not coincidently, the

minimum momentum of associated particles in the hard ridge measurement is taken to be 2 GeV. However, more than 99% of all the particles produced in these collisions are in the soft or bulk region (below 2 GeV). Particles in this range are primarily thermal and well described by hydrodynamics in Au+Au collisions [9, 30, 31, 32]. Correlations amongst these particles resembling those of the hard ridge suggests that the ridge shape is a general feature of heavy ion collisions rather than a modification of that system.

The exploration of the possible relationship between the two ridges is another goal of this thesis. In particular, we focus on the azimuthal width and amplitude of the ridge, away from the jet peak. Fig. 1.3 shows the soft ridge in 200 GeV Au+Au collisions for selected centrality cuts. Notice that in peripheral collisions (left most graph in Fig. 1.3), the correlations structure resembles that in p+p (left graph in Fig. 1.1). As the centrality increases the ridge appears and becomes more prominent.

The azimuthal width of the soft ridge in Fig. 1.3 remains roughly constant with centrality, at about $\sigma_r \sim 0.7$. In comparison, the hard ridge is much narrower at about $\sigma_r \sim 0.3$. The amplitude of the hard ridge is also considerably less than the soft ridge. Naively one would expect this since the number of possible pairs contributing to the hard ridge comes from 1% of the total multiplicity and the soft ridge examines all particle pairs. For this reason, in the soft ridge, the jet peak would be overwhelmed by correlations from bulk pairs. Although the observables are different, it should be possible to examine the emergence of a hard ridge-like jet peak in the soft ridge through the implementation of appropriate $p_t$ cuts [26].

The PHOBOS measurement of the ridge (Fig. 1.4) finds the most interesting and most discriminating feature, as it extends to a range as large as $-4 < \eta < 2$ [4, 5]. Correlations existing over a causally disconnected range must then arise at the earliest stage of the collision when the first partons are produced [25, 36]. Therefore, fluctuations in the initial conditions of heavy ion collisions directly impact the shape

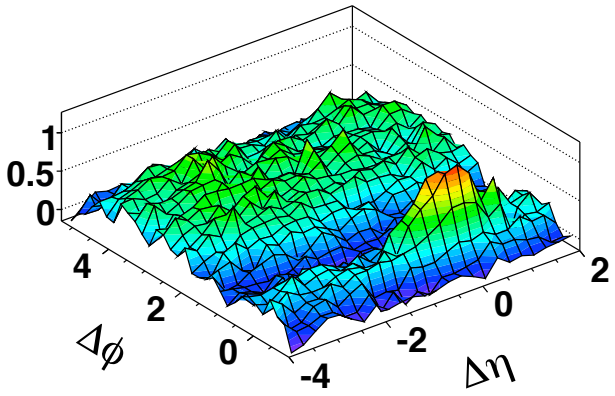


Figure 1.4: Per-trigger correlated yield with $p_T^{trig} > 2.5$ GeV/c as a function of $\Delta\eta$ and $\Delta\phi$ for 200 GeV PHOBOS Au+Au collisions [4, 5].

of the ridge.

## 1.3 The Ridge from Fluctuations and Flow

In this dissertation, we propose an explanation for the soft ridge based on fluctuating initial conditions and later stage transverse flow. Particles produced in a common local region share an initial spatial correlation based on the fact that they were produced within that same density fluctuation. Taking each fluctuation as a fluid cell with small transverse size comparative to the nuclear overlap region, the following dynamical evolution will have approximately the same effect on all particles in the cell.

The amount of work done on a fluid cell then depends on the pressure gradient of the system inside the radial position of the cell. In other words, transverse flow radially boosts all particles in the fluid cell depending on the initial radial position of the cell. Since the $p_t$ of particles coming from the same fluctuation is related to their common origin, the initial state spatial correlation then translates into a final state momentum correlation.

Furthermore, to obtain long range rapidity correlations, fluctuations must extend

over a large longitudinal region. This relies on both the Bjorken expansion assumption that links soft particle rapidity to longitudinal position, and a source of fluctuations that is uniform over a large longitudinal distance and has small transverse size.

Almost instantaneously after a collision of two nuclei, Color Glass Condensate (CGC) theory predicts that the transverse fields of each nucleus are transformed into longitudinal fields that are approximately uniform in rapidity [56, 57, 58]. The fields, which are random over transverse distances larger than $Q_s^{-1}$ where $Q_s \sim 1 - 2$ GeV is the saturation scale, comprise a series of flux tubes. Given a dense distribution of flux tubes, the system enters a "Glasma" pre-thermalization phase as the tubes evaporate into particles. The Glasma description describes many features of the matter produced in the high density environment produced in nuclear collisions, and allows for a systematic weak coupling computation. The contribution of flux tubes to long range correlations is studied in the Glasma formulation in [25, 36, 37, 59].

We take CGC flux tubes as the source of the fluctuations that produce the soft ridge. The Glasma scenario provides a distribution of tubes and gluon density per tube which allows for a quantative comparison to the change in ridge amplitude. Ours is one of a family of models in which particles are initially correlated at the point of production [25, 60, 61, 62, 63, 64, 65]. Long range rapidity correlations arise because flux tubes stretch between the two nuclei and particles from the same flux tube start at nearly the same transverse position, regardless of rapidity. Flow then boosts the correlated particles into a small opening angle in $\phi$. Flow models have also been used to describe qualitative features of the hard ridge [65], [66].

The hard ridge has most commonly been described as a consequence of the jet passing through the flowing bulk matter produced by the nuclear collision [67, 68, 69, 70, 71, 72, 73, 74, 75, 76, 77]. While in principle jets and minijets may contribute to the soft ridge [78], the overwhelming success of hydrodynamics at low $p_t$ suggests both effects play a role. Of particular interest in this regard is work by Shuryak in

which jet quenching and transverse flow of the bulk play a combined role [79]. Jet quenching produces a near side bias by suppressing the away side jet. Near side jet particles are then correlated with other particles from the same jet or transversely flowing bulk particles.

We propose that the near side of both hard and soft ridges arise as a consequence of primarily the same phenomena. Long range correlations arise as a consequence of initially long color flux tubes that provide particle density fluctuations which feel later stage transverse flow.

# Chapter 2

## Background

High energy particle and nuclear physics are fields devoted to the understanding of nature at its most fundamental level. The most basic questions include: What are the smallest building blocks of nature, what are their physical characteristics, and how do they interact to form the matter we observe? Despite their simplicity, it is no trivial matter to answer these questions. Our current understanding of these questions is addressed in the Standard Model [80] as described by Quantum Chromo-Dynamics (QCD), the strong force corollary to Quantum Electro-Dynamics (QED).

Normal matter is made of elements which are categorized on the Periodic Table. We understand individual elements as atoms with specific configurations of nuclei orbited by electrons. An element is defined by the number of protons in its nucleus. The lightest element, Hydrogen, has one nucleon, the proton, where Gold has, on average, 197 nucleons (79 protons and 118 neutrons). Already we have described nature at three very different size scales that vary by many orders of magnitude, see Fig.2.1. The radius of a Gold atom is $144pm$, but its nuclear radius is $\sim 6.38fm$ and the radius of a proton is $\sim 1fm$. Comparably, the electron size is $\sim 10^{-3}fm$.

Scattering is a common technique for determining the size of such forms of matter. In particular, one can scatter electrons from a target, and determine its size from the defraction pattern. Deep Inelastic Scattering (DIS) experiments have shown that the proton is not the smallest particle in the nucleus. Scatterings of electrons on protons

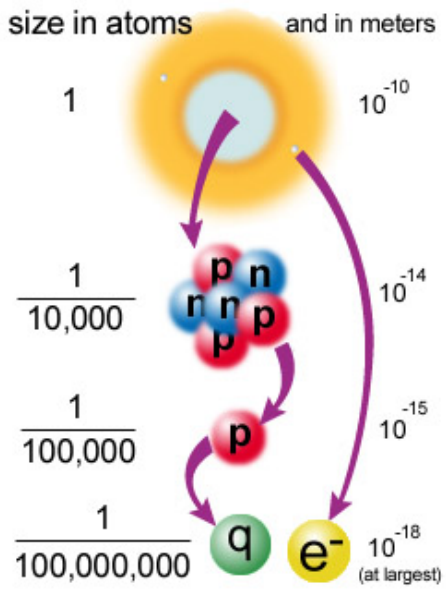


Figure 2.1: Size scales of sub-atomic particles.

show three scattering centers inside the proton, quarks. Free quarks, however, have not been observed and are confined to hadrons. QCD predicts that the coupling strength between quarks asymptotically falls to zero with increase in the energy of the interaction between quarks. This phenomenon is known as asymptotic freedom.

The motivation behind nuclear collisions is to take advantage of asymptotic freedom and create a system with energy density high enough that quarks move freely within the system. RHIC collides Gold nuclei with a maximum center of mass energy of 200 GeV per nucleon. The resulting system has an energy density nearly 30 times that of a proton, an order of magnitude greater than that in a neutron star. The system evolves over $\sim 20 fm/c$, where $c$ is the speed of light, a time scale expected to be long enough that the quarks and gluons thermalize into a new form of matter, the Quark-Gluon Plasma (QGP). The primary goal of experiments at RHIC has been to gather evidence for the existence of QGP and characterize its physical attributes. The goals of this thesis fall along the same lines through the use phenomenological attributes of the QGP along with theories of the initial state of the collision to explain

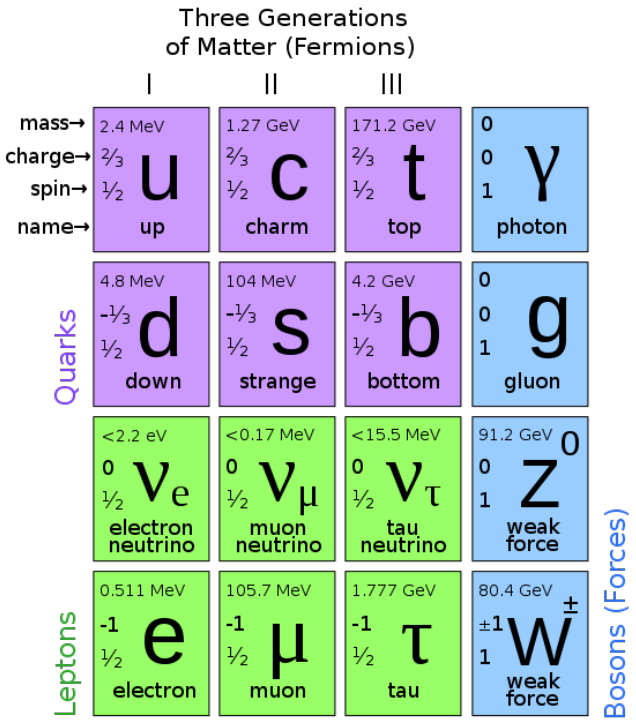


Figure 2.2: Table of standard model particles. Image source: Fermilab, Office of Science

current measurements.

## 2.1 The Standard Model and QCD

The Standard Model is a description of our current understanding of the most elementary particles that make up the universe and their interactions. Fig.2.2 categorizes these particles and lists some attributes. We see that we are already familiar with some of these particles, namely the electron and the photon. The electromagnetic interactions of these particles has been understood for hundreds of years, but the more recent understanding of these particles in terms of quantum field theory that has provided the basis for the Standard Model.

QED describes the electromagnetic force acting on electrically charged particles as mediated by the photon. This knowledge comes in part from understanding the quantum numbers of elementary particles, such as charge and spin. The electron is

a Fermion with spin 1/2 and charge $-1$ where the photon is a massless Boson with spin 1 and no charge. Like the photon, there are other force carrying Bosons that mediate the weak and strong forces. For the weak force, there are the $W^{\pm}$ and the $Z^0$, and for the strong force, there is the gluon.

The weak force, along with the electromagnetic force, describes all interactions between leptons. This is symptomatic of the result that, at interaction energies on the order of 100 GeV, the two forces unify. There are other leptons, the muon and the tau, that like the electron, have charge $-1$ and spin 1/2, but different masses. Additionally there are three more leptons called neutrinos - one associated with each of the electron, muon, and tau. They are spin 1/2, have zero charge, and are massless in electroweak theory but are seen to have small experimental mass.

Quarks make up the final class in the standard model. They not only feel the electroweak force described by the $SU(2) \times U(1)$ gauge group, but also the strong $SU(3)$ gauge group. The $SU(3)$ group is determined by interactions of the (strong) color charges. In addition to the positive and negative electrical charge, an individual quark can have one of three charges labeled red, green, or blue. There are eight gluons that carry carry different combinations of these color charges.

QCD then describes the interactions of quarks and gluons in the $SU(3) \times SU(2) \times U(1)$ gauge group. The gluons mediate the color force and can interact with themselves. There are six quarks called flavors, three with electrical charge 2/3 and three with electrical charge $-1/3$. The lightest two, the up and down, make up all of the visible matter in the universe (protons and neutrons). They also make up the most common hadron produced in heavy ion collisions, the pion. The remaining quarks in order of mass are the strange, charm, bottom, and top.

Quarks combine to form hadrons, which are the particles that we ultimately detect. Individual quarks carry both a color and electrical charge. Unlike the electrical charge, the total color charge of a hadron must always add to a neutral (colorless) state. This

corresponds to the confinement condition that prevents experimental observation of a free quark.

Hadrons come in two categories, baryons, containing three quarks, and mesons, containing two quarks. A proton is and example of a baryon since two up quarks and a down quark combine to describe its quantum numbers ($p = uud$). Similarly, a pion is made of combinations of an up with antidown ($\pi^+ = u\bar{d}$), down with antiup ($\pi^- = d\bar{u}$), or $\pi^0 = (u\bar{u} + d\bar{d})/\sqrt{2}$. In addition to the valence quarks that describe the quantum numbers of the hadron, there is a "sea" of quarks and gluons that contribute to the total distribution of the hadron. The primary goal of deep inelastic scattering experiments is to map out this distribution.

The confinement condition is central to the motivation for studying relativistic heavy ion collisions. The goal is to create an environment where the temperature and energy density is high enough that quarks and gluons do not "identify" with any particular hadron and the color charge is globally rather than locally neutral. This is perhaps the only situation where one can observe "free" quarks and gluons.

## 2.2 Relativistic Heavy Ion Collisions

In many ways collisions of relativistic nuclei at RHIC are analogous to the Big Bang. Each "Little Bang" collision is a space-time event with a sudden deposition of high energy density into the vacuum. What starts as quantum fluctuations ends as causally disconnected hadronic matter.

The stages of a heavy ion collision are illustrated in Fig.2.3. In the center of mass frame, nuclei first appear as highly Lorentz contracted pancakes due to their relativistic speeds. At the moment of the collision, the dense, contracted nuclei pass through each other in a sort amount of time. Due to large numbers of inelastic interactions, a large amount of energy is deposited in the vacuum at the collision center. Reminiscent of the inflationary period of the early universe, the nuclei continue on, driving

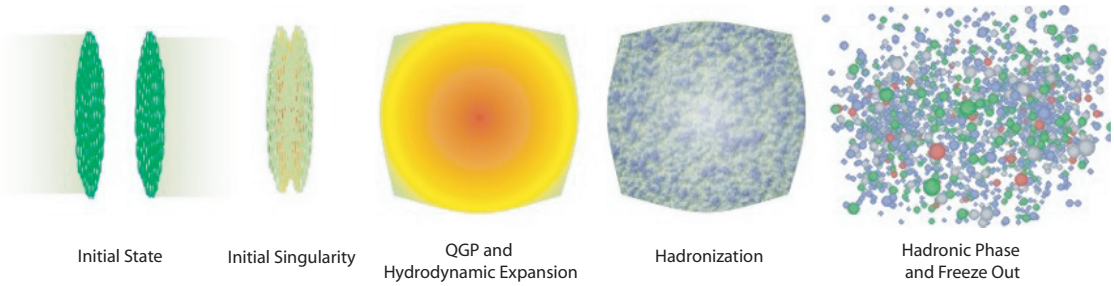


Figure 2.3: A schematic picture of the matter produced in heavy ion collisions. Image from S. Bass

a rapid longitudinal expansion of any produced medium [81]. This medium consists of quarks and gluons that are thought to transition into a thermalized quark-gluon plasma (QGP), as evidenced by the apparent ideal hydrodynamical expansion of the system. As the system expands the temperature drops and quarks and gluons must experience another transition into colorless hadronic states. Finally, rescatterings of hadrons cease and all hadrons "freeze out", meaning their momentum will remain unchanged thereafter.

The initial singularity dictates much about the following evolution of the system. A traditional geometrical (Glauber) approach is sufficient to explain many phenomenon observed in nuclear collisions. The Glauber approach quantifies how head on or central nuclear collisions are in terms of number of interactions of individual nucleons. For example, at a given impact parameter $b$ ($b = 0$ being the most central or directly head on), one can calculate, using probability theory, the number of nucleons that participate in at least one inelastic collision, $N_{part}$, and the number of binary nucleon-nucleon collisions, $N_{coll}$ (See Appendix B for a more detailed description). One can make assumptions about particle production and fluctuations of initial parton densities based on these quantities. For example, the soft (thermally produced) part of measured spectrum of hadrons seems to scale with $N_{part}$, while interactions following from perturbative QCD seem to scale with $N_{coll}$. This Eikonal

model is significantly different in principle from that of the Color Glass Condensate [19, 16], see Sec.4.5. The Color Glass Condensate approach is described in Ch.4. It relies on the gluon saturation picture, and distinguishes between perturbative and non-perturbative processes with a momentum transfer scale $Q_s$. Both approaches lack the ability to provide a quantitative description of the QGP.

The primary concern of experiments at RHIC is the search for the quark gluon plasma. At very high temperatures the coupling of the strong force should become small, and quarks and gluons should become "free" inside the dense medium. If this is the case, there should be an increase in the number of degrees of freedom corresponding to those of quarks and gluons rather than hadrons. An ideal gas of hadrons would have the three translational degrees of freedom, but this number should largely increase because the availability in QGP for changes of color and quark flavor. Each gluon would have two helicities and eight colors and each quark has three colors, two spins, and a quark-antiquark pair. So, the number of degrees of freedom in a QGP would be $2 \times 8 + 3 \times 2 \times 2 \times N_F = 52$ if the number of contributing quark flavors is $N_F = 3$. Lattice QCD calculations do see a rapid increase in the number of degrees of freedom around a critical temperature $T_c \approx 170MeV$, see for example Refs.[82, 83, 84]. RHIC temperatures at the formation stage of the QGP reach $2T_c$, so the relevant degrees of freedom should be those of quarks and gluons.

$J/\psi$ suppression is one proposed signature of the existence of QGP [85]. It relies on the prevention of the formation of $c\bar{c}$ pairs through a Debye screening of color charge. Another signature is the observed enhancement in strange hadrons over those seen in the same number ($N_{coll}$) of p+p collisions [86]. The ability of ideal hydrodynamics to explain the the transverse expansion of the system also lends its self to the argument for the existence of QGP, see Sec.2.3 for more information. For more details about other possible signature of QGP see [87, 88].

It seems that there is no first order but rather a smooth phase transition from

the QGP phase to the hadronic phase. The hadronization process itself is also not completely understood. Hadronization occurs when the system expands such that the density of partons is not large enough to maintain a global colorless state. Quarks and gluons combine to form hadrons which freeze out when the mean free path between hadrons is larger than that of the system.

## 2.3 Elliptic Flow

Along with jet quenching, the hydrodynamical behavior of the system created in heavy ion collisions has been one the most striking results from RHIC. Ideal hydrodynamics does an excellent job of describing the flow of hadrons at $p_t$ less than 2 GeV. In particular, the observation of anisotropic flow is unique to heavy ion collisions and is a useful tool for relating the geometry of the collisions to the pressure gradients of the matter produced at the earliest times of the collisions [89]. For this reason, flow provides a background for correlation measurements, and fluctuations in flow measurements could probe fluctuations in the initial conditions.

The azimuthal shape of final state particle distributions is seen to change from central to peripheral collisions [9, 30, 31, 32]. A Fourier analysis of the distribution provides a mathematical description with quantities (the Fourier coefficients) that have physical meaning [89]:

$$\frac{1}{N}\frac{dN}{d\phi} = 1 + 2v_1\cos(\phi - \Psi_{RP}) + 2v_2\cos[2(\phi - \Psi_{RP})] + \cdots \tag{2.1}$$

with

$$v_n = \langle\cos[n(\phi - \Psi_{RP})]\rangle. \tag{2.2}$$

$\Psi_{RP}$ defines the angle that the event reaction plane makes with the detector, and the Fourier coefficients, $v_1$ and $v_2$ relate to the shape of the distribution corresponding to "directed flow" and "elliptic flow" respectively. These shapes are illustrated in

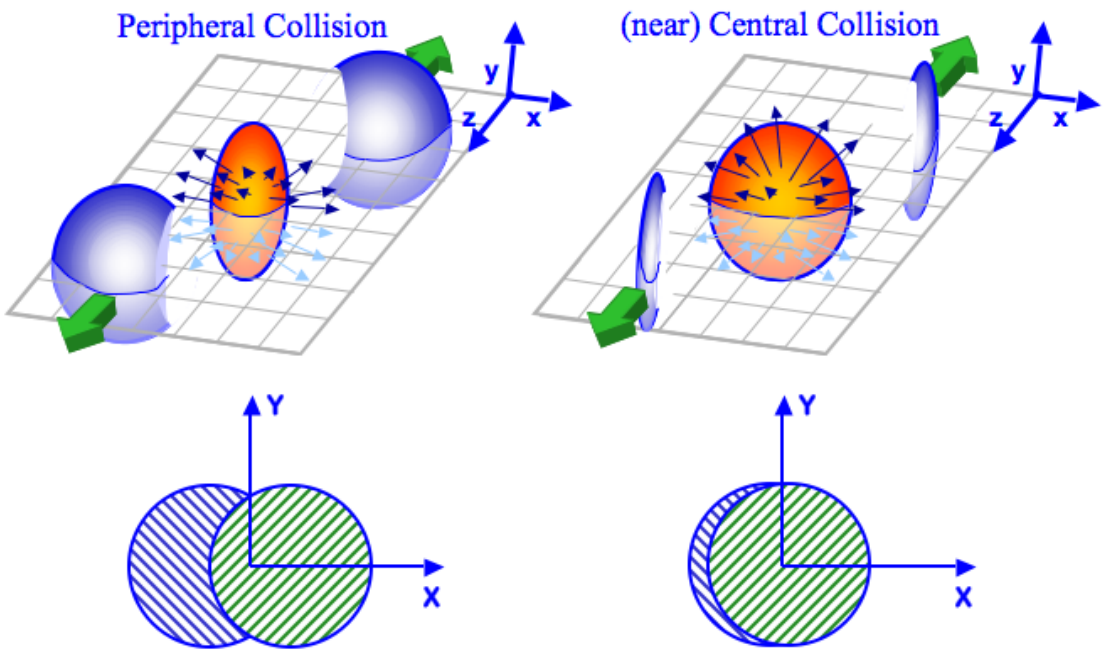


Figure 2.4: A diagram of (left) an off-center collision producing anisotropic flow, and (right) a central collision with small elliptic flow and large directed flow. The x-z plane defines the event reaction plane. Image created by Masashi Kaneta.

Fig.2.4. If a collision is peripheral, as in the left side of Fig.2.4, then for the collision of identical symmetric nuclei, the density of the overlap region is larger in the x-direction than the y direction. The x-direction and the z-direction (beam direction) define the reaction plane. The anisotropy in density of the overlap area leads to pressure gradients in the collision volume; there is a larger push in the x-direction than the y-direction. At RHIC, this corresponds to 30% more particles in the direction of the reaction plan than out of plane, and a large $v_2$ value. The right side of Fig.2.4, corresponds to a central collision, where the resulting volume density is nearly spherically symmetric. In this case, the transverse push is similar in all directions, minimizing $v_2$, but corresponding to a larger $v_1$.

The elliptic flow parameter, $v_2$, changes as a function of centrality as well as the $p_t$ of measured particles. Ideal hydrodynamics does an excellent job of describing $v_2$ for $p_t < 2\ GeV$ [90, 91]. Fig. 2.5 illustrates this point with a compilation of STAR and

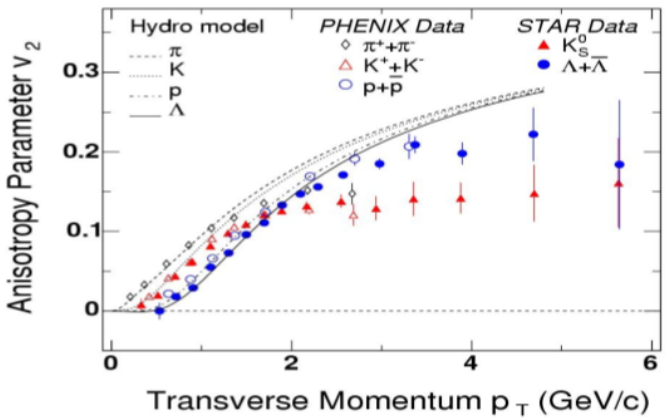


Figure 2.5: Elliptic flow ($v_2$) plotted as a function of transverse momentum $p_t$ for identified hadrons. Compilation of STAR and PHENIX data with hydrodynamic predictions as presented in [6]

PHENIX data and theoretical predictions [6]. Past this point, ideal hydro predicts further increase, but the data flattens. The flatness in the data could correspond to the suppression of high $p_t$ particles in nuclear collisions. Fast partons are slowed to smaller $p_t$ as they traverse the medium, decreasing the number of fast hadrons in the final state, and increasing the number of slower ones. Alternatively, viscous corrections to hydrodynamics could have the same effects [90, 91, 92, 93, 94, 95, 96]. Thermal partons that have the greatest push from the pressure gradients would have a larger $p_t$ , but viscosity essentially forces the faster partons to drag the slower ones along, slowing them down.

It is no coincidence, however, that the region of best comparison corresponds with the soft part of the spectrum. The soft or thermal particles are those thought to be born of the QGP, where above 2 GeV, pQCD effects start to become important. The so-called constituent scaling is further evidence for this argument. As seen in Fig. 2.6, the $v_2$ of both baryons and mesons follows the same trend when the total $v_2$ per quark is plotted vs. the transverse kinetic energy per quark. In other words, the total $v_2$ of each baryon is divided by three (the number of valence quarks) and the $v_2$ for each meson is divided by two. The same is done for the transverse kinetic

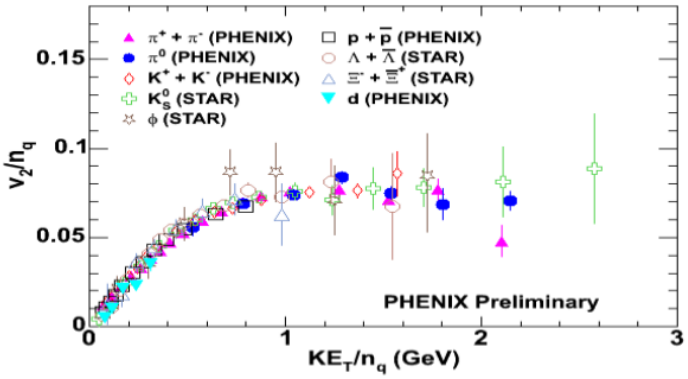


Figure 2.6: The elliptic flow parameter plotted as $v_2/quark$ against the transverse energy/quark [6].

energy of each baryon or meson. The fact that all light hadrons have the same $v_2$ per quark at any given $k_t$ indicates that the same transverse energy is given to each individual quark before hadronization. This fits the flowing QGP picture, but does not eliminate the possibility that the hadronic phase just has a very large viscosity which could quickly normalize the momenta of slower hadrons.

The shape of $v_2$ has an impact on correlation measurements. Since there are more particles pushed in the direction of the reaction plane, and those particles receive a bigger push, one would find more pairs of particles at small angular separations, where $\phi = \phi_1 - \phi_2$ is the relative azimuthal angle between the particle pair. Pairs with relative angles $\phi \sim 90°$ are comparatively suppressed. At $\phi \sim 180°$ one expects a similar number of pairs with this angular separation to those at small $\phi$. The correlation background then has the shape

$$C(\phi) = b_0(1 + 2\langle v_2^{trig} v_2^{asoc} \rangle \cos(2\phi)) \tag{2.3}$$

where $v_2^{trig}$ and $v_2^{asoc}$ are the Fourier coefficients corresponding to angular distributions of particles in a trigger $p_t$ range and that of particles in an associated $p_t$ range [97]. The coefficient $b_0$ is set by the Zero Yield at Minimum (ZYAM) method for triggered ridge measurements [2, 3, 5, 4, 48, 49, 50], and left as a free parameter in

soft ridge fits to data [1, 26, 51]. Since $v_2$ is sensitive to fluctuations in initial conditions, and CGC initial conditions predict larger eccentricities in initial elliptic density distributions (and therefore larger $v_2$), there could be a model dependent effect in the shape of the ridge. The ridge is a correlation structure that remains after known sources of correlations are subtracted; the azimuthal width of the ridge depends on the magnitude of the $v_2$ subtraction. However, this is only a problem in the hard ridge measurement since the contribution from $v_2$ in the soft ridge measurement is fit rather than subtracted.

## 2.4 Jets

During hadronic collisions, partons can scatter with very large momentum transfers. In this case, colored partons move off with large transverse momenta. Such events are well described by perturbative QCD since for high energy interactions the strong coupling is small. The high $p_t$ partons quickly radiate gluons which split into multiple quarks which all form hadrons to conserve quantum numbers, momentum, and a colorless state. This process is called jet fragmentation. Because of the large energy and $p_t$ , the fragments from a jet are focused into a narrow cone opening in the direction of the original leading particle. Unlike collective phenomenon like flow and $v_2$, jets are also seen (and more well defined) in p+p collisions. Fig. 2.7 shows a schematic diagram of a hard scattering of two quarks in a p+p collision forming back to back jets. In principle, two quarks could scatter elastically into jets, or annihilate on impact and form gluon jets. One parton gains large transverse momentum and fragments. A momentum conserving away side jet is found 180° away in the transverse plane.

In heavy ion collisions, the situation is somewhat different. If the jets are formed in the center of the collision volume, they have to traverse the medium before they escape. Experiments at RHIC have measured unexpectedly low multiplicities of high

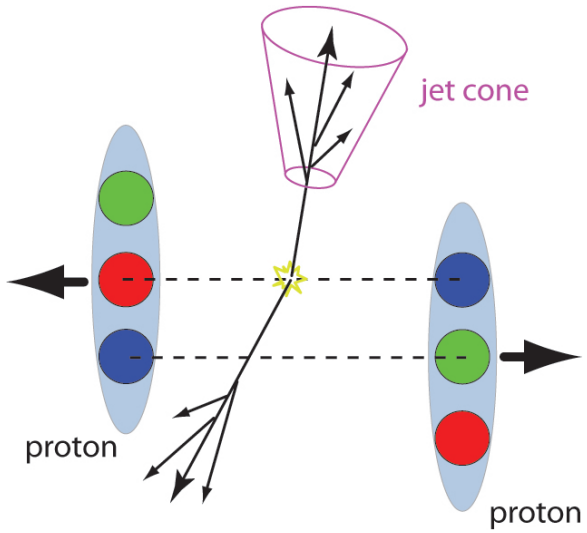


Figure 2.7: Hard scattering of two quarks in a p+p collision, and back to back high $p_t$ jets result.

$p_t$ hadrons. This is constant with the saturation picture described in Sec.4.1, and the discovery of jet quenching.

Jet quenching is the attenuation of the fast colored object as it passes through the dense strongly interacting partonic medium. Thus, the probability that a jet escapes the medium is proportional to the length of its path through the medium, and observed jets are biased toward the surface. Evidence of this is shown in Fig.2.8 [7].

Jets are found by identifying a fast hadron, called the trigger and associated hadrons within a selected $p_t$ threshold. Measurement of the associates' azimuthal angle relative to the jet indicates a strong correlation with the leading particle. This is seen in Fig.2.8, where a narrow peak, that represents the jet cone, is found centered about small relative angles. Momentum conservation would suggest a peak centered $\Delta\phi = 180°$. Indeed, in p+p and d+Au collisions this peak is present, but absent in Au+Au collisions.

The absence of a di-jet in heavy ion collisions suggests that the away side jet is attenuated or absorbed by the medium. If the triggered jet is near the surface

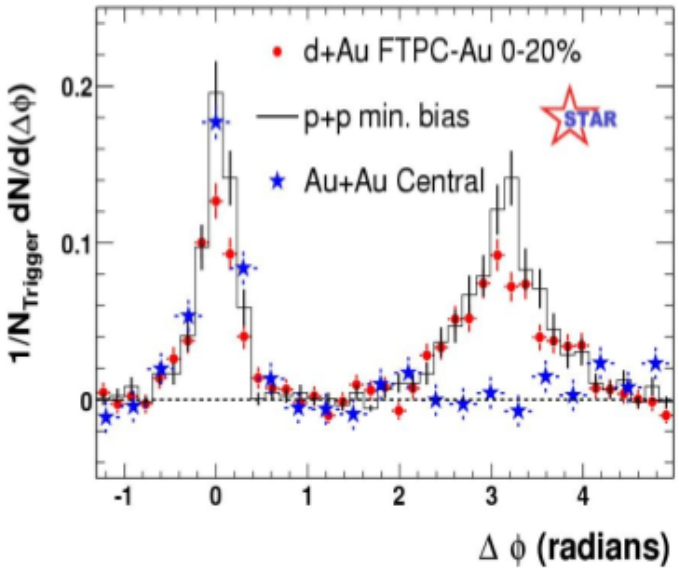


Figure 2.8: Correlations in azimuthal angle between high momentum hadrons showing evidence of suppression of back-to-back jets in central Au+Au relative to p+p and d+Au collisions as seen by the STAR collaboration [7].

of the collision area, then the away side jet must pass through the dense medium. Quenching of the away jet would support a strongly coupled QGP. Following this reasoning, the medium could completely quench di-jets produced close to the collision center, biasing observed jets to the surface. In fact, the identification of jets in central Au+Au collisions is suppressed by a factor of 4-5 relative to the number found in p+p or d+Au collisions [43, 98]. In contrast, the number of direct photons which escape the medium without modification, agrees nicely with the appropriately scaled amount found in p+p [98].

The response of the medium to the passage of a jet has become an important topic, and in some sense spurred the work presented in this dissertation. The energy lost by the jet must equal an energy gain by the medium. Correlation measurements could observe these changes. The jet quenching measurement is itself a correlation measurement since it compares the azimuthal angle of hadrons relative to the jet trigger. The hard ridge measurement is an extension of this, comparing both relative azimuthal and rapidity coordinates.

The nature of fragmentation into a narrow cone is responsible for the jet peak. Fragments splinter off the fast parton, co-moving in the same transverse direction at about the same rapidity. Therefore, as seen in jet quenching and hard ridge measurements, there is an abundance of correlated associates at small angles away from the jet axis, and few at large angles.

Many have suggested that the formation of the near side ridge is a result of the jet passage through the medium [67, 68, 69, 70, 71, 72, 73, 74, 75]. Ref. [79] suggests that the jet has coincidental correlations with bulk matter based on the position of production and transverse bulk flow and jet quenching collaboratively direct particles to common emission angles. Our work [37], presented here, adopts this prescription, as described in Ch.6.

# Chapter 3

## The Blast Wave Model

Rapid transverse expansion is one of the predominant features of relativistic heavy ion collisions. The transverse momentum spectrum from RHIC indicates that the hadronic average final state transverse velocity is larger than that of a freely expanding thermal source. The conditions at RHIC can be described with a blast wave scenario.

The blast wave model is useful since it describes a significant feature of heavy ion collisions while incorporating only a small fraction of the physical processes involved in heavy ion collisions. Given a temperature, it provides a reasonable description of how a medium of particles gains a collective transverse flow. Among other things, it does not incorporate the underlying particle production mechanism, perturbative QCD processes, or the hadronization process. Furthermore, a full hydrodynamical description would be more useful for characterizing the system, since it would have information on the equation of state as well as the sheer and bulk viscosity. The blast wave model is useful, though, because of its simplicity; it characterizes the transverse expansion of the system with only two parameters, $\beta$ (also called $v_{surface}$), the transverse velocity, and $T$, the temperature. Since the collective behavior of soft particles influences almost all observables, it is convenient to have a model for specifically that phenomenon.

In this chapter, we review the features of the blast wave model following primarily Refs. [99, 100, 101]. In Secs. 3.2 and 3.3, we extend this treatment with the intent on

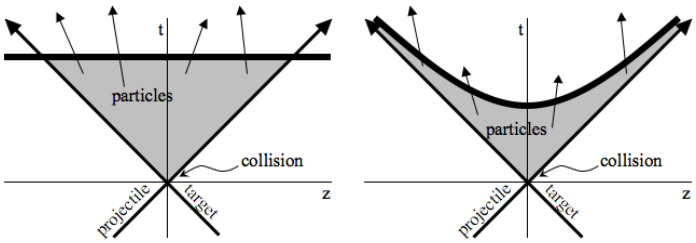


Figure 3.1: Light cone diagrams indicating different freeze out scenarios. (Left) Constant time freeze out. (Right) Constant proper time freeze out. Higher rapidity particles freeze out later and the freeze out surface conforms to the beam axes which move at nearly the speed of light.

its application to our correlation studies.

## 3.1 Features of the Blast Wave Model

In relativistic ion collisions, the sudden localized deposition of energy produces an initially hot and dense medium of particles with random transverse motion. Particles on the surface moving outward from the center of the medium could do so freely, but surface particles with an inward velocity would scatter from particles in the dense core. As a result, surface particles will expand outward with an average velocity in the radial direction. The next innermost layer of particles would scatter from both the more dense core as well as the outer surface particles. However, as the surface particles deflected outward, filling more space and becoming more diffuse, the next layer can also expand outward. The expansion of the entire system follows in this manner. This anisotropy in density gives rise to pressure gradients that do work to expand the system. These are the characteristics of a shock or blast wave [99].

The major aspects of the blast wave model are as follows:

- *Transverse flow:* The outermost layer of particles in the system acquires a radial velocity because collisions with the next innermost layer continue until the outer particles have an outward trajectory. Just inside the outer layer, the pressure gradient is largest, providing the largest push outward. Successive layers will

receive less of a push as the system expands and the pressure gradient decreases. The final velocity of each layer of particles then depends on its initial radial position; the particles starting at a larger radius get a larger transverse boost. Following this idea, the following calculations utilize a Hubble-like expansion velocity,

$$\gamma_t \mathbf{v}_t = \lambda \mathbf{r}. \tag{3.1}$$

- *Freeze out:* The picture drawn in this chapter, where outer layers of particles expand out while inner layers continue to interact, changing the surface of the volume in space-time, assumes a constant proper time freeze out scenario. Rather than assuming all particles freeze out at the same time, the constant proper time requires that all particles freeze out at the same proper time, $\tau_F = constant = \sqrt{t^2 - \mathbf{x}^2}$, or in the Bjorken approximation, $\tau_F = constant = \sqrt{t^2 - z^2}$ . In this case, faster or higher rapidity particles freeze out later than slower ones. This is illustrated in the right diagram in Fig. 3.1. The space-time hypersurface $\sigma$ defines a borderline between flowing behavior and free streaming [100]. The element $d\sigma_\mu$, moving with momentum $p^\mu$ is defined as

$$d\sigma_\mu = (d^3x, 0, 0, dtdxdy) \tag{3.2}$$

for constant proper time, and

$$d\sigma_\mu = (d^3x, 0, 0, 0) \tag{3.3}$$

for constant time freeze out.

Since the goal of the blast wave model is to determine the distribution of particles freezing out on $\sigma$ with velocity $\beta$, the differential element of interest is then $p^\mu d\sigma_\mu$, where $p^\mu = (E, \mathbf{p})$ is the 4-momentum. Cooper and Frye show that this

differential is also required for energy conservation [101].

- *Energy conservation:* The reduction of random or thermal kinetic energy (cooling) is precisely the energy associated with the average radial velocity $\langle\beta\rangle$ providing outward or "directed" flow. A purely thermal source would have a distribution function $\propto exp[-\gamma E/T]$, but in the blast wave picture, energy for transverse flow is taken from the thermal energy such that the distribution is $\propto exp[-\gamma(E - \mathbf{v}\cdot\mathbf{p})/T]$. As a result, the particle distribution peaks about a mean radial velocity, where a thermal source would have a peak at a lower velocity where the multiplicity is higher [99].

- *Entropy conservation:* The entropy reduction due to the more orderly, collective motion is equal to the entropy gain from spatial expansion. In other words, the entropy gain due to expansion of position space is compensated by the entropy loss from the narrowing of momentum space, implying that the expansion force is reversable. Gains in entropy, not built into the blast wave model, come from fluctuations in the medium. If there are only cells of local thermal equilibrium, processes such as conduction between the cells (thermal fluctuations) and diffusion (momentum fluctuations) would increase the entropy. These contributions should be small if the system is in a globally thermalized QGP phase.

- *Particle Number:* Since the blast wave model contains no information about the initial production mechanism of partons, it cannot predict the absolute number of particles. Generally the magnitude of blast wave particle distributions are normalized to data.

- *Boost invariance:* The transverse boost given to a particle depends only on its radial position. This implies two things: 1) that longitudinal expansion is significantly more rapid than transverse expansion, and 2) that the system initially resembles a long cylinder with the same azimuthal distribution at any longitu-

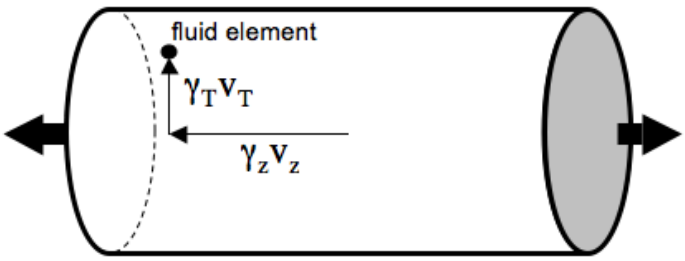


Figure 3.2: A schematic diagram representing the velocity of a fluid element as two successive boosts in a uniform cylindrical system. The scenario depicted here infers that the transverse velocity depends only on the transverse boost and is independent of the boost to the longitudinal position.

dinal position. The velocity at any position, then consists of a longitudinal and transverse boost as illustrated in Fig. 3.2. Consequentially, the gamma factor is then approximated as a factorization of the two boosts, such that $\gamma \approx \gamma_z \gamma_t$.

- *Boltzmann Distribution:* For mathematical simplicity, a Boltzmann distribution (with transverse boost) has been taken in replacement of Fermi or Bose distributions.

Cooper and Frye show in Ref. [101] that the distribution of particles with momentum $p^\mu$ within a surface element $d\sigma_\mu$ in the neighborhood of space-time point $x^\mu$ is

$$E\frac{dN}{d^3p} = \int_\sigma f(\mathbf{x}, \mathbf{p}) p^\mu d\sigma_\mu. \tag{3.4}$$

We can then calculate important quantities including $N$, $dN/dy$, $\langle p_t \rangle$, and $v_2$, from

(3.4) as follows:

$$N = \int E \frac{dN}{d^3p} d^3p \tag{3.5}$$

$$\frac{dN}{dy} = \int E \frac{dN}{d^3p} p_t d_t d\phi \tag{3.6}$$

$$\langle p_t \rangle = \frac{1}{N} \int p_t \; E \frac{dN}{d^3p} d^3p \tag{3.7}$$

$$v_2 = \frac{1}{N} \int \cos 2\phi \; E \frac{dN}{d^3p} d^3p \tag{3.8}$$

Following closely to [100], we choose a Boltzmann phase-space distribution

$$f(\mathbf{x}, \mathbf{p}) = a e^{-(u^\mu p_\mu)/T} \tag{3.9}$$

which is boosted by the local fluid velocity $u^\mu(\mathbf{x})$ and $a$ is a normalization constant. Following the boost invariance approximation, $u^\mu(\mathbf{x})$ represents successive longitudinal and transverse boosts,

$$u^\mu(\mathbf{x}) = (\gamma, \gamma \mathbf{v}) = (\gamma_z \gamma_t, \gamma_t \mathbf{v}_t(\mathbf{r}), \gamma_t \gamma_z v_z) \,. \tag{3.10}$$

We define a "spatial" rapidity, $\eta$ representing the longitudinal boost

$$\frac{z}{t} = \tanh \eta \tag{3.11}$$

$$z = \tau \sinh \eta \tag{3.12}$$

$$t = \tau \cosh \eta \tag{3.13}$$

$$\tau = \sqrt{t^2 - z^2}. \tag{3.14}$$

Furthermore (3.12) can be rewritten

$$\frac{\gamma_z v_z}{\gamma_z} = \tanh\eta \tag{3.15}$$

$$\gamma_z v_z = \sinh\eta \tag{3.16}$$

$$\gamma_z = \cosh\eta \tag{3.17}$$

such that (3.10) can take the form

$$u^\mu(\mathbf{x}) = (\gamma_t \cosh\eta, \gamma_t \mathbf{v}_t(\mathbf{r}), \sinh\eta)\,. \tag{3.18}$$

Making use of (3.13) and (3.14), the surface element (3.2), in cylindrical coordinates, becomes

$$d\sigma_\mu = (\cosh\eta, 0, 0, \sinh\eta)\ \tau r dr d\theta d\eta. \tag{3.19}$$

Similarly, we write the 4-momentum in terms of the rapidity variable

$$p^\mu = (E, \mathbf{p}_t, p_z) = (m_t \cosh y, p_t, m_t \sinh y)\,. \tag{3.20}$$

To obtain the differential in (3.4), we combine (3.20) with (3.2) and relate $dt$ with (3.14) to obtain

$$\begin{aligned} p^\mu d\sigma_\mu = (E d^3x - p_z dt d^2r) &= (m_t \cosh y\ r dr d\theta dz - m_t \sinh y\ r dr d\theta dt) \\ &= [(m_t \cosh y)(\tau \cosh\eta\ d\eta) - (m_t \sinh y)(\tau \sinh\eta\ d\eta)]\ r dr d\theta \\ &= \tau m_t \cosh(y-\eta)\ r dr d\theta d\eta. \end{aligned} \tag{3.21}$$

The argument of the exponential in (3.9) makes use of (3.18) and (3.20) and gives

$$\begin{aligned} u^\mu p_\mu &= \gamma_t m_t \cosh y \cosh\eta - \gamma_t \mathbf{v}_t \cdot \mathbf{p}_t - \gamma_t m_t \sinh y \sinh\eta \\ &= \gamma_t m_t (\cosh y \cosh\eta - \sinh y \sinh\eta) - \gamma_t \mathbf{v}_t \cdot \mathbf{p}_t \\ &= \gamma_t m_t \cosh(y-\eta) - \gamma_t \mathbf{v}_t \cdot \mathbf{p}_t. \end{aligned} \tag{3.22}$$

Substituting (3.22) in (3.9) we obtain

$$f(\mathbf{x},\mathbf{p}) = a e^{-\frac{\gamma_t m_t}{T}\cosh(y-\eta)} e^{\frac{\gamma_t \mathbf{v}_t \cdot \mathbf{p}_t \cdot}{T}}, \tag{3.23}$$

and using (3.21) we rewrite (3.4) to take the form

$$E\frac{dN}{d^3p} = a \int e^{-\frac{\gamma_t m_t}{T}\cosh(y-\eta)} e^{\frac{\gamma_t \mathbf{v}_t \cdot \mathbf{p}_t \cdot}{T}} \tau m_t \cosh(y-\eta)\; r dr d\theta d\eta. \tag{3.24}$$

To introduce the Hubble-like expansion term we substitute (3.1) into (3.24), noticing the expansion velocity only appears in one term. The usefulness of the boost invariance approximation becomes apparent here, since (3.24) factorizes if the temperature and transverse flow are independent of longitudinal position, and $\gamma_t \approx$ constant. In this work, we study the blast wave model for both the "real" and "constant" $\gamma_t$ cases. The quotations suggest that one should not take the words literally. The "real" gamma case is useful for chapter 7, where the "constant" gamma case is useful for chapters 5 and 6.

## 3.2 "Real" $\gamma_t$

Since the transverse velocity depends on position through (3.1), the gamma factor related to the *transverse* boost should also depend on position. The *longitudinal* boost to a transverse plane does not remove this dependency. To determine $\gamma_t(\mathbf{r})$, we take

the radial position vector to be

$$\mathbf{r} = \epsilon_x x\hat{x} + \epsilon_y y\hat{y} \tag{3.25}$$

where the eccentricities are defined as

$$\epsilon_x = \sqrt{\frac{1+\epsilon}{2}} \tag{3.26}$$

$$\epsilon_y = \sqrt{\frac{1-\epsilon}{2}}. \tag{3.27}$$

We parameterize the eccentricity $\epsilon$ with centrality using

$$\epsilon = a + d\left(\frac{b^2}{b^2 + 2\chi^2}\right) \tag{3.28}$$

where $b$ is the impact parameter and the others are free parameters with values $a = 0.07$, $\chi = 3.0$, and $d = 0.43$ . We can then write

$$\begin{aligned} \gamma_t^2 v_t^2 = \frac{v_t^2}{1 - v_t^2} \Rightarrow \gamma_t^2 v_t^2 = \gamma_t^2 - 1 \\ \gamma_t = \sqrt{1 + \lambda^2(\epsilon_x^2 x^2 + \epsilon_y^2 y^2)}. \end{aligned} \tag{3.29}$$

In the transverse plane of a radially boosted cell, (3.29) implies no further approximations, and (3.24) does not factorize. Conversely, Sec. 3.3 chooses an approximation for $\gamma_t$ that allows (3.24) to factorize. Furthermore, for reasons explained in chapter 7, we add the term $\mathcal{M}(x, y, \eta)$ to modify the spatial distribution of (3.9), to have a gaussian rather than isotropic distribution, where

$$\mathcal{M}(x, y, \eta) = e^{\frac{-x^2}{2\sigma_w^2}} e^{\frac{-y^2}{2\sigma_w^2}} e^{\frac{-\eta^2}{2\sigma_\eta^2}}. \tag{3.30}$$

Here, $\sigma_w$ and $\sigma_\eta$ represents the widths of the gaussian spatial densities. For central collisions, $\sigma_w$ is proportional to the nuclear radius, and reduces like a power law with $N_{part}$, and $\sigma_\eta$ is constant with centrality. Using (3.1), and $\mathbf{p}_t = p_t(\cos\phi\hat{x} + \sin\phi\hat{y})$ so that $\gamma_t \mathbf{v}_t \cdot \mathbf{p}_t = \lambda p_t(\epsilon_x x\cos\phi + \epsilon_y y \sin\phi)$, we rewrite (3.24) substituting (3.1), (3.25), (3.29), and (3.30) and

$$E\frac{dN}{d^3p} = a\int e^{-\sqrt{1+\lambda^2(\epsilon_x^2x^2+\epsilon_y^2y^2)}\frac{m_t}{T}\cosh(y-\eta)}$$

$$\times e^{\lambda p_t(\epsilon_x x\cos\phi+\epsilon_y y\sin\phi)/T}$$

$$\times e^{\frac{-x^2}{2\sigma_w^2}} e^{\frac{-y^2}{2\sigma_w^2}} e^{\frac{-\eta^2}{2\sigma_\eta^2}} \tau m_t \cosh(y-\eta)\; rdrd\theta d\eta, \tag{3.31}$$

which we integrate using the Monte Carlo: Vegas integration routine. With this code, we calculate $dN/dy$, $\langle p_t\rangle$, and $v_2$ to check the validity of the model. Figures 3.3 and 3.4 show the $\langle p_t\rangle$, and $v_2$ comparisons to data respectively. In Fig. 3.3, the solid lines represent the $\langle p_t\rangle$ for pions, kaons, and protons with a constant temperature of $T = 120MeV$. The pions fit well, however the kaons and protons do not show good agreement. It is possible that including resonances will improve the kaon and proton curves, but that is not covered here. Moreover, all of the work presented here accounts for only pions so, for now, it is only critical that the pion $\langle p_t\rangle$ is correct. Additionally, we simultaneously calculate the pion $v_2$ . This also fits well, but depends on the eccentricity parameterization (3.28) and spatial widths $\sigma_w$ and $\sigma_\eta$.

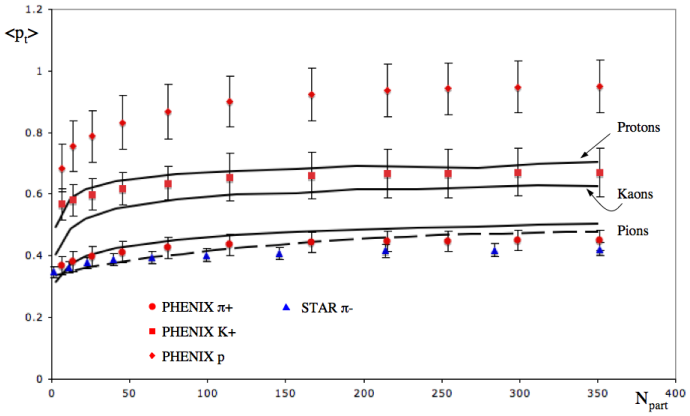


Figure 3.3: $\langle p_t \rangle$ fits to experimental data with a temperature at 120 MeV, constant with centrality. The solid lines are the "real" gamma calculations, and the dashed line is the "constant" gamma calculation with constant temperature. The circles, squares, and diamonds represent PHENIX data for pions, kaons and protons respectively [8]. The triangles represent STAR pion data [9].

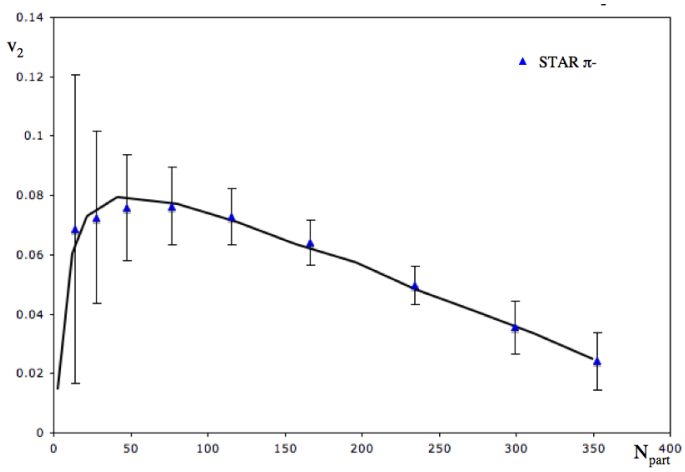


Figure 3.4: Blast wave calculation of pion $v_2$ with temperature is constant with centrality at 120 MeV. The solid line is the "real" gamma calculation fit to a STAR measurement [9]. The "constant" gamma calculation does not include eccentricities and would appear flat in this figure.

## 3.3 "Constant" $\gamma_t$

In order for (3.24) to factorize, $\gamma_t$ must be independent or constant with radial position. For mathematical convenience we use the approximation

$$\gamma_t = (1 - v_t^2)^{-1/2} \approx (1 - v_s^2)^{-1/2} \tag{3.32}$$

where $v_s$ is the surface velocity measured by experiment [27].

Making use of the modified Bessel function $K_\nu(z) = \int_0^\pi e^{z\cosh\theta}\cosh(\nu\theta)d\theta$, using $\nu = 1$, we integrate the first exponential in (3.24) over$d\eta$ and find

$$\int_{-\infty}^{\infty} e^{-\gamma_t m_t \cosh(y-\eta)/T}\cosh(y-\eta)d\eta = 2K_1\left(\frac{\gamma_t m_t}{T}\right). \tag{3.33}$$

Notice that the $y$ is a constant of integration and the resulting function is independent of rapidity. This is the mathematical consequence of the boost invariance approximation. Taking our attention now to the second term in (3.24), after substitution of (3.1), the argument of the exponential is now $\lambda r p_t \cos\varphi/T$, and angle between the radial vector and the momentum vector is equivalent to $\varphi = 180° - \phi + \theta$ where $\phi$ and $\theta$ are the momentum and spatial angles respectively. Again making use of another modified Bessel funtion

$$I_\nu(z) = \frac{1}{\pi}\int_0^\pi e^{z\cos\theta}\cos(\nu\theta)d\theta, \tag{3.34}$$

using $\nu = 0$, the second exponential in (3.24) can we integrate $d\theta$ such that

$$\int_0^{2\pi} e^{\lambda r p_t \cos(\phi-\theta)/T}d\theta = 2\pi I_0\left(\frac{\lambda r p_t}{T}\right). \tag{3.35}$$

Notice again, that the angle $\phi$ is a constant of integration and is absent in the re-

sulting Bessel function. This is an indication that the final state emission of particles is isotropic, or as some might say, "flat" in the azimuthal plane, meaning there is no anisotropic flow. Since (3.35) is the only term that has a radial dependence, we can be perform the final spatial integration using the Bessel function relation $\int_0^1 z^{\nu+1} I_\nu(\alpha z) dz = \frac{1}{\alpha} I_{\nu+1}(\alpha)$, and the substitution $r = Rz$, so that

$$\int_0^R 2\pi I_0\left(\frac{\lambda r p_t}{T}\right) r dr = \int_0^1 2\pi I_0\left(\frac{\lambda p_t}{T} Rz\right) R^2 z dz = 2\pi \frac{R^2 T}{\lambda R p_t} I_1\left(\frac{\lambda R p_t}{T}\right). \tag{3.36}$$

Introducing the notation where $\rho_1$ represents the single particle distribution such that $\rho_1(\mathbf{p}) = E dN/d^3p$, eq.(3.24) is now

$$\rho_1(\mathbf{p}) = a' \frac{4\pi R^2 T}{\lambda R} \frac{m_t}{p_t} K_1\left(\frac{\gamma_t m_t}{T}\right) I_1\left(\frac{\lambda R p_t}{T}\right). \tag{3.37}$$

The normalization constant, $a'$, ensures that $\int f(\mathbf{x}, \mathbf{p}) d^3p = n(\mathbf{x})$ and has the form $a' = a(dN/dy|_{y=0})/(\pi R^2)$. This is a consequence of the fact that the blast wave model cannot calculate the correct particle number and we require that this factor cancels in later calculations.

Following from (3.1), which relates the flow velocity to the radial position, if the position is $R$, then $\lambda R = \gamma_t v_s$, where $v_s$ is the surface velocity and is a measure of the average flow velocity. We fix these parameters with measurements from experiment [27].

Finally for mathematical convenience, we make the substitution $x = \gamma_t p_t / T$ and the single particle spectrum takes the form

$$\int \rho_1(\mathbf{p}) p_t dp_t = \frac{4a}{v_s} \left(\frac{dN}{dy}\right)_{y=0} \left(\frac{T}{\gamma_t}\right)^3 \int \sqrt{x^2+\zeta^2} K_1(\sqrt{x^2+\zeta^2}) I_1(v_s x) dx, \tag{3.38}$$

with $\zeta = \gamma_t m/T$. We can compare $\langle p_t \rangle$ calculated with (3.38) and constant temperature, to justify the approximation in Sec. 3.3. However, since this calculation has no azimuthal eccentricity, we cannot compare $v_2$, as it will be flat. This calculation will be used in chapters 5 and 6 to normalize the pair spectrum and cancel out the incorrect particle magnitudes.

# Chapter 4

## Color Glass Condensate

Following from the idea of gluon saturation, the theory of Color Glass Condensate (CGC) investigates the QCD regime of high parton density to describe the initial stages of a heavy ion collisions. Parton saturation indicates that at small Bjorken **x** (see Appendix A.3), the gluon density rises and fills the available phase space up to the saturation scale $Q_s$ [102, 103, 104]. This large density leads to a coherent state of gluonic matter, CGC, that can be treated with a classical approach to QCD [56, 57, 105, 106, 107, 108, 109, 110, 111, 112, 113, 114, 115]. This novel approach allows for first-principle investigation of QCD in a non-perturbative region. Furthermore, its application to heavy ion collisions provides both predictions for and quantitative descriptions of measured data [16, 19, 25, 36, 37, 59, 116, 117, 118, 119]. CGC theory also has significant phenomenological impact as, for example, the calculation of fluctuations in the initial state influence the measurement of elliptic flow (and therefore shear viscosity) as well as provide a natural origin of the long range correlations seen in the ridge, the focus of this work.

Including an initial CGC state, Ludlam and McLerran, in Fig. 4.1, illustrate the proposed stages of heavy ion collisions in terms of energy density vs. time. Notice that the maximum energy density is many times that of ordinary matter. The evolution of heavy ion collisions takes a path that starts at densities even greater than that of neutron stars and transitions through several phases. Each phase adds complication

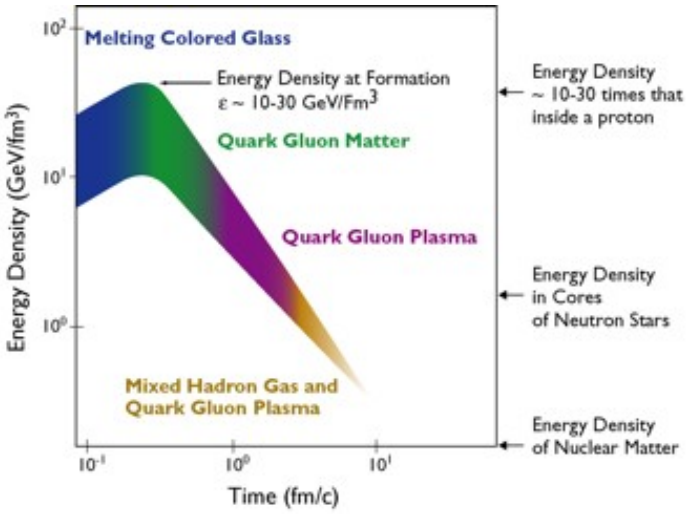


Figure 4.1: The various stages of a heavy ion collision [10]

to the understanding of such collisions, but also provides an opportunity to study the behavior of nature in energy regions not accessible through any other means. Much emphasis in the study of relativistic heavy ion collisions is placed on the understanding of QGP, but the QGP is a phase that is born from some initial conditions and modifies the final results with behaviors of its own. Using observed behaviors of QGP, one should be able to test how proposed initial conditions are manifested after freeze out. Correlation studies have proved to be a useful tool for this endeavor.

In this chapter, we outline the ideas of parton saturation and the calculation of the energy dependent saturation momentum $Q_s$ the primary scale in the CGC phase of QCD. We also discuss the emergence of color flux tubes and the Glasma phase following from CGC theory and their impact on the calculation of the ridge. The information in this chapter is primarily review with the exception that we reproduce selected calculations relevant to out correlation studies.

## 4.1 Saturation

We can build our understanding of parton saturation in terms of a proton consisting of constituent partons. At low energies, protons consist of three quarks which

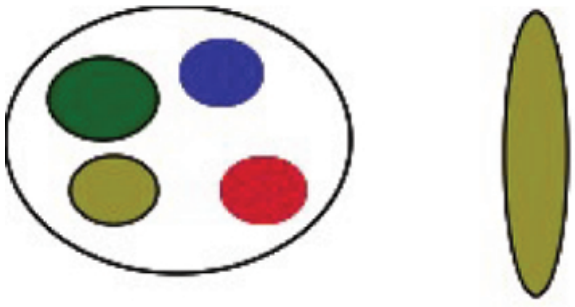


Figure 4.2: A schematic illustration of the wave functions of a baryon at low (left) and high (right) energies. [11].

carry a larger fraction of the total energy, and few gluons, which carry a smaller fraction. The size of the proton depends on the wave functions of the constituents. From the uncertainty principle, a parton's transverse size is inversely proportional to its momentum. It is seen from measurements of the total cross sections of $p + p$ and $p + \bar{p}$ collisions, that the size of the proton grows slowly, at most like $\ln^2(E/E_0)$, the Froissart bound [120]. We hypothesize from this that an increase in the proton's energy is not accompanied by a substantial increase in the momentum of the constituents, but rather an addition of gluons. This is illustrated in Fig. 4.2, where the wave function of a low energy baryon, on the left, is made up of the three valence quarks and few gluons, which we can distinguish. The same baryon at high energy is depicted on the right and has a wave function dominated by gluons. Adding an infinite amount of gluons with small fractions of the total momentum is equivalent to adding the infinite amount of energy required to bring a hadron to the speed of light.

Deep inelastic scattering (DIS) experiments at HERA provide evidence for this argument. DIS experiments map the partonic structure of hadrons with electromagnetic probes (i.e. electron+proton collisions). Fig. 4.3 shows the parton distribution of quarks and gluons in a proton as a function of **x**. At large **x**, up and down quarks dominate the distribution, but for decreasing **x**, the gluon contribution has a shocking

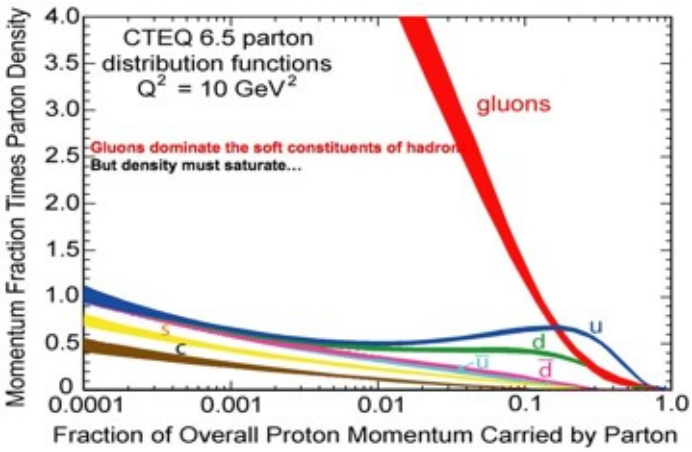


Figure 4.3: The quark and gluon composition of a proton for fixed $Q^2 = 10\ GeV$ [12].

exponential like increase. The rapid increase in gluon number combined with the slow growth in hadronic size support the saturation picture.

Further, measurements from HERA show that this effect is energy dependent, meaning that the gluon contribution depends on the momentum transfer of the probe, $Q^2$. Fig. 4.4 shows the gluon structure function, $xG(x, Q^2)$, as a function of $\mathbf{x}$, for different values of $Q^2$. Notice that the number of gluons increases with decreasing $\mathbf{x}$, and the effect is more pronounced with increasing $Q^2$.

Since the phase space of the proton is limited, the increase in gluon density with $Q^2$ implies that gluons saturate the phase space up to a momentum scale that is energy dependent. In other words, it is observed that the number of gluons grows with energy and the Froissart bound and unitarity limit the growth of the total cross section of the proton to $\ln^2(1/x)$. So, added gluons must inhabit regions of phase space not already occupied. Partons probed with small $Q^2$ correspond to larger values of $\mathbf{x}$, and added gluons can only fill in the remaining phase space which requires them to have a smaller value of $\mathbf{x}$ and larger $Q^2$. The scale that defines the distribution of glue is determined by the region of phase space that is already filled. This is the saturation scale, $Q_s$ . If the energy of the proton is increased, the phase space increases and gluons are added, but they must have a $Q^2$ greater than $Q_s$ (before

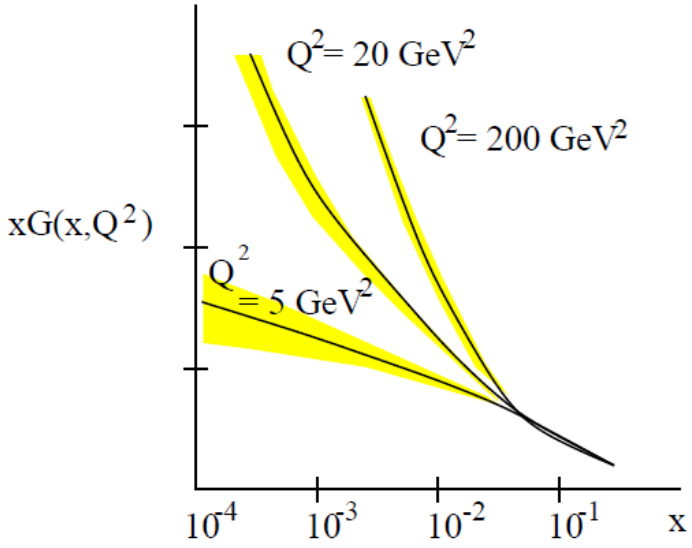


Figure 4.4: The distribution of gluons as a function of **x** as seen by HERA deep inelastic experiments [12].

the energy increase). Now a larger amount of phase space is filled, and since $Q_s$ is defined as the momentum scale below which the phase space is filled, it is larger; $Q_s$ increases with the energy of the proton.

We can visualize the saturation picture with the aid of Fig. 4.5. Similar to Fig. 4.2, we see on the left side the transverse distribution of partons at a lower energy, and the same on the right at a higher energy. On the left, gluons of some size fill the space, and we see that in adding energy, it is difficult to add more gluons of a fixed size. At this point, there are typically $1/\alpha_s$ partons of this size, and repulsive forces between gluons becomes a factor. So, in order to add gluons, they must fill in smaller spaces, and in this way the density gets larger. In adding more energy, gluons would have to fill yet smaller spaces, limiting the growth of the density.

A high energy proton is composed of constituents in two regimes, those above and below the saturation scale $Q_s$. We want to explore the behavior of interactions with partons in these two regimes. The gluon distribution as a function of $p_t$ is calculated in Refs. [109, 121, 122, 123], and shown in Fig. 4.6. High $p_t$ partons follow a power law distribution which is familiar to the perterbative region of QCD. The most significant

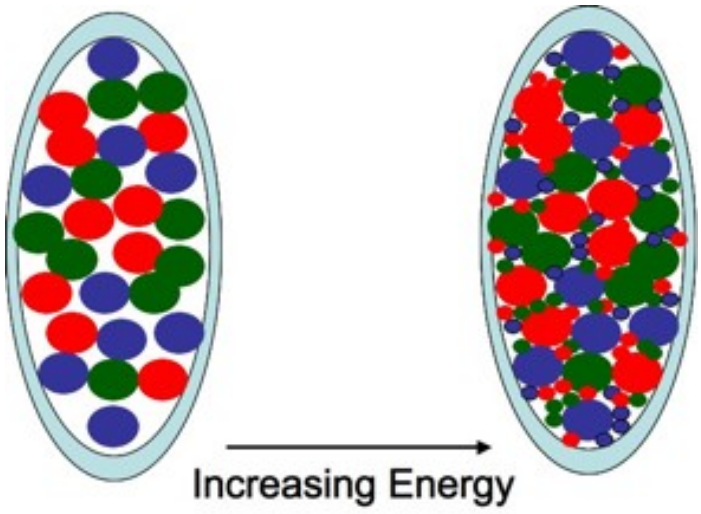


Figure 4.5: The density of gluons in the transverse plane as a function of energy [13, 14].

result of this calculation, however, is that the infrared (small $\mathbf{x}$, large wavelength) divergence of this behavior is cut off at the saturation scale. Below $Q_s$, the phase space density flattens as a logarithm of order $\ln(p_t/Q_{sat})/\alpha_s$. This is yet another indication of the saturation of gluons below $Q_s$. The flattening of the distribution is due to the cancellation of field strengths on size scales larger than their separation; the interactions between gluons prevent further growth of the numbers of gluons at larger $\mathbf{x}$.

The key feature of the saturation picture is that below the saturation scale, there is a densely packed coherent condensate of gluons that cuts off the infrared instabilities of the perturbative region of the gluon distribution. An interesting and perhaps crucial implication of this, is that when the density of particles is large enough that the inter-particle spacing is much smaller than that of the size of the system, all hadrons look the same at the same saturation scale. In principle, the radius of the system is irrelevant, meaning hadrons look no different than nuclei.

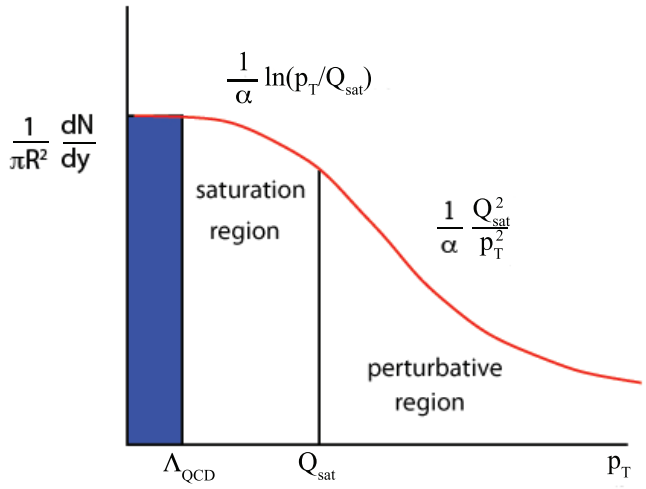


Figure 4.6: The gluon distribution function [15].

## 4.2 Saturation in Relativistic Nuclei

In relativistic nuclei, the saturation picture is nearly synonymous with the phenomenon known as shadowing. In a nucleus, small $\mathbf{x}$ partons originating from one nucleon have large wavelengths that can overlap with that of other small $\mathbf{x}$ partons from another nucleon at the same transverse position. From the uncertainty principle, interactions with partons at small $\mathbf{x}$ develop over large longitudinal distance, $z \sim 1/(mx)$, where $m$ is the nucleon mass. In the situation where $z$ becomes larger than the nuclear diameter, a probe cannot distinguish whether the parton originates from a nucleon at the front or back of the nucleus. All partons within a transverse area $\sim 1/Q^2$ participate in the interaction coherently, see Fig. 4.7 [16].

In the Lorentz contracted nucleus, partons from many nucleons at the same transverse position contribute to the gluon saturation. This brings to light the advantage of using relativistic nuclear collisions to study high density QCD matter; the density of gluons in a nucleus at RHIC is equivalent to that in a proton at much higher energy. Following the assumption that the gluon distribution scales with the number of nucleons, A, so $A \times xG(x,Q^2) = xG_A(x,Q^2)$, we can define the density of partons in

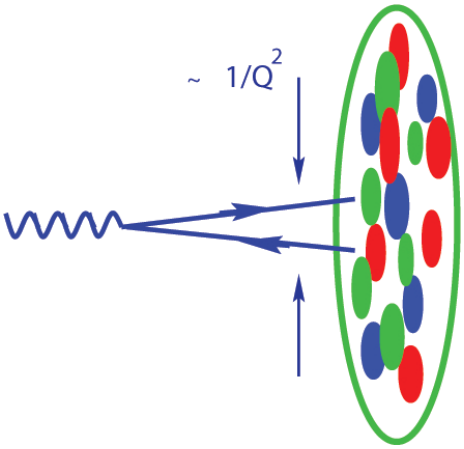


Figure 4.7: A hard probe interacting with the nuclear target resolves the area $1/Q^2$ where $Q^2$ is the square of the momentum transfer, and in the target rest frame the longitudinal longitudinal distance $\sim 1/(mx)$ ($m$ is the nucleon mass and $\mathbf{x}$ is the Bjorken variable [16].

the transverse plane as

$$\rho_{A} \simeq \frac{xG_{A}(x,Q^2)}{\pi R_{A}^2} \sim A^{1/3}, \tag{4.1}$$

where $R_{A}$ is the nuclear radius. The nuclear gluon distribution then also has two regimes corresponding to Fig. 4.6. If each parton can be probed with a cross section $\sigma \sim \alpha_s/Q^2$, then depending on the magnitude of the momentum transfer, Q, the atomic number, A, and the value of Bjorken $\mathbf{x}$, then we can identify the saturation region and perturbative region by:

- $\sigma\rho_{A} \ll 1$ - the perturbative QCD regime, where interactions of a probe can distinguish the wave functions of individual partons.

- $\sigma\rho_{A} \gg 1$ - the regime of the dense partonic system, where a probe interacts with many partons behaving coherently.

The border between the two regimes is the critical value of the momentum transfer, the saturation scale, where $\sigma\rho_{A} \simeq 1$ determines at which the parton system begins to

look dense to a probe. So, we have

$$Q_s^2 \simeq \alpha_s \frac{xG_{_A}(x,Q^2)}{\pi R_{_A}^2}. \tag{4.2}$$

Note that in the rest frame of the target, $Q_s$ can be understood as the burdening of the transverse momentum due to multiple rescatterings of the probe [16, 124].

This dense coherent gluonic matter, then is a different regime of QCD that is unexplored, but accessible in nuclear collisions at RHIC. The relativistic contraction of the nucleus provides not only dense and coherent gluonic fields, but also weak coupling that allows for a semi-classical treatment of the matter. It is precisely this matter that has been given the title of Color Glass Condensate.

## 4.3 Color Glass Condensate

The etymology of the term Color Glass Condensate is as follows:

- **Color:** Gluons have color.
- **Glass:** In the center of mass frame, fast moving particles are time dilated. The fields from the fast partons, however, generate the fields at smaller $\mathbf{x}$ through the evolution equations [56, 57, 105, 106, 107, 108, 109, 110, 111, 112, 113]. Through this generation, the time scale of the slower gluons evolve slow compared to their natural time scales. This is a property of glass. Ordinary glass is a liquid on very long time scales, but acts like a solid on shorter time scales [11].
- **Condensate:** There is a high occupation number of gluons. Due to the uncertainty principle, gluons at small $\mathbf{x}$ can have wave functions extending the size of the nuclear radius. These gluons can be packed until their phase space density is so high that interactions prevent more gluon occupation. This forces

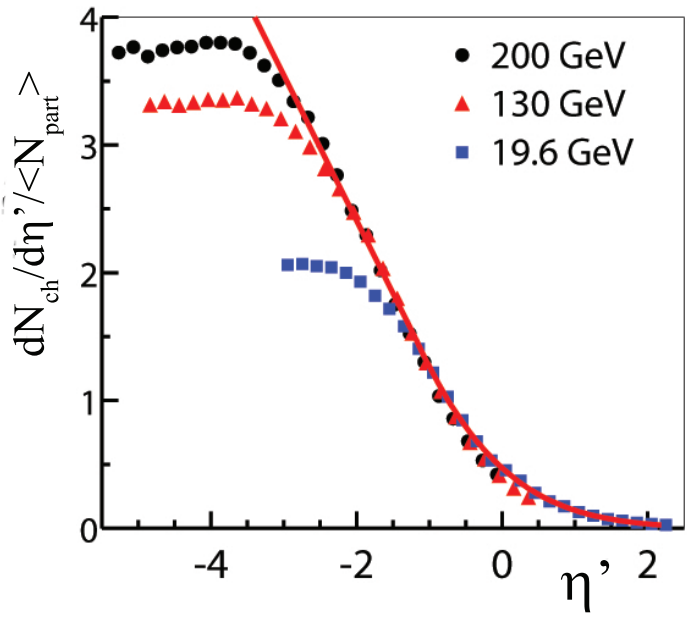


Figure 4.8: Limiting fragmentation as illustrated in the PHOBOS experimental data on Au+Au collisions at RHIC [17]

at increasingly high density the gluons to occupy higher momenta, and the coupling becomes weak. At high densities, with weak coupling, these gluons behave coherently, forming a Bose-Einstein like condensate.

Since the density is high, the coupling between gluons is weak. In other words, the separation between gluons is small and the energy is high, so $\alpha_s << 1$. This is precisely the condition that allows for a classical approach to the problem. Also, weak coupling does not mean weak effects. Since we can treat gluonic fields classically, their wave functions add in a coherent way, analogous to standing electromagnetic waves. This coherence allows for many small effects to add to large effects. A more common example of this behavior is seen is gravity. The gravitational force from one particle is very weak, but a superposition from some huge mass can produce an extremely large force [11].

We can find empirical evidence for the glassy nature in limiting fragmentation as measured by the PHOBOS collaboration and shown in Fig. 4.8 [17, 125]. The data in

the image has been shifted so that the rapidity of one of the nuclei is at zero. In the center of mass frame, the rapidity of nuclei are $\sim \pm 6$; in the frame of one nucleus, the other nucleus would have a rapidity of $\sim \pm 12$. In Fig. 4.8, what we call the central rapidity region is centered at $-6$. Measurements of Au+Au multiplicities are shown for three different center of mass energies. All three energies share the same behavior. Starting at rapidities near that of the beam, the curves rise, but flatten off near the central rapidity region, the region corresponding to small $\mathbf{x}$. The interesting attribute is that for all three energies, the fast degrees of freedom scale the same. In simpler terms, even though Au+Au collisions at center of mass energies of 19.6 GeV and 200 GeV are different by an order of magnitude, they seem to produce the same number of "fast" high rapidity, large $\mathbf{x}$ partons per participant. The scaling breaks in the central rapidity region, where the multiplicity growth flattens earlier at lower energies. This indicates that there is a separation between fast and slow degrees of freedom that changes with energy. This separation fits in the CGC picture where the mathematical development of the increase in small $\mathbf{x}$ gluon density is sourced from the current of fast particles. The nonlinear growth in the multiplicity at small $\mathbf{x}$ is reminiscent of the slow growth in gluon density of the CGC despite the increase of sources.

Increasing the energy seems to only lead to the addition of lower $\mathbf{x}$ degrees of freedom as sources; the scaling holds to smaller rapidity. The connection to the separation between the energy of the source partons and the partons below $Q_s$ is controlled by the renormalization group formalism [58, 110, 14, 126, 127, 128, 129, 130, 131, 132].

This interpretation of Fig. 4.8 suggests another important point, the multiplicity of the central rapidity region is governed by interactions with the dense gluonic (CGC) matter at small $\mathbf{x}$. We can now draw the picture of soft particle production emerging from collisions of the CGC in each nucleus. Because of the Lorentz contraction of

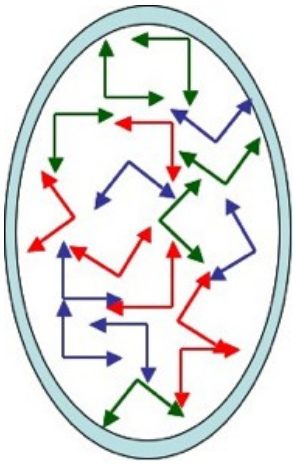

Figure 4.9: The color electric and magnetic fields on a sheet of colored glass [13, 14, 18].

the nuclei, we can think of the CGC matter as a thin sheet of high density matter. The gluon wave functions are tightly packed and represented by color electric and magnetic fields that are purely transverse, such that $\vec{E} \perp \vec{B} \perp \hat{z}$, and random over the transverse plane, as shown in Fig. 4.9. Due to saturation, these fields have maximal strength $E^2 \sim B^2 \sim 1/\alpha_s$.

The representation of a nuclear collision involves solving classical Yang-Mills equations before and after the collision. Equations for color fields in high energy hadronic collisions have been developed in Refs.[126, 127, 133, 134] and numerically solved for the rapidity independent case in Refs.[110, 128, 129, 135, 136].

During the time CGC sheets pass through each other, each sheet develops a topological charge since each sheet has a random orientation of color electric and magnetic fields, the collision allows for $\vec{E} \cdot \vec{B} \neq 0$ [137, 138, 139, 140, 141, 142]. As the sheets carry away this charge and their separation becomes large, the once transverse fields become longitudinal between them. The orientation of longitudinal fields is dubbed the "Glasma", and depends on the orientation of fields before the collision. The Glasma is a pre-equilibrium phase, whose fields source the partons that eventually thermalize into quark gluon plasma.

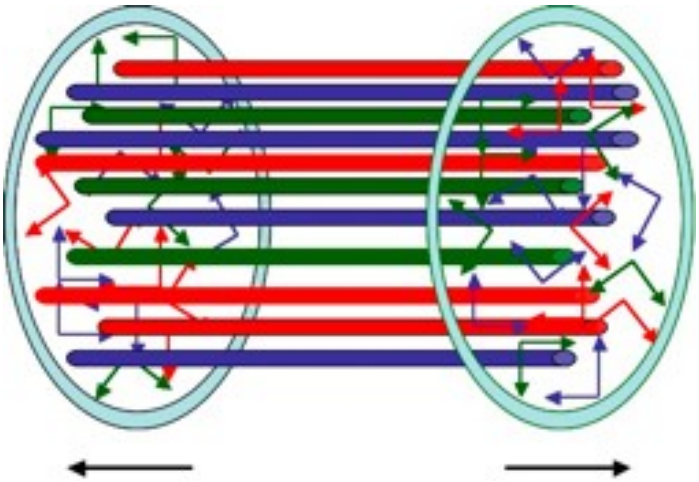

Figure 4.10: Two sheets of colored glass after their collision and the longitudinal color flux tubes generated by the collision [13, 14, 18].

## 4.4 Flux Tubes and Glasma

Almost instantaneously after a collision of two nuclei, Color Glass Condensate (CGC) theory predicts that the transverse fields of each nucleus are transformed into longitudinal fields that are approximately uniform in rapidity, as shown in Fig. 4.10, [56, 57, 58]. The fields, which are random over transverse distances larger than $Q_s^{-1}$ (where $Q_s \sim 1 - 2$ GeV at RHIC), comprise a series of flux tubes. Given a dense distribution of flux tubes, the system enters a Glasma pre-thermalization phase where flux tubes develop quantum instabilities and evaporate into particles.

With this in mind, we can take a new look at the first stages of our schematic illustration of heavy ion collisions, Fig. 2.3. We can view the initial state of the nuclei as CGC sheets moving toward each other. The initial singularity corresponds to the moment when the sheets pass through each other. It is useful to visualize the time frame of the system in terms of a light cone diagram, as in Fig. 4.11. In the first 0.1 fm/c, the amount of time it takes the speed of light to traverse the CGC, field fluctuations on the quantum scale form. These fluctuations are stretched by rapid longitudinal expansion to the scale of the collision, manifested as topological charges and connecting longitudinal flux tubes. It is important to note here that the

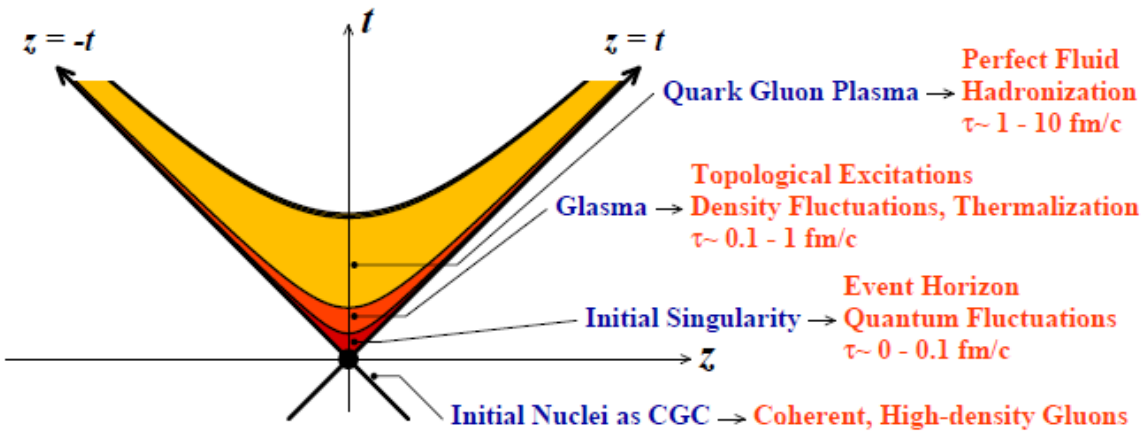


Figure 4.11: The stages in the evolution of matter produced in high energy heavy ion collisions following from a CGC- Glasma picture. Image from [11]

number and transverse position of flux tubes fluctuates from event to event. This has significant ramifications to our correlation picture, see Secs.4.6, and 5.2. This is the Glasma phase, which is left out of Fig. 2.3, but represents the transition from local emission of partons from individual flux tubes, to equilibrated QGP.

The Glasma description describes many of the features of the matter produced in the high density environment in nuclear collisions, most notably, final state multiplicities [16, 19, 20, 116, 117]. The connection between flux tubes, fluctuations, and multiplicity has significant impact on our description of the correlations that form the ridge.

## 4.5 Hadron Multiplicities

In the saturation picture, the total multiplicity of gluons produced in a collision follows from dimensional reasoning as in Ref. [19]. The factor $1/\alpha_s$ arises because the multiplicity may be determined by solving a classical problem, or alternatively, because the phase space density of gluons in the initial state has the same factor [18]. We imagine the Glasma to be filled with flux tubes of large longitudinal extent but small transverse size $\sim \pi/Q_s^2$. Each flux tube yields a multiplicity of $\sim \alpha_s \pi (Q_s)^2$

gluons. The number of flux tubes is proportional to the transverse area $S_A \sim \pi R_A^2$ divided by the area per flux tube, $\pi Q_s^{-2}$. The rapidity density of gluons is therefore

$$dN/dy \sim {\alpha_s}^{-1} Q_s^2 R_A^2, \tag{4.3}$$

where the strong coupling constant, $\alpha_s(Q_s)$, depends on $Q_s$, and is to leading order

$$\alpha_s = \frac{4\pi}{11 - \frac{2}{3}N_c} \frac{1}{ln(Q_s^2/\Lambda_{QCD}^2)}. \tag{4.4}$$

Again we see the that the saturation scale plays a deterministic role. Indeed, Ref. [19] finds that the initial gluon density scales to the final state multiplicity with a constant number near unity. This implies "parton-hadron duality", meaning the dynamical evolution of the system doesn't change the overall multiplicity much. The "parton liberation" coefficient, $c = 1.23 \pm 0.20$ found in Ref. [19], compares well with other calculations [135, 143].

To construct an equation for the saturation scale, we follow Ref. [19], which follows from methods in Refs. [16, 20, 102, 104, 103, 56, 105, 106, 109, 113, 134, 133, 121, 114, 144], which were motivated in previous sections. We write down

$$Q_s^2 = \frac{8\pi^2 N_c}{N_c^2 - 1} \alpha_s(Q_s^2) x G(x, Q_s^2) \frac{\rho_{part}}{2}, \tag{4.5}$$

where $N_c = 3$ is the number of colors, and the density of participants $\rho_{part}$ is defined in Appendix B. The density of participants is divided by 2 to get the density of nucleons in a single nucleus that participate at a given impact parameter. The gluon distribution function, $xG(x, Q^2)$, to leading order from global DIS fits, from Ref.[145], is

$$xG(x, Q^2) = 31.2 x^{0.390} (1 - x)^{6.18} (1 - 5.23\sqrt{x} + 7.33x) \tag{4.6}$$

taking $x \simeq 2Q_s/\sqrt{s}$. Ref.[19] solves (4.5) by iterations for Au+Au collisions at $\sqrt{s} =$

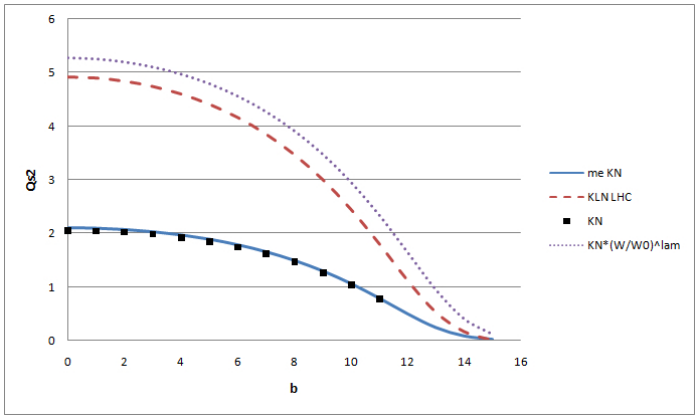


Figure 4.12: Comparison of the calculation of $Q_s^2$, eq.(4.5) (solid line), to that in Ref.[19] (solid squares). The dotted line is the LHC prediction for Pb+Pb at $\sqrt{s} = 5500\ GeV$ scaling (4.5) with (4.7). The dashed line is the KLN prediction (4.9) from Ref.[20] at $y = 0$.

130 $GeV$. We reproduce that procedure with agreeing results, as shown in Fig. 4.12.

The energy dependence of $Q_s$ follows the scaling noticed in HERA data [124, 146, 147, 148], where

$$Q_s^2(x) = Q_0^2 \left(\frac{x_0}{x}\right)^{\lambda} = Q_0^2 \left(\frac{W}{W_0}\right)^{\lambda}, \tag{4.7}$$

with W=$\sqrt{s}$. This scaling has been used to make predictions for both RHIC at 200 GeV, and LHC energies, taking initial values of $Q_{s0}^2 = Q_s^2(W = 130\ GeV)$ [16, 19, 20, 116, 117].

A model starting with CGC initial conditions followed by a hydrodynamic afterburner finds excellent agreement with Au+Au collision multiplicities at $\sqrt{s} = 200\ GeV$, using $\lambda = 0.2$, see Fig. 4.13 [21]. However, using the value $\lambda = 0.25$ as determined by HERA experiments [146, 147, 148] still lands the result within the error bars [21].

There is a fundamental difference between the CGC approach to multiplicity calculation and the conventional "soft plus hard" picture. The latter scenario assumes that some fraction $x$ of the multiplicity $n_{pp}$ measured in p+p collisions is due to hard

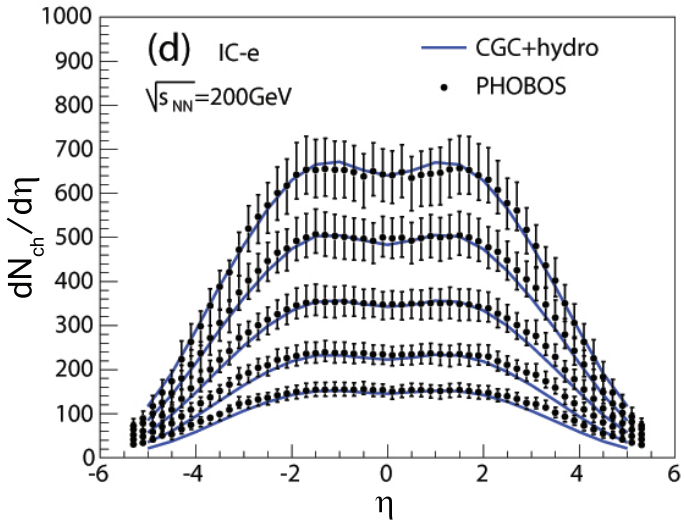


Figure 4.13: Comparison of pseudorapidity distributions in Au+Au $\sqrt{s} = 200GeV$ collisions from PHOBOS [17] to a model of CGC initial conditions with a hydrodynamic afterburner [21] for different centralities. The impact parameters from top to bottom are: 2.4, 4.5, 6.3, 7.9, and 9.1 fm.

processes. The remaining fraction $(1 - x)$, is due to soft processes. The parameterization

$$\frac{dN}{d\eta} = (1 - X(s))n_{pp}\frac{\langle N_{part}\rangle}{2} + X(s)n_{pp}\langle N_{coll}\rangle, \tag{4.8}$$

assumes further, that in nuclear collisions, the hard fraction scales with the number of binary collisions, $N_{coll}$, and the soft fraction scales with the number of participants, $N_{part}$. This formulation was shown to describe $\sqrt{s} = 130\ GeV$ Au+Au data quite well [19], but has a particular behavior with change in energy. The $p+p$ multiplicity follows the parameterization $n_{pp} = 2.5 - 0.25\ln(s) + 0.023\ln^2(s)$ [149, 150], and aside from the nucleon-nucleon cross section's increase with energy, the minijet fraction, $X(s)$ is required to increase to agree with RHIC data at higher energies [16]. So, in the soft plus hard picture, we expect growth with energy, reflecting the minijet cross section, where in the CGC picture, the dependence of multiplicity in the central rapidity region is determined by the running of $\alpha_s$ [30].

Although both approaches have differences small enough that RHIC data cannot distinguish them, the difference in trends is already noticeable [16]. The KLN pre-

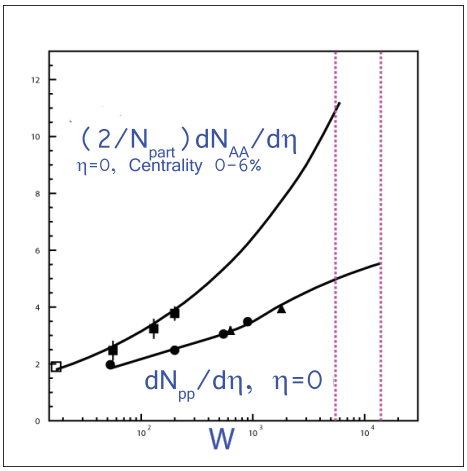


Figure 4.14: Energy dependence of charged hadron multiplicity from Ref.[20]: $dN/d\eta$ at $\eta = 0$ in p+p collisions and $(2N_{part})dN/d\eta$ at $\eta = 0$ for central nucleus-nucleus collsions. The vertical dotted lines mark LHC energies for Pb+Pb (W=5500 GeV) and p+p (W=14000 GeV). The experimental data are from Refs.[22, 23].

dictions for the LHC [20] depend on a more sophisticated calculation of $Q_s^2$. They find

$$Q_s^2(y, W) = \Lambda_{QCD}^2 \exp\left(\sqrt{2\lambda \ln(Q_{s0}^2/\Lambda_{QCD}^2)[\ln(W/W_0) + y] + \ln^2(Q_s^2(W_0)/\Lambda_{QCD}^2)}\right) \tag{4.9}$$

which includes dependence on rapidity. This dependence allows for the possibility that one of the colliding partons is in the saturation region and the other is not. In work presented here, we always consider both colliding partons to be in the saturation region. This corresponds to the central rapidity region where $y \approx 0$ in (4.9), and the gluon multiplicity corresponds to (4.3). The KLN predictions for multiplicities at the LHC are shown in Fig. 4.14 and Fig. 4.15.

The LHC will offer much higher energies, but the saturation picture predicts a slow growth in parton density. However, the saturation scale should be large enough that there would be a significant difference from a jet dominated picture. Fig. 4.14 shows p+p and A+A values of $dN/d\eta$ at $\eta = 0$ as a function of center of mass energy. There is agreement with current data [22, 23], but the growth with energy is small

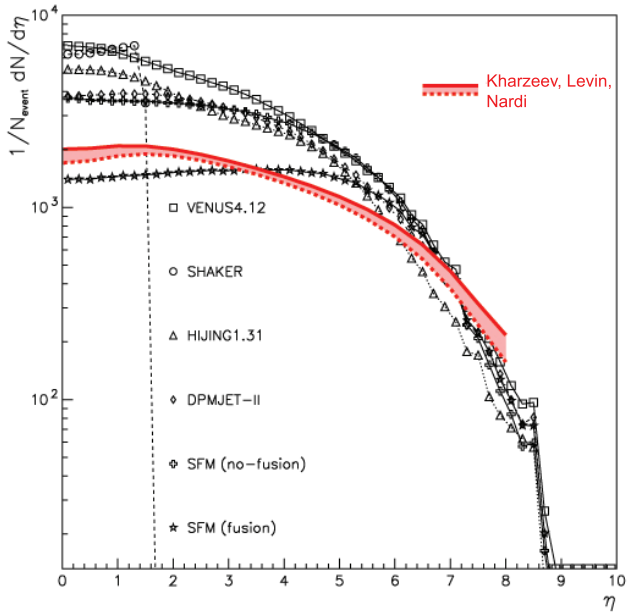


Figure 4.15: Comparison of the Kharzeev, Levin, and Nardi [20] prediction for charged hadron multiplicities in central ($b \leq 3fm$) Pb+Pb collisions with results from other approaches as given in Ref.[24].

compared to other models. For example, at maximum RHIC energies Au+Au collision yield a central multiplicity of $dN/d\eta \sim 700$, and the prediction for LHC energy, as extrapolated from Fig. 4.14, is $dN/d\eta \sim 2000$. From Fig. 4.15, we see comparisons to other predictions. In particular, we can compare to HIJING, a pure jet model, which predicts a central value $\sim 2-4$ times larger.

## 4.6 CGC and Correlations

The CGC-Glasma picture has many implications in our understanding of the stages of relativistic heavy ion collisions. The CGC formalism builds from fields of large $\mathbf{x}$ partons as sources of those at small $\mathbf{x}$. Because of this, it is convenient to use the light cone variables reviewed in Appendix A.1. The Bjorken approach to longitudinal expansion leads to a correspondence between rapidity and pseudorapidity

via

$$y = \frac{1}{2}\ln\left(\frac{p^+}{p^-}\right) \sim \ln\left(\frac{p^+}{m^t}\right) \sim \ln\left(\frac{x^+}{\tau}\right) \sim \eta \tag{4.10}$$

This is consistent with the idea sketched in Fig. 3.2. This implies that particles created at some spatial rapidity are essentially created with approximately the same momentum space rapidity. This has significant impact on the picture drawn later in Sec.5.1, since particles born at very large pseudorapidity differences are seen to have correlation [2, 3, 4, 5, 28, 48, 49, 50, 52, 53, 54, 55].

In the CGC picture we link these long rage correlations to the long longitudinal flux tubes, which are the sources of partons [25, 36, 37, 59]. Since, in our picture, correlated particles come from the same flux tube, it is important that a collection of flux tubes emits a multiplicity of partons that is preserved throughout the hydrodynamic evolution of the QGP and describes the final state, as seen in Fig. 4.13 [21]. Following the idea of parton hadron duality, we do not consider effects from resonances or $2 \to 3$ process which would smear out correlations.

We describe the near side ridge as a consequence fluctuations formed at early stages which are modified by later stage transverse flow. Other similar models taking initial conduits from individual p+p collisions or string fragmentation are able to qualitatively describe features of the ridge [60, 65]. This validates that fluctuating initial conditions are indeed the primary source of final state momentum correlations. We propose that local parton density fluctuations at early stages arise from the dissolution of individual flux tubes. Aside from the necessity that these fluctuations be longitudinally long, their transverse size, number, and individual multiplicity ultimately determine the strength of the observed correlation. We will show in Chapter 5, that the CGC-Glasma formalism provides an explicit description of these features and provides a remarkable agreement with correlation data.

# Chapter 5

# The Soft Ridge

Two particle correlations measurements find an excess of correlated particle pairs that is narrow in relative azimuthal angle, $\phi$, and broad in relative (pseudo)rapidity, $\eta$ . Experiments find this ridge like shape in correlation measurements with and without a jet trigger. As described in Ch. 1, the untriggered "soft ridge" represents correlations of particles with all ranges of momentum. The word "soft" reflects the fact that the majority of the particles contributing to the measurement emerge from non-perterbative processes. As we will see in in Ch. 6, this distinction is important when comparing the soft and hard ridge.

We argue in this chapter that the soft ridge originates from initial state spatial correlations that experience later stage transverse flow. In Sec. 5.1, we begin with a brief description of some features of two particle correlations in heavy ion collisions. One of the primary motivations behind this work is that the ridge exhibits a long range behavior in $\eta$ that challenges all potential explanations of the phenomenon [29]. In Sec. 5.2, we discuss how this long range behavior arises naturally from CGC-Glasma initial conditions. We then focus on the consequences CGC-Glasma initial conditions have on the construction of our correlation function and the overall correlation strength. In Sec. 5.3, we take into account the effects of radial flow. Finally, we show our results in Sec. 5.4.

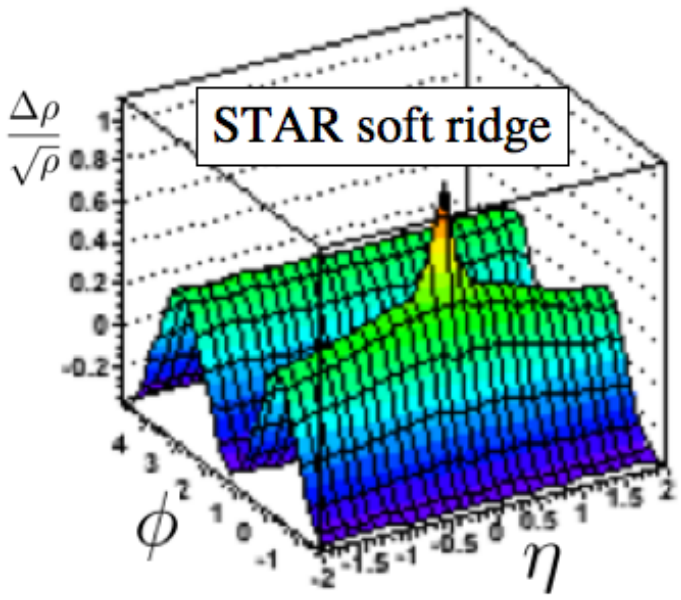


Figure 5.1: Image of the STAR measured soft ridge $19-28\%$ central [1].

## 5.1 Some Features of Correlations

The full correlations landscape is a complicated 2-D structure as shown in Fig. 5.1, taken from Ref. [1]. The coordinates of the correlation structure indicate relative units between particle pair momenta. The azimuthal difference between two particle's momenta is $\phi = \phi_1 - \phi_2$. Similarly, the relative pseudorapidity is defined as $\eta = \eta_1 - \eta_2$. The "near-side" structure is centered at $\phi = \eta = 0$ and represents the combination of several sources of correlations including purely random correlations, flow, jets, and density fluctuations.

If particles are initially randomly deposited in the medium, and do not flow, then correlations would obey Poisson statistics, mathematically allowing the pair distribution to factorize into two single-body distributions, i.e. $\rho_2 \rightarrow \rho_1\rho_1$. This case corresponds to particle pairs having only random correlation and should be, on average, constant for all $\eta$ and $\phi$. This would effect the overall offset of the correlations structure in Fig. 5.1.

If we examine the same situation, but allow the particles to flow, then momentum

conservation demands that transverse momentum gains are compensated by equal gains at an angular difference of $\pi$. We expect correlations of the form of $\cos\phi$ from transverse flow, and $\cos 2\phi$ from anisotropic flow, see Sec. 2.3. In the case of the soft ridge, experimentalists extract the magnitudes of these effects from the correlation landscape and find $v_2$ values consistent with other measurements [151]. In the case of the hard ridge the correlations of the form $\cos 2\phi$ are subtracted using the Zero Yield At Minimum (ZYAM) method [3].

Conversely, if all particles come from jets, the emission of particles is a cone opening in the direction of a leading particle. In this case, all particles in the same jet have the same origin - the position of the collision producing the jet. Jet particles' momenta are also correlated, as indicated by the existence of a cone, since particles fragmenting from the leading particle are co-moving with the leading particle. Here, one would expect correlated pairs to have small $\phi$ and $\eta$. Indeed this is seen in $p+p$ and peripheral collisions, as well as the jet peak sitting on the hard ridge. The jet peak exists in the soft ridge as well, however it appears to be overwhelmed by the anomalous correlations that comprise the ridge [26].

STAR experimentalists decompose the 2-D correlation structure using a multicomponent fit [1]. The fit accounts for correlations from many sources such as momentum conservation, elliptic flow,and experimental effects. After subtracting these components an anomalous structure remains on the near side, the ridge. The ridge is fit with a 2-D Gaussian as shown on the right side of Fig. 5.6 and is the primary subject of interest in this dissertation.

The most striking feature of the ridge measurement is that, for central collisions, the ridge appears to extend to $\eta > 2$ where causality limits kinematic transport. The PHOBOS measurement of the triggered ridge, as shown in Fig. 5.2, provides further support for the existence of long range correlations [5]. The dashed blue line in the right panel of Fig. 5.2 indicates the correlation structure from PYTHIA simulations

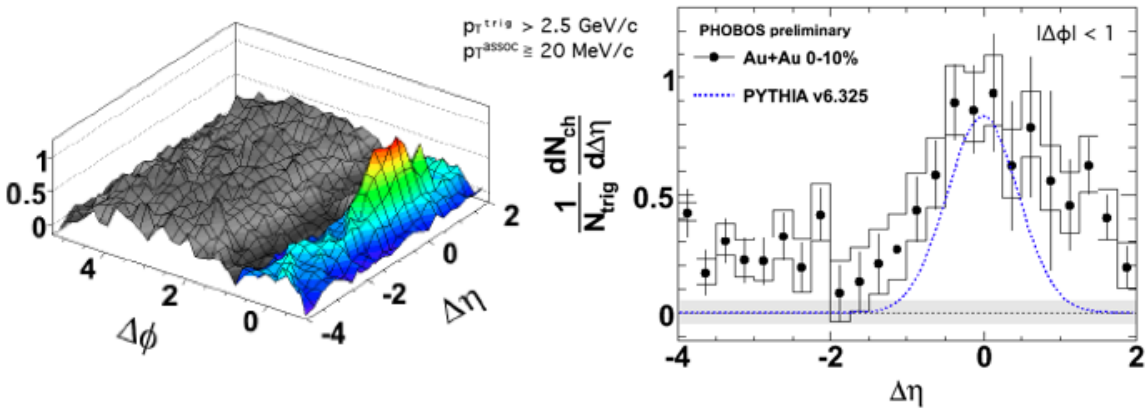


Figure 5.2: PHOBOS measurement of the triggered ridge [5]. The left figure is the 2-D correlation structure with relative azimuthal angle $\Delta\phi$ and relative rapidity $\Delta\eta$ where the away side is shaded out. In the right figure is the solid dots indicate yield of pairs integrated over the angle $\|\Delta\phi\| < 1$, and the dashed blue line is the correlation yield from PYTHIA.

representing the expected correlations from jets. Correlations from jets alone are zero at $\|\eta\| > 2$ where the data in central Au+Au collisions is consistently positive in the range $-4 < \eta < 2$. In this chapter, we present an explanation of long range correlations following Ref. [36]. We find excellent comparison to available STAR data although STAR rapidity acceptance does not reach to long range.

## 5.2 Flux Tubes, Glasma, and Correlations

Correlations over several rapidity units can only originate at the earliest stages of an ion collision when the first partons are produced [25]. The rapid longitudinal expansion can modify initial quantum fluctuations, stretching them to distances not causally connected. Hydrodynamics and other later-stage effects can modify these correlations but are limited to a horizon of $\sim 1-2$ rapidity units. Analogous to superhorizon fluctuations in the cosmos, these long range correlations can therefore reveal the "little bang" in each nuclear collision at its birth.

The red and green shaded regions in Fig. 5.3 represent the history of all possible events influencing particles A and B respectively. The history of these particles de-

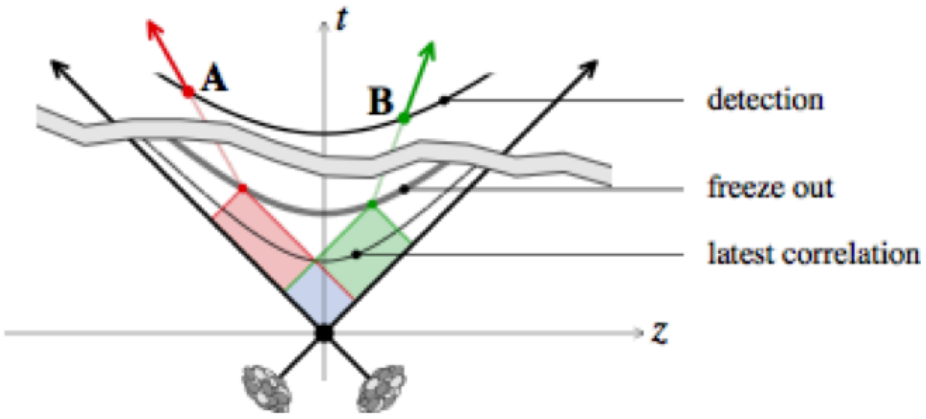


Figure 5.3: The shaded areas represent the light cones of events causally related to particles A and B. Image from Ref. [25]

pends on their rapidity. Particles with larger rapidity follow more closely to the beam line and freeze out later. Particle A has a larger rapidity than B, and consequently, the shaded red region is slimmer than the green. Particles A and B could only gain correlations in the blue shaded region, where their light cones overlap. Larger rapidity differences reduce the overlap region, requiring any correlations to occur at earlier times.

Almost instantaneously after a collision of two nuclei, CGC theory predicts that the transverse fields of each nucleus are transformed into longitudinal fields that are approximately uniform in rapidity [105, 57, 58]. These fields, which are random over transverse distance larger than $Q_s^{-1}$, where $Q_s \sim 1 - 2$ GeV is the saturation scale, comprise a series of flux tubes. These tubes are then stretched by the rapid longitudinal expansion, as illustrated in Fig.5.4.

We attribute the source of long range correlations to longitudinal flux tubes predicted by the theory of Color Glass Condensate. Long range rapidity correlations arise because particles from the same flux tube start at nearly the same transverse position, regardless of rapidity.

In a nuclear collision, the number of tubes is proportional to the transverse area $R_A^2$ divided by the area per flux tube, $Q_s^{-2}$. The high density of flux tubes begin

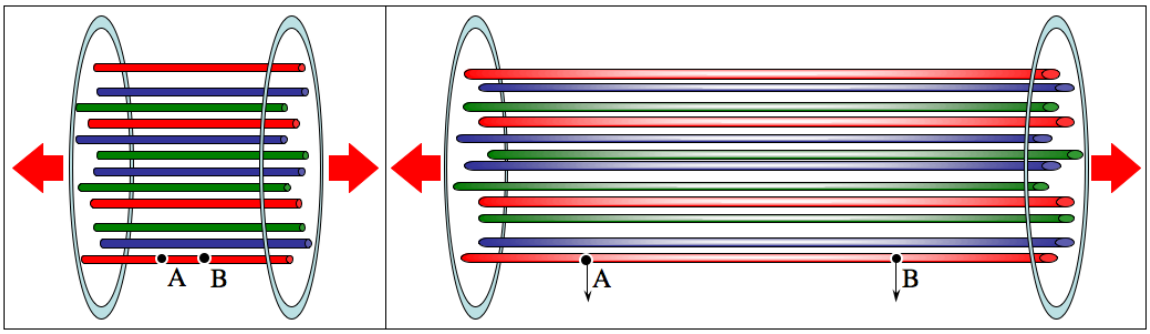


Figure 5.4: Cartoon of longitudinal flux tubes just after a nuclear collision (left) and after $\propto 10^{-1} fm/c$ (right). The Glasma phase begins immediately as the hight density of tubes begin to thermalize into partons. Analogous to Fig. 5.3, partons A and B have an early time (in this case, zero time) correlation and rapid longitudinal expansion stretches the tube causally separating A and B while preserving the correlation.

to emit partons, indicating a Glasma phase. Only partons from the same tube are correlated and we neglect correlations between neighboring tubes.

In a Glasma phase (see Ch. 4), we imagine a closely packed system of flux tubes and not strictly distinct due to saturation. They are however uncorrelated for $r_t > Q_s^-1$. This is the essential feature for this work. The Glasma changes into plasma as particles form from fields and thermalize.

We characterize correlations in the Glasma and later in the evolution using the spatial correlation function

$$c(\mathbf{x}_1, \mathbf{x}_2) = n_2(\mathbf{x}_1, \mathbf{x}_2) - n_1(\mathbf{x}_1) n_1(\mathbf{x}_2), \tag{5.1}$$

where $n_1$ and $n_2$ are the single and pair densities. In the absence of correlations, $n_2(\mathbf{x}_1, \mathbf{x}_2) \to n_1(\mathbf{x}_1) n_1(\mathbf{x}_2)$ so that $c$ vanishes. The integral of $n_2$ over both positions gives the number of pairs averaged over events $\langle N(N-1) \rangle$. When correlations are negligible, the integral of $c$ vanishes – as it must – because $N$ follows Poisson statistics and, therefore, $\langle N(N-1) \rangle \to \langle N \rangle^2$.

We take flux tubes to be approximately independent of rapidity, and write the correlation function depending only on the relative transverse position $\mathbf{r}_t = \mathbf{r}_1 - \mathbf{r}_2$ as

well as the average $\mathbf{R}_t = (\mathbf{r}_1 + \mathbf{r}_2)/2$. The correlation length in $r_t$ is roughly the flux tube size $\sim Q_s^{-1}$, while the correlation length in $R_t$ of order of the transverse system size $R_A$. For $Q_s^{-1} \ll R_A$ we take the correlation function to be point-like in $r_t$ and broad in $R_t$, writing

$$c(\mathbf{x}_1, \mathbf{x}_2) = \mathcal{R}\, \delta(\mathbf{r_t})\rho_{_{FT}}(\mathbf{R}_t). \tag{5.2}$$

Here, $\rho_{_{FT}}(\mathbf{R}_t)$ describes the transverse distribution of flux tubes in the collision volume, which we assume follows the thickness function of the colliding nuclei

$$\rho_{_{FT}}(\mathbf{R}_t) = \kappa \left(1 - \frac{R_t^2}{R_A^2}\right). \tag{5.3}$$

Here $\kappa = 2\langle N\rangle^2/(\pi R_A^2(\Delta y)^2\tau^2)$ and $R_t \leq R_A$. Integrating both sides of (5.2) with respect to $r_t$ and $R_t$, we find

$$\langle N\rangle^2\mathcal{R} = \int c\, d^3x_1 d^3x_2 = \langle N^2\rangle - \langle N\rangle^2 - \langle N\rangle. \tag{5.4}$$

To see how $\mathcal{R}$ depends on $Q_s$, think of each flux tube as a source that produces particles with a mean multiplicity $\mu$ and variance $\sigma^2$. For $K$ flux tubes, the mean multiplicity is $\mu K$ and the variance is $\sigma^2 K$. If $K$ fluctuates from event to event, then the mean multiplicity is $\mu\langle K\rangle$ and the variance is $\sigma^2\langle K\rangle + \mu^2(\langle K^2\rangle - \langle K\rangle^2)$. Therefore

$$\mathcal{R} = \frac{\sigma^2 - \mu}{\mu^2}\frac{1}{\langle K\rangle} + \frac{\langle K^2\rangle - \langle K\rangle^2}{\langle K\rangle^2}. \tag{5.5}$$

Particle production from a flux tube is a Poisson process, since the flux tube is a coherent state. It follows that $\sigma^2 = \mu$, so that the first contribution vanishes. For large $K$, the second term is $\propto \langle K\rangle^{-1}$.

We combine these results to obtain a scaling relation for the integrated strength

of correlations in the Glasma

$$\mathcal{R} \propto \langle K \rangle^{-1} = (Q_s R)^{-2}, \tag{5.6}$$

a result supported by momentum-space calculations in [25]. In contrast, the mean multiplicity in a rapidity interval scales as $\alpha_s (Q_s)^{-1} Q_s^2 R^2$; see eq. (4.3). This difference will prove significant later. We comment that (5.6) and similar CGC relations may not quantitatively describe $p+p$ or peripheral collisions at the energies studied here, although phenomenological string models may apply.

## 5.3 The Blast Wave and Correlations

We now turn to discuss the impact of these long range correlations on the final-state particle correlations. As the partons emitted from these flux tubes locally equilibrate, transverse flow builds. To describe the effect of thermalization and flow on the pair correlation function at freeze out, we generalize the common blast-wave model described in Ch. 3.

In Ch. 3 we stressed that transverse flow provides a radial boost that depends the final transverse boost depending on the radial position following (3.1). Here, fluctuations in particle density are boosted radially based on their initial radial position, focusing particles to have narrower relative azimuthal angles. Voloshin has long stressed the connection between flow and $p_t$ correlations [60].

Figures 5.5 and 5.6 illustrate the effect of this phenomenon on angular correlations. The top of Fig. 5.5 is a cartoon of the dynamical evolution of two selected elements in a transverse slice of the system. We start with *a*) a distribution of color flux tubes, in the Glasma phase, and in *b*) the tubes have disintegrated into small locally equilibrated fluid cells. These cells receive a radial boost depending on their radial position indicated in the images by the white vectors. In step *c*), transverse flow

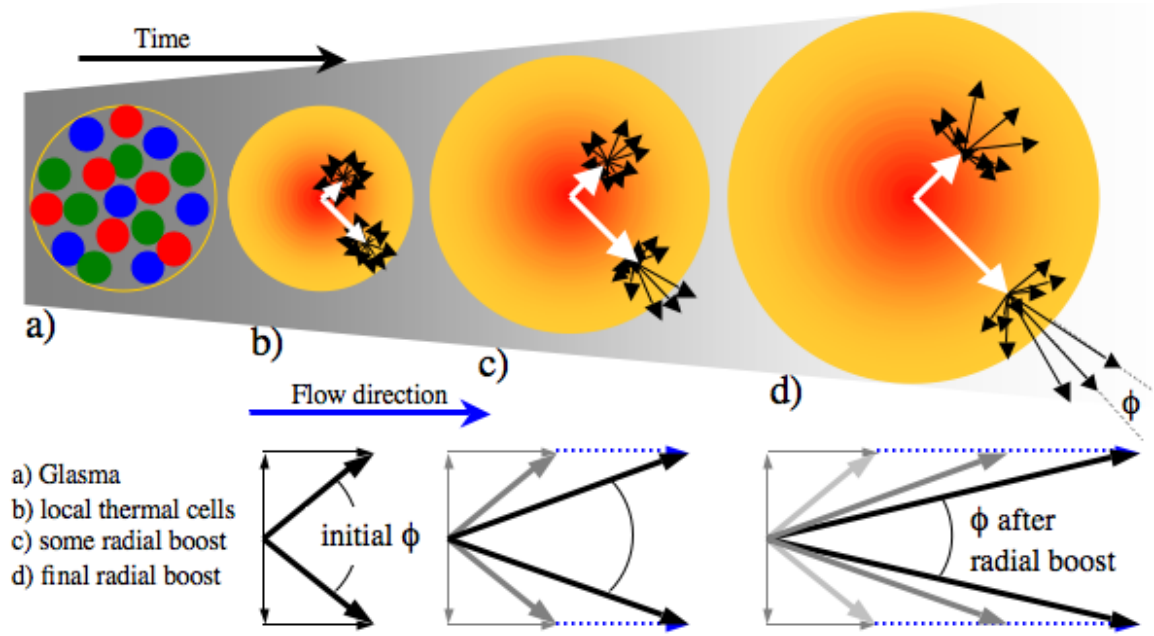


Figure 5.5: (top) Dynamical evolution of the angular correlation enhancement from transverse flow, and (bottom) vector diagrams illustrating the change in momentum vectors corresponding to the image immediately above.

has begun, adding the same transverse momentum to all vectors in the same cell effectively reducing their angular difference and pushing them into a more cone-like shape. At freeze out, step *d*, flow effects have finished their work, and we can see that the cell at the larger radial position received a bigger radial momentum increase, and particles in that cell have been pushed into a narrower opening angle.

In Fig. 5.6 we show how the effects of transverse flow are represented in the measured correlation structure. Fluid cells at a larger radius emit particles in a narrower opening angle. In the cartoon on the left, we highlight in blue a pair with a small angular difference and in red a pair with larger angle. On the right, using the same colors, we identify how these two examples are represented in the measurement. We see that our argument that transverse flow enhances angular correlations, is supported by the data, at least by eye. A more quantitative comparison will come later.

To exhibit the effect of flow on particle correlations, we use the momentum-space

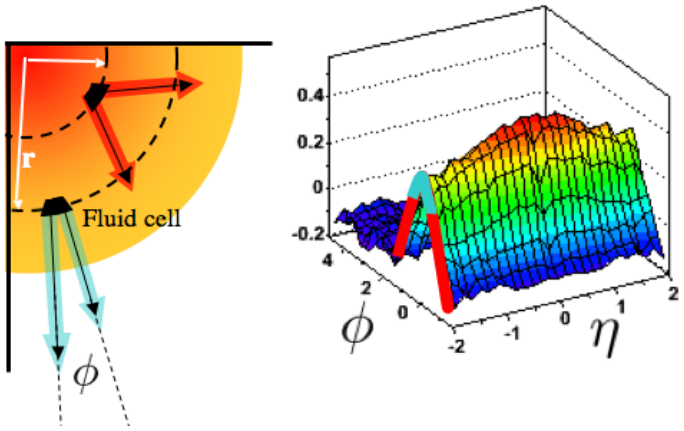


Figure 5.6: Comparison of flow effects on angular correlations to the measured correlation structure(2-D gaussian component of data in [1]). Fluid cells at larger radial position have a narrower opening angle and have a greater contribution to correlations. The wider the opening angle, the weaker the correlation.

correlation function

$$\Delta\rho(\mathbf{p}_1,\mathbf{p}_2) = \rho_2(\mathbf{p}_1,\mathbf{p}_2) - \rho_1(\mathbf{p}_1)\rho_1(\mathbf{p}_2) \tag{5.7}$$

where $\rho_2(\mathbf{p}_1,\mathbf{p}_2) = dN/dy_1 d^2p_{t1} dy_2 d^2p_{t2}$ is the pair distribution. Generalizing (3.4), we write

$$\Delta\rho(\mathbf{p}_1,\mathbf{p}_2) = \int c(\mathbf{x}_1,\mathbf{x}_2)\frac{f(\mathbf{x}_1,\mathbf{p}_1)}{n_1(\mathbf{x}_1)}\frac{f(\mathbf{x}_2,\mathbf{p}_2)}{n_1(\mathbf{x}_2)}p_1^\mu d\sigma_{\mu 1} p_2^\mu d\sigma_{\mu 2}. \tag{5.8}$$

The freeze out surface differentials follow (3.21), and the quantities $f(\mathbf{x},\mathbf{p})/n_1(\mathbf{x})$ explicitly indicate the spatial normalizations, and simply take the form of (3.23). We identify $c(\mathbf{x}_1,\mathbf{x}_2)$ at freeze out with (5.2), a form that describes the system at its formation. This identification omits the effects of diffusion described in Ch. 7 and Ref. [38, 39]. This omission is reasonable only as long as we restrict our attention to the long range correlations with pairs separated by $|\eta_1 - \eta_2| > 1$.

Starting with equation (3.23), we see that the terms including $\cosh(y-\eta)$ can factor and we can make use of (3.33) twice. We make the transformation from spatial Cartesian coordinates $\mathbf{x}_1$ and $\mathbf{x}_2$ to relative and average coordinates $\mathbf{r}_t$ and $\mathbf{R}_t$ and

write

$$\Delta\rho(\mathbf{p}_1,\mathbf{p}_2) = 4a^2\tau^2\left[m_{t1}K_1\left(\frac{\gamma_t m_{t1}}{T}\right)m_{t2}K_1\left(\frac{\gamma_t m_{t2}}{T}\right)\right] \tag{5.9}$$
$$\times\int e^{\frac{\lambda}{T}[(\mathbf{p}_{t1}+\mathbf{p}_{t2})\cdot\mathbf{R}_t+\frac{1}{2}(\mathbf{p}_{t1}+\mathbf{p}_{t2})\cdot r_t}\mathcal{R}\,\delta(\mathbf{r}_t)\rho_{_{FT}}(\mathbf{R}_t)d^2r_t d^2R_t.$$

Now we can make use of the delta function in the correlation function where integration over $d^2r_t$ eliminates the exponential with $r_t$ in the argument. The remaining exponential reduces to $exp[(\lambda/T)\|\mathbf{p}_{t1}+\mathbf{p}_{t2}\|R_t\cos\theta]$ and we can again make use of the Bessel function relation (3.34). The remaining integration looks like $\int_0^{R_A}\kappa(2\pi)I_0((\lambda/T)\|\mathbf{p}_{t1}+\mathbf{p}_{t2}\|R_t)(1-R_t^2/R_A^2)R_t dR_t$, which we can preform with help from the substitution $R_t = R_A z$ and the Bessel relation $\int\limits_0^1 z(1-z^2)I_0(\alpha z)dz = \frac{2}{\alpha^2}I_2(\alpha)$. We are now in a position to integrate over the momentum magnitudes where

$$\Delta\rho(\eta,\phi) = 16a^2\tau^2\pi R_A^2\frac{T^2}{(\lambda R_A)^2}\mathcal{R}\kappa\int\frac{m_{t1}m_{t2}}{\|\mathbf{p}_{t1}+\mathbf{p}_{t2}\|^2}K_1\left(\frac{\gamma_t m_{t1}}{T}\right)K_1\left(\frac{\gamma_t m_{t2}}{T}\right)$$

$$\times I_2\left(\frac{\lambda R_A\|\mathbf{p}_{t1}+\mathbf{p}_{t2}\|}{T}\right)p_{t1}dp_{t1}p_{t2}dp_{t2}d\Phi, \tag{5.10}$$

and $\phi = \phi_1 - \phi_2$ is the relative azimuthal angle, and $\Phi = (\phi_1+\phi_2)/2$ is the average azimuthal angle.

To confront the STAR measurements, we calculate $\Delta\rho(\eta,\phi)$ by performing the integration in (5.10) over the momenta. Similarly, we compute $\rho_{ref}(\eta,\phi)$ by integrating $\rho_1(\mathbf{p_1})\rho_1(\mathbf{p_2})$ as defined in eq,(3.38). To preform the momentum integration of Eq. (5.10), we make the same substitutions as at the end of Sec. 3.3, where $x = \gamma_t p_{t1}/T$, $y = \gamma_t p_{t2}/T$, and $\lambda R_A = \gamma_t v_s$. The pre-factor $16a^2\tau^2\pi R_A^2 v_s^{-2}(T/\gamma_t)^6\kappa$ cancels with the square of the pre-factor in eq,(3.38) and we now arrive at the result

$$\frac{\Delta\rho(\eta,\phi)}{\int\rho(p_{t1})\int\rho(p_{t2})} = \frac{\mathcal{R}\int xy\frac{\sqrt{(x^2+\zeta^2)(y^2+\zeta^2)}}{w^2}I_2(v_s w)dxdy}{\left[\int\sqrt{x^2+\zeta^2}K_1(\sqrt{x^2+\zeta^2})I_1(v_s x)dx\right]^2} = \mathcal{R}F(\phi) \qquad (5.11)$$

with $\zeta = \gamma_t m/T$, and $w = \sqrt{x^2+y^2+2xy\cos\phi}$. Notice that the blast wave normalization is not an issue, as it cancels in the ratio (5.11), which is dimensionless. Furthermore, notice that, as in Sec. 3.3, the result is independent of rapidity. This is a consequence of the lack of a spatial rapidity term in the correlation function (5.2). This is addressed further in Ch. 7.

## 5.4 Results

STAR measures the characteristics of the untagged near-side ridge as functions of the centrality at 62 and 200 GeV for Au+Au [1, 51]. While they focus on the region $-1 < \eta < 1$, where short and long range correlation phenomena are both present, it is instructive to see which aspects of the data can be explained by a purely long range model.

To facilitate our comparison, we visualize the STAR analysis as consisting of the following steps. First, a correlated two particle distribution of "sibling" particles $\rho_{sib}$ is measured. This quantity is essentially our $\rho_2$ integrated over the magnitudes of each particle's $p_t$ as well as the average azimuthal angle $\Phi = (\phi_1+\phi_2)/2$ and average pseudorapidity $\eta_a = (\eta_1+\eta_2)/2$. The resulting density depends only on the relative quantities $\phi$ and $\eta$. Then, an uncorrelated pair distribution $\rho_{ref}$ is obtained from mixed events and $\Delta\rho/\sqrt{\rho} = (\rho_{sib}-\rho_{ref})/\sqrt{\rho_{ref}}$ is constructed. Next, a rapidity-independent function $a + b\cos\phi + c\cos 2\phi$ is subtracted to remove backgrounds as well as elliptical flow and momentum conservation effects. Finally, the corrected $(\eta,\phi)$ distribution is subjected to a multicomponent fit to extract the attributes of the near side peak. In practice, these steps are performed simultaneously.

To confront the STAR measurements, we calculate $\Delta\rho(\eta,\phi)/\int\rho_1(\mathbf{p}_{t1})\int\rho_1(\mathbf{p}_{t2})$, (5.11), as described in Sec. 5.3 and multiply by the gluon distribution from (4.3), assuming the final state particle distribution scales similarly [19]. The integrations are straightforward and done numerically. We obtain

$$\frac{\Delta\rho}{\sqrt{\rho_{ref}}} = \kappa\mathcal{R}\frac{dN}{dy}F(\phi), \tag{5.12}$$

where $\int_0^{2\pi}F(\phi)d\phi = 1$ and $\kappa$ is an energy independent constant to be determined from data.

In the saturation regime, the gluon density follows (4.3), which depends on the density of gluons per flux tube $\propto\alpha_s^{-1}(Q_s)$ and the number of flux tubes $K\sim(Q_sR_A)^2$. The factor

$$\mathcal{R}\frac{dN}{dy} = \frac{1}{\alpha_s(Q_s)} \tag{5.13}$$

follows from the Glasma relations (4.3) and (5.6). Equation (5.13) contains all of the energy, system, and centrality information provided by CGC, where the angular distribution $F(\phi)$ is a result of the Glasma influence on the correlation function, but depends only on blast wave parameters $\gamma_t m/T$ and $v_s$.

We specify the centrality dependence of the correlation function using the velocity and temperature fit from single particle spectra at 200 GeV in Ref. [27]. The computed $F(\phi)$, ($\Delta\rho/\sqrt{\rho}$ without the CGC scaling) is shown as the dashed line in the top right panel of Fig. 5.7. We fix $\kappa$ in (5.12) such that the calculation of the most central point of $F(\phi)$ agrees with that of the 200 GeV data (only). The top left panel shows the same calculation using the same value of $\kappa$ with a constant temperature of 120 $MeV$. The solid lines represent the full equation (5.12), this time including the CGC scaling relation.

We define the height of the near side peak as the difference between $\Delta\rho/\sqrt{\rho}$ at $\phi = 0$ and $\pi$. It follows the basic trend of the data rather well, given that the only

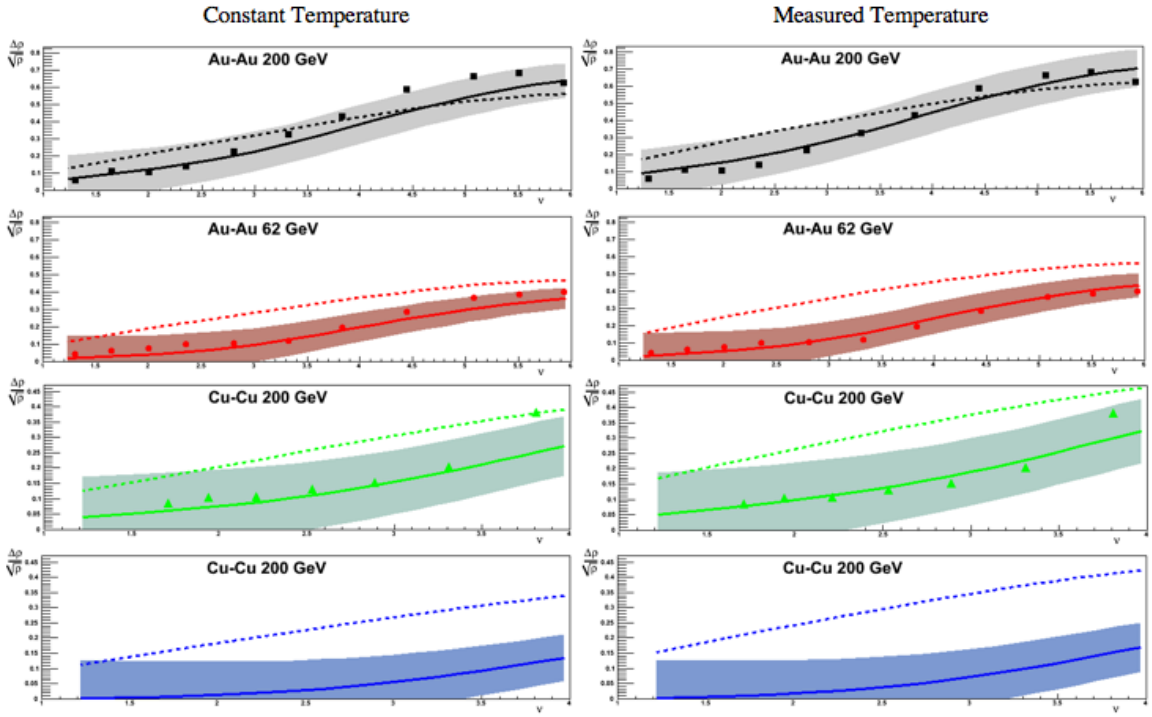


Figure 5.7: $\Delta\rho/\sqrt{\rho}$ amplitudes for Au+Au and Cu+Cu 200 and 62 GeV. All data point are preliminary STAR data, Au+Au from [1] and Cu+Cu from [26]. The normalization parameter $\kappa$ is adjusted *only* in the case of Au+Au 200 GeV with blast wave temperature from [27]. Calculations presented in the left column use a constant temperature of 120 MeV and the right column uses a centrality dependent temperature measured by experiment.

parameters that vary with centrality – $v$ and $T$ – are fit elsewhere [27]. The shaded bands in Fig. 5.7 represent the uncertainty in $v$ and $T$ combined with an uncertainty in the parameterization of $Q_s^2$, which increases inversely with centrality.

To compute $\Delta\rho/\sqrt{\rho}$ at 62 GeV, we follow [27] and reduce the velocities by 5% and the temperatures by 10% by uniform scale factors. The dashed curves again represent the calculation $F(\phi)$ alone and are well above the data, but agrees roughly in shape. Note, we now take the factor $\kappa$ as fixed, and no longer adjust it. The solid curve again represents the inclusion of the CGC scaling (5.13). We reduce $Q_s$ by $\sim 1/2$ to change from 200 GeV to 62 GeV, and we see surprisingly good agreement with the data.

We see that although blast wave parameters have some energy dependence, the Glasma factor (5.13) allows for strong agreement with the 62 GeV data without further adjustment of $\kappa$. In this manner, we use (5.13) to predict the amplitude of the near side peak of the soft ridge in Cu+Cu for both 200 and 62 GeV as a function of centrality. We are able to do this, again without adjustment of $\kappa$, because of the $Q_s^2$ dependence on the density of participants. We simply scale $Q_s^2$ by the ratio of the cental participant density in Au+Au to that of Cu+Cu

$$Q^2_{s,CuCu} = Q^2_{s,AuAu}\frac{\rho_{part,CuCu\ central}}{\rho_{part,AuAu\ central}}. \tag{5.14}$$

Caution should be taken however, since we use the centrality dependance of the blast wave parameters $T$ and $v_s$ as well as the saturation scale from Au+Au in the Cu+Cu calculation. The results are shown in Fig. 5.7 and again give nice agreement.

To compare to measured azimuthal widths, we plot (5.12) as a function of $\phi$ and simulate the experimental fit procedure, obtaining the width in the near-side interval $-\pi/2 < \phi < \pi/2$ by fitting a gaussian plus a constant offset. The results are shown in Fig. 5.8 for both Au+Au and Cu+Cu. We find that the width is nearly independent

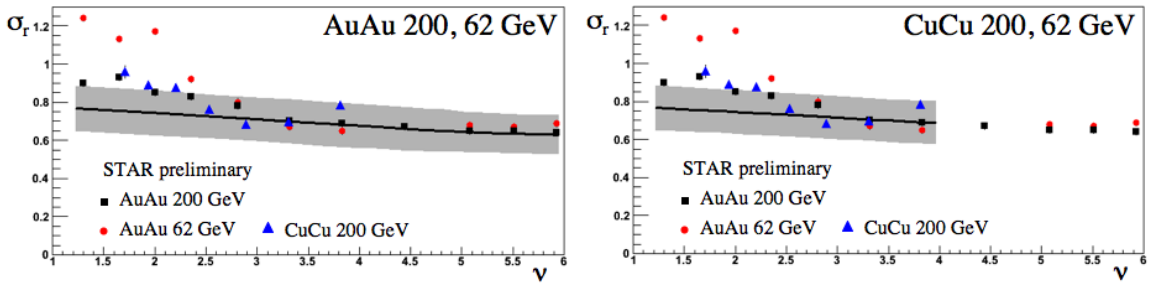


Figure 5.8: Azimuthal correlation widths for Au+Au (left) and Cu+Cu (right) for 200 and 62 GeV. Error bands represent uncertainty in a gaussian fit to calculated azimuthal distributions.

of both system and energy since the blast wave parameters change very little, and the normalization does not affect $F(\phi)$. The uncertainty band in Fig. 5.8 indicates the impact of changing the near-side interval by $\pm 20\%$, i.e. the error associated with the fit. Once again, the agreement is surprisingly good given the simplicity of the model. Note that Ref. [25] includes flow by boosting a Glasma source. Their computed width exceeds data because they omit the $p_t$ dependence of the boost and do not simulate the experimental fit procedure.

To recap the chapter, we describe how the near side peak of the soft ridge can be explained by Glasma flux tube initial conditions and transverse flow. Glasma conditions allow for the existence of correlations between causally separated pairs while transverse flow preserve these long range correlations and enhance angular correlations. The case for Glasma initial conditions is strengthened by the fact that it provides energy and system dependence in addition to centrality dependence, which allow for parameter free deduction of 62 GeV data and prediction of Cu+Cu data.

# Chapter 6

## Hard Ridge / One Ridge

A primary focus of this work is to determine if the soft and hard ridges are fundamentally different phenomena. Although the hard ridge attempts to isolate the effects of jets on the medium, both ridges are di-hadron correlation measurements with similar *looking* structures. Comparing Fig.6.1 to Fig.5.1 some differences one might notice include the fact that the azimuthal width of the hard ridge is narrower than that of the soft ridge, and that although the relative rapidity width is still broad, the hard ridge seems to have a separate narrower peak sitting on it. Since the rapidity width of the narrower peak is similar to the width measured with PYTHIA simulations, we hypothesize that it is a result of correlations from jet fragmentation, although we don't address that here, see Sec. 8.1. Our interest here centers on the broad ridge structure, its connection to the soft ridge, and its relationship to long range correlations.

To understand the relationship between the soft and hard ridge, we must account for the the differences in the two measurements, and determine how to compare them. The hard ridge measures the yield of associated particles per jet trigger, and the soft ridge reports the number of "sibling" pairs per reference multiplicity. Sibling pairs are pairs from the same event and the reference is the square root of the uncorrelated pair distribution. The most significant difference between the two measurements is the choice of the momentum range of the correlated particles. The hard ridge attempts to

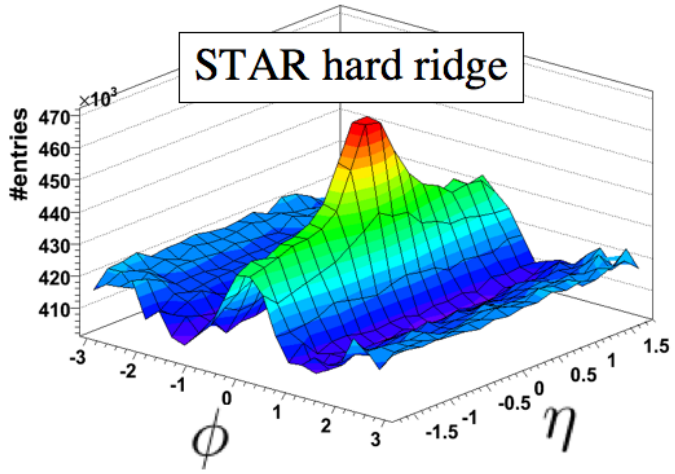


Figure 6.1: STAR hard ridge, Au+Au, 200 GeV, $0-10\%$ central [3]. The "*#entries*" on the vertical axis represents the yield of correlated pairs per jet trigger, with the trigger in the range $3 < p_{t,trigg} < 4$ GeV and paired with a particle in the associated range $2 < p_{t,assoc} < 3$

highlight the influence of jets and arises from particle pairs where one particle comes from a jet trigger $p_t$ range and the other comes from a lower associated $p_t$ range. Conversely, the soft ridge represents all correlated pairs taking both particles from any $p_t$ above minimum bias. In Sec.6.1 we describe the behavior of the soft ridge with a change in the $p_t$ range of particle pairs, and describe how to compare the observable with that of the hard ridge. In Sec.6.2, we describe one method by which jets could contribute to long range correlations, and in Sec.6.3 and Sec.6.4 we describe how soft ridge effects combine with those jet-bulk correlations to explain some features of the hard ridge.

## 6.1 Soft Contribution to the Hard Ridge

We observe that both the hard ridge amplitude and azimuthal width are smaller than that of the soft ridge. Since the angular width of the soft ridge depends on small thermal fluids cell receiving a radial boost, the higher $p_t$ particles are those that received the greater push from flow. As described before, the greater the radial boost given to a fluid cell, the narrower the relative angle between the momentum

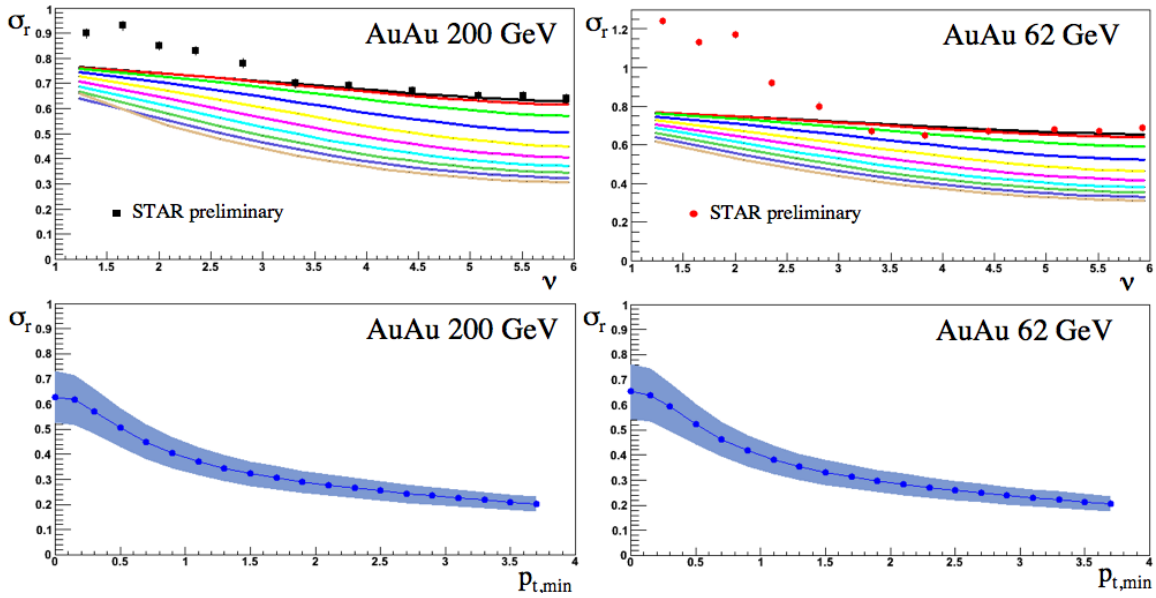


Figure 6.2: (top) Azimuthal width of the near side peak for Au+Au 200 GeV vs. centrality. Colored lines (from top to bottom) represent increasing $p_{t,min}$ limits. (bottom) Plots the most central values of the width vs $p_{t,min}$. Each dot represents the central point of a curve in the graph above.

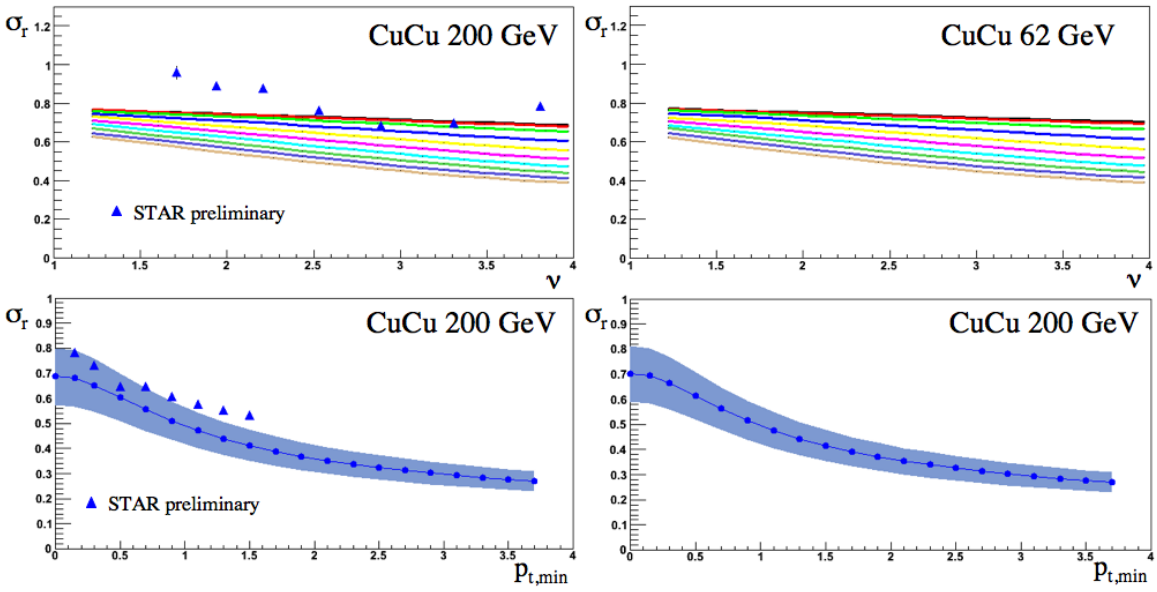


Figure 6.3: (top) Azimuthal width of the near side peak for Cu+Cu 200 GeV vs. centrality. Colored lines (from top to bottom) represent increasing $p_{t,min}$ limits. (bottom) Plots the most central values of the width vs $p_{t,min}$. Each dot represents the central point of a curve in the graph above.

vectors of particles in that cell. We therefore expect that the azimuthal width of the soft ridge will narrow if the $p_t$ range of correlated particles is increased. Furthermore, if we "cut out" lower $p_t$ particles, we reduce the number of possible pairs and therefore reduce the ridge amplitude as well.

To examine the $p_t$ dependence of the soft ridge, we rewrite (5.11) such that the lower limit of the $p_t$ integration is no longer zero but some minimum value $p_{t,min}$

$$\left(\frac{\Delta\rho}{\rho_{ref}}\right)_{p_{t,min}} = \frac{\int_{p_{t2,min}}^{p_{t2,max}}\int_{p_{t1,min}}^{p_{t1,max}} \Delta\rho(\mathbf{p}_1,\mathbf{p}_2)}{\int_{p_{t1,\min}}^{p_{t1,max}} \rho_1(p_{t1}) \int_{p_{t2,min}}^{p_{t2,max}} \rho_1(p_{t2})}$$

$$= \mathcal{R}F(\phi; p_{t1,min}, p_{t1,max}, p_{t2,min}, p_{t2,max}). \tag{6.1}$$

To obtain the measured ratio, we write

$$\frac{(\Delta\rho/\sqrt{\rho_{ref}})_{p_{t,min}}}{\Delta\rho/\sqrt{\rho_{ref}}} = \frac{F(\phi; p_{t,min}, \infty, p_{t,min}, \infty)}{F(\phi)} \frac{\int_{p_{t1,min}}^{\infty}\rho_1}{\int_0^{\infty}\rho_1}. \tag{6.2}$$

For increasing values of $p_{t,min}$, we calculate the correlation function as in chapter 5, using (6.1) and (6.2) and find that the azimuthal width does indeed decrease as shown in the upper panels of Fig.6.2, and Fig.6.3. The black curves are the same curves shown in Fig.5.8, (i.e. $p_{t,min} = 0$), and the following colored curves represent, in descending order, the width calculation for $p_{t,min} = \{0.15, 0.3, 0.5, 0.7, ...\}$ GeV also indicated by the dots in the panel directly below. The lower panels plot the most central width value for each curve as a function of its $p_{t,min}$ limit. Preliminary data in Fig.6.3 comes from ref.[26] and shows decent agreement. We remark that if one examines the Cu+Cu most central width in Fig.5.8 one might notice that it is slightly greater than both the Au+Au data and our calculations. This difference may be the reason why our curve in the lower right panel of Fig.6.3 is consistently lower than the

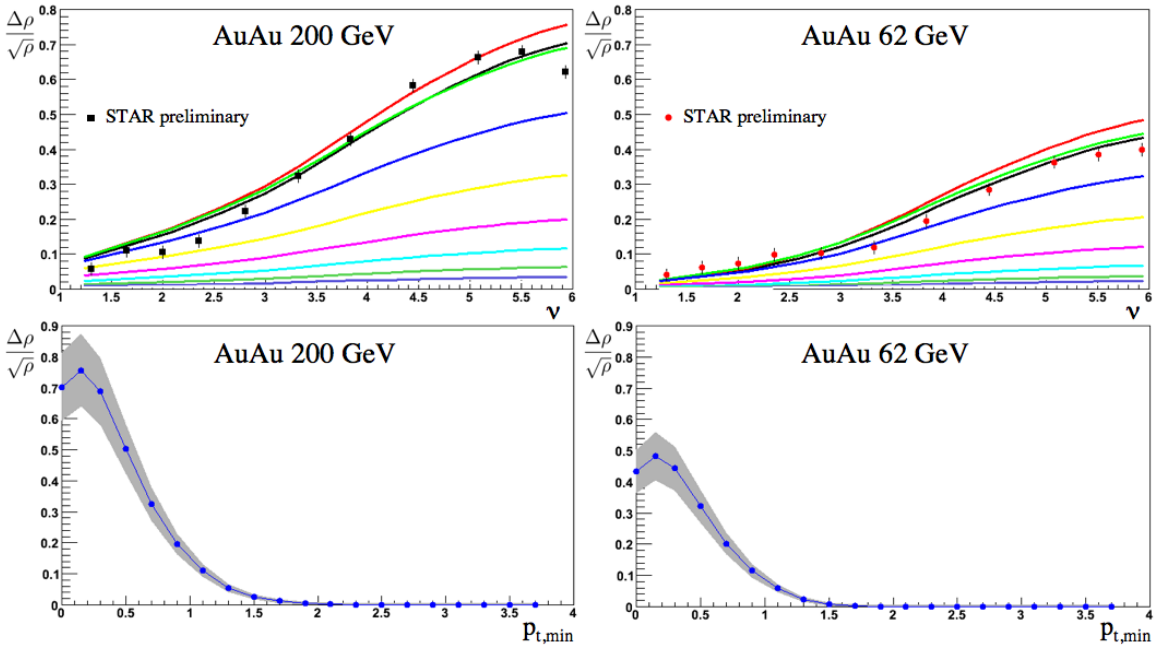


Figure 6.4: Soft ridge near side peak amplitudes for Au+Au 200 and 62 GeV. Top panels: amplitudes vs. centrality for various $p_{t,min}$ limits as indicated by the dots in the lower panels. Lower panels: most central point of the curves directly above vs the $p_{t,min}$ limit.

data.

The upper panels of Fig.6.4 and Fig.6.5 show predictions of the amplitude $\Delta\rho/\sqrt{\rho_{ref}}$ vs. centrality for the same choices of $p_{t,min}$ as previously discussed. The amplitude decreases with increasing $p_{t,min}$ because the number of particles contributing to correlations is reduced. The lower panels of Fig.6.4 and Fig.6.5 show the amplitudes for the most central collision as a function of the choice of $p_{t,min}$. Preliminary STAR data, shown in the lower left panel of Fig.6.5, shows agreement, at the very least, with the trend of our predictions. Again, we must take caution since we use the Au+Au centrality dependance of the blast wave as well as the saturation scale parameterizations; the large error bars in our Cu+Cu calculations are representative of this.

As the minimum $p_t$ of the particles is increased, the amplitude of the correlations drops and the azimuthal width narrows. In the $p_t$ range of the hard ridge, it appears

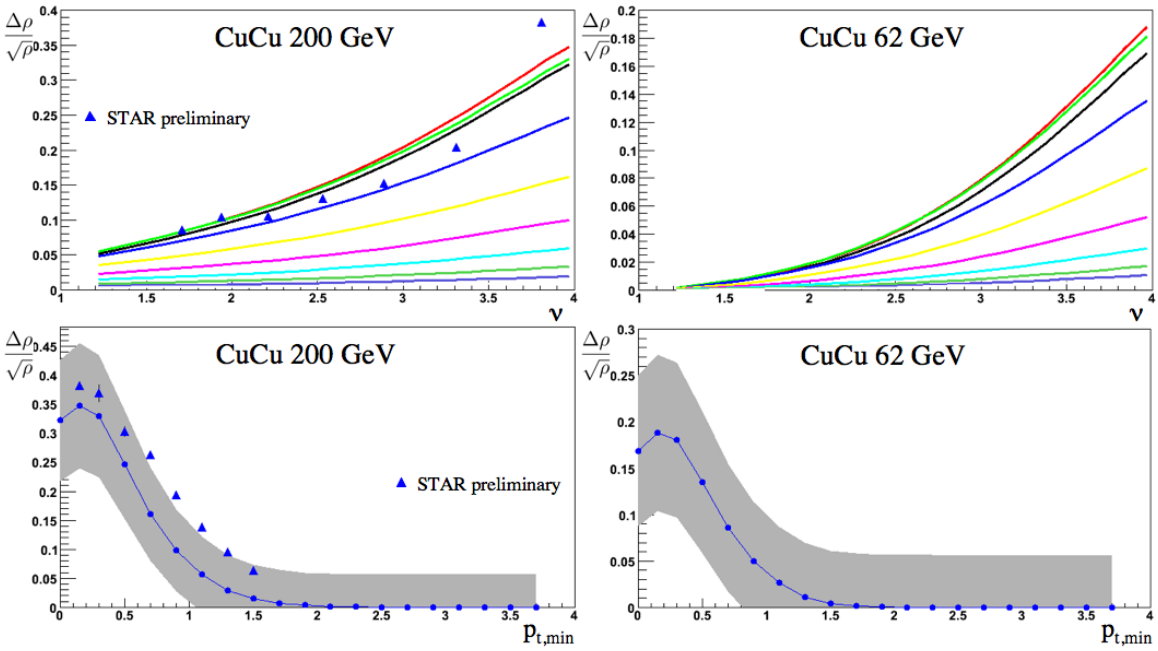


Figure 6.5: Soft ridge near side peak amplitudes for Cu+Cu 200 and 62 GeV. Top panels: amplitudes vs. centrality for various $p_{t,min}$ limits as indicated by the dots in the lower panels. Lower panels: most central point of the curves directly above vs the $p_{t,min}$ limit.

that the azimuthal width could be narrow enough, but the amplitude is not a directly comparable quantity. STAR measures the hard ridge, or yield of associated particles per jet trigger, for Au+Au 200 GeV for $3 < p_{t,trigg} < 4$ GeV with $2 < p_{t,assoc} < 3$ [3]. We identify $p_{t1}$ in our calculation with the trigger range, $p_{t2}$ with the associated range, and calculate $\Delta\rho/\sqrt{\rho_{ref}}$. We find the yield with the transformation

$$\text{Yield} = \left(\frac{\Delta\rho}{\sqrt{\rho_{ref}}}\right)_{p_{t,min}} \left(\frac{\int \rho_1(p_{t2})}{\sqrt{\int \rho_1(p_{t1}) \int \rho_1(p_{t2})}}\right). \tag{6.3}$$

At higher ranges of $p_{t1,2}$ the contribution from jets should become more significant, and it is important, therefore, to know the relative fraction of thermal and jet contributions. Section 6.3 discusses how we decompose the total particle spectrum into thermal bulk and jet fractions. To obtain the contribution of bulk correlations to the hard ridge, we multiply (6.3) by the bulk fraction $\int \rho_1(p_{t1}) / \int \rho_{tot}(p_{t1})$ where

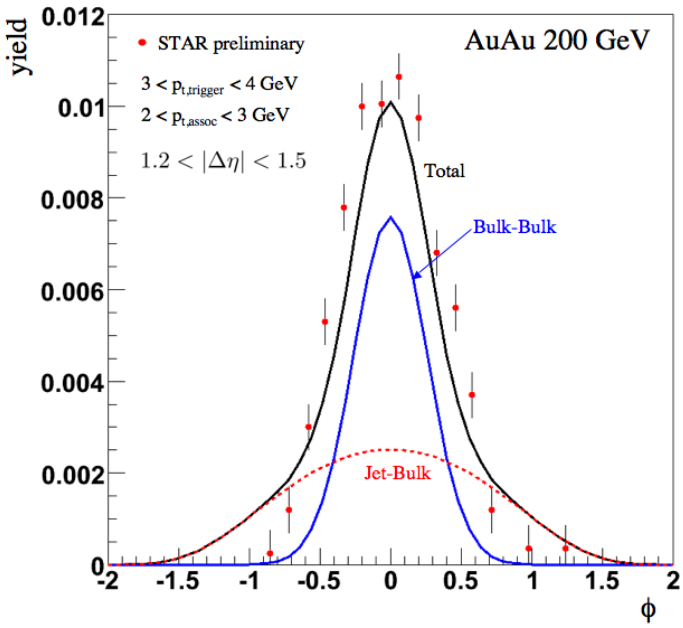


Figure 6.6: Comparison of bulk-bulk and jet-bulk correlation yields to a cross section of the hard ridge. Jet contributions begin at $p_s$=1.25 GeV. Data from [3] (talk).

$\int \rho_{tot}(p_{t1})$ is the total number of particles in the range of $p_{t1}$.

We find from this calculation, that the contribution to the hard ridge from only thermal bulk pairs is $\sim 75\%$, a considerable fraction. The blue curve in Fig.6.6 represents the contribution to the hard ridge from only thermal bulk pairs. We see from the the blue curve in Fig.6.6 that "bulk-bulk" correlations contribute significantly to the amplitude of the triggered measurement, but has a somewhat narrower azimuthal profile. Ref.[79] shows that a jet acquires angular correlations with flowing matter due to quenching, but the width of the correlation is wider than the data. The contribution of jet correlations with bulk particles, "jet-bulk" correlations, could increase both the amplitude and the width and make up the difference between the bulk-bulk correlations and data.

In the next section we combine a theory of angular correlations from Ref.[79] with spatial correlations of jets and flux tubes to obtain a jet-bulk contribution to the hard ridge.

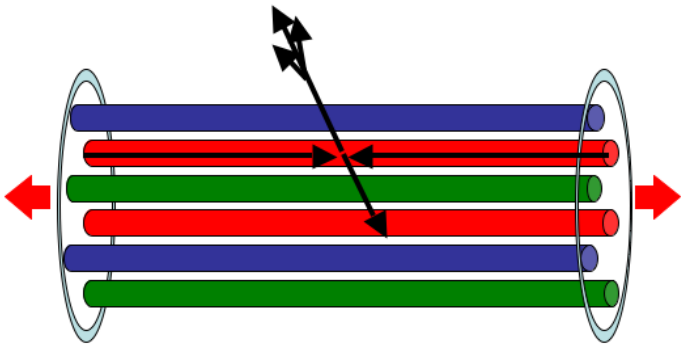

Figure 6.7: Jet correlations with tubes. Anywhere in the overlap region, the location of a hard collision will coincide with a flux tube, since tubes fill the space.

## 6.2 Jet Quenching, Flow, and Correlations

The existence of correlations with jet particles at larger $\eta$ would require a correlation early in the collision that remains through the expansion of the system. As we examine higher $p_t$ pair correlations, the contributions from jets should become more prevalent, particularly for small $\eta$. Correlations between jet fragments should eventually dominate the correlation structure, but are restricted to the size of the jet cone, and the transfer of momentum from jets to bulk particles is causally limited to $\sim 1-2$ units in rapidity.

Both the hard collisions and flux tubes are made in the initial moments of the nuclear collision. Assuming that the entire overlap region of the colliding nuclei is in the saturation regime, flux tubes would fill the collision volume and a jet formed at any transverse position would be accompanied by a flux tube at the same position. Since the flux tube extends to large rapidities, the correlation of particles from a flux tube and a jet can extend to large $\eta$. Angular correlations arise since particles from the tube acquire a radial trajectory from flow, but the (measured) jet trajectory has a bias in the radial direction due to quenching [79].

For the purposes of simplicity, we start with the assumption that jet production is independent and uncorrelated with the production of soft particles. It has been

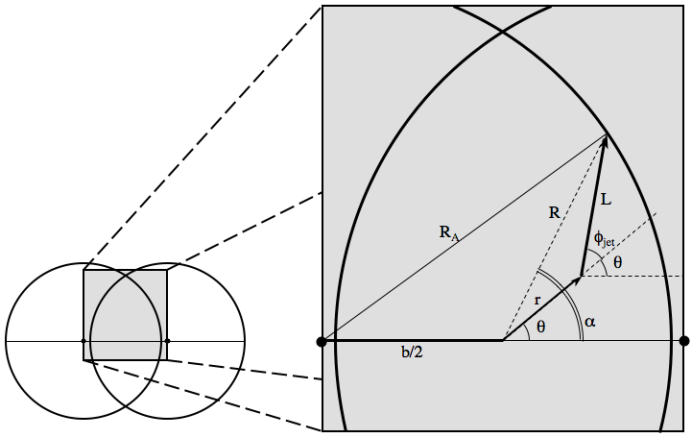


Figure 6.8: Jet path, **L**, with relation to the event plane.

pointed out in Refs.[60, 79] that some information about the location of a hard collision can be determined by correlating it with transverse flow. Since the jet must pass through matter, there is some chance that the matter attenuates or even completely absorbs the jet. Since the amount of this quenching is related to the amount of matter the jet must pass through, surviving jets tend to be biased toward the surface of the medium. Furthermore, if the jet production point is deeper into the medium, the jet must take the most direct exit route to have the greatest chance to survive; if the medium is circular, the most direct route is a radial one.

Since quenching biases jets to have a more radial direction, and transverse flow pushes bulk particles to a more radial trajectory, an angular correlation is induced between the jet and bulk particles originating at the same radial position. Reference [79] considers correlations of jets with beam jets, but we explore the possibility of jet correlation with flux tubes. As illustrated in Fig.6.7, since flux tubes fill the transverse space of the overlap region, any transverse location that a hard collision occurs would coincide with a flux tube independently produced at the same location. As a caveat, at RHIC energies, saturation does not extend to the periphery of the nuclei so a correction including a "core" made of flux tubes and a "corona" with Glauber-like production would be appropriate.

At the moment of a hard collision, the jet direction is random, and the amount of quenching, or conversely, the chance of survival, depends on the path, **L**, through the matter, as depicted in Fig.6.8 and Fig.6.9. Assuming the nuclei are hard spheres, and that the jet exits the medium before significant expansion, from geometrical considerations we find the jet path to be

$$\begin{aligned} L &= -\frac{1}{2}\left[2r\cos\phi_{jet} \pm b\cos(\phi_{jet}+\theta)\right] \\ &\quad +\frac{1}{2}\sqrt{\left[2r\cos\phi_{jet} \pm b\cos(\phi_{jet}+\theta)\right]^2 - 4\left[r^2 - R_A^2 + b^2/4 \pm br\cos\theta\right]}. \end{aligned} \tag{6.4}$$

Notice that the quenching length is sensitive to the reaction plane. We must take care since the vector **r** can, for example, point to the $+x$ side of the $xy$-plane and the vector **L** can point to the $-x$ side. Equation (6.4) has two solutions depending on which hemisphere the vector **R** points, since this is the hemisphere the jet exits. In (6.4), we choose the positive solution for $-\pi/2 < \alpha < \pi/2$ and negative for $\pi/2 < \alpha < 3\pi/2$ where $\alpha = \sin^{-1}[(L/R)\sin\phi_{jet}]+\theta$ and $R = \sqrt{r^2 + L^2 + 2rL\cos\phi_{jet}}$. For the symmetric case, if $b = 0$ then (6.4) reduces to

$$L = \sqrt{R_A^2 - r^2\sin^2\phi_{jet}} - r\cos\phi_{jet}, \tag{6.5}$$

a result stated in Ref.[79]. For the purposes of the following calculation, we make the approximation that the collision transverse area is circular, even for peripheral collisions. In the future, we plan to study the reaction plane dependence of the ridge, which would require us to abandon this assumption as well as introduce eccentricities back into the blast wave formulation as discussed in Ch.3.

For now, let us analyze the contributions of jet-bulk correlations in the case of circularly symmetric initial systems as illustrated in Fig.6.9. If **r** is small (close to

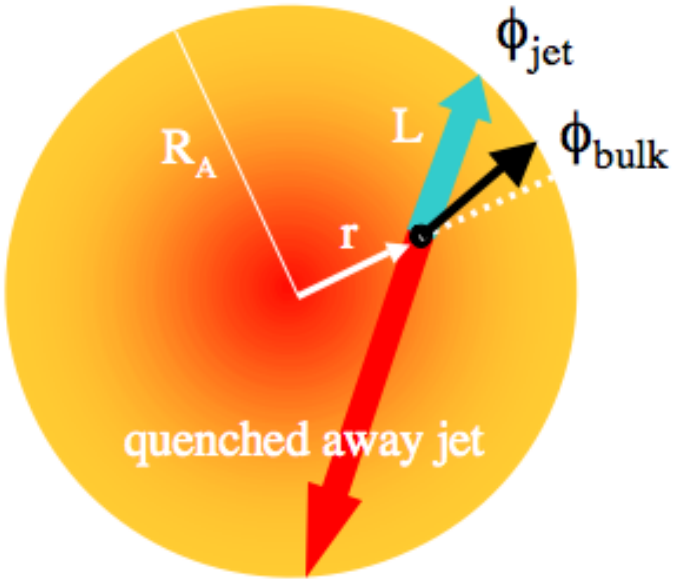


Figure 6.9: Jet path, **L**, in a circularly symmetric system, compared to a particle which will later have a radial trajectory from flow.

the center), the probability of having a jet is maximum, but then **L** is the same in all directions, providing no correlation. If **r** is close to the surface, the probability of production is at a minimum, and the jet, with any trajectory pointing away from the medium, experiences little or no quenching. In this case, there is some correlation since some of the jet's trajectories are restricted. At some depth inside, the probability of jet production increases, and the range of $\phi_{jet}$ of surviving jets is narrowed. To determine the angular shape and magnitude of this phenomenon, we modify our calculation in Ch. 5 by replacing the blast wave distribution $f(\mathbf{x}_1, \mathbf{p}_1)/n(\mathbf{x}_1)$ in (5.8) with the jet distribution $f_{jet}(\mathbf{x}_1, \mathbf{p}_1)/n(\mathbf{x}_1)$.

We define the jet distribution as

$$f_{jet}(\mathbf{x}, \mathbf{p}) = \frac{A}{p_t^n} P_{prod}(r_{jet}) S(r_{jet}, \phi_{jet}). \tag{6.6}$$

The probability of jet production is

$$P_{prod}(r_{jet}) \propto \left(1 - \frac{r_{jet}^2}{R^2}\right), \tag{6.7}$$

for two homogenous hard spheres colliding centrally. For future calculations that include the anisotropy of the system, we would need to explicitly use a Glauber calculation of binary collisions [87]. The probability of quenching, or the probability the jet survives, is approximated by an exponential damping

$$S(r_{jet}, \phi_{jet}) = e^{\frac{-L(r_{jet},\phi_{jet})}{\ell_{abs}}} \tag{6.8}$$

that depends on the jet path (6.5) and the quenching length $\ell_{abs} = 0.25fm$ [79]. The momentum distribution follows a power law of the form $A/p^n$.

We rewrite (5.8) using the indicies "$_J$" for "jet" and "$_B$" for "bulk", such that the first particle comes from a jet and the second from a flux tube

$$\Delta\rho_{_{JB}}(\mathbf{p}_1, \mathbf{p}_2) = \int c_{_{JB}}(\mathbf{x}_1, \mathbf{x}_2) \frac{f_{_J}(\mathbf{x}_1, \mathbf{p}_1)}{n_1(\mathbf{x}_1)} \frac{f_{_B}(\mathbf{x}_2, \mathbf{p}_2)}{n_1(\mathbf{x}_2)} p_1^\mu d\sigma_{\mu 1} p_2^\mu d\sigma_{\mu 2} \tag{6.9}$$

where $p^\mu d\sigma_\mu$ follows (3.21). The correlation function $c_{_{JB}}(\mathbf{x}_1, \mathbf{x}_2)$ requires that a jet and a bulk particle must come from the same radial position. The rest of the equation accounts for the different spectra for jet and bulk particles. We write

$$c_{_{JB}}(\mathbf{x}_1, \mathbf{x}_2) = \frac{\mathcal{R}_{_{JB}} \langle N_J \rangle}{\mathcal{R} \langle N_B \rangle} c(\mathbf{x}_1, \mathbf{x}_2), \tag{6.10}$$

where $c$ is given by (5.2) and $\kappa_{_{JB}} = 2\langle N_{_J} \rangle \langle N_{_B} \rangle / (\pi R_A^2 (\Delta y)^2 \tau^2)$.

To relate the correlation strength $\mathcal{R}_{_{JB}}$ to the bulk correlation strength $\mathcal{R}$ discussed earlier, we assume that the hard scattering rate is independent of the flux tube dynamics. Recall that the bulk quantity $\mathcal{R}$ in (5.4) is related to the number of

flux tubes; see (5.13). If we take the fraction of jet and bulk particles per flux tube to be independent of the number of flux tubes, we can write $\langle N_{_J}\rangle = \alpha\langle N\rangle$, where $\alpha$ and $\beta$ may depend on momentum, but do not vary event by event. We then follow Ref. [152] to find $\langle N_{_B}\rangle = \beta\langle N\rangle$, and $\langle N_{_J}N_{_B}\rangle = \alpha\beta\langle N(N-1)\rangle$, so that

$$\begin{aligned}\mathcal{R}_{_{JB}} &= \frac{\langle N_{_J}N_{_B}\rangle - \langle N_{_J}\rangle\langle N_{_B}\rangle}{\langle N_{_J}\rangle\langle N_{_B}\rangle} \\ &= \frac{\alpha\beta\langle N(N-1)\rangle - \alpha\langle N\rangle\beta\langle N\rangle}{\alpha\langle N\rangle\beta\langle N\rangle} \\ &= \frac{\langle N(N-1)\rangle - \langle N\rangle^2}{\langle N\rangle^2} \;=\; \mathcal{R}. \end{aligned} \tag{6.11}$$

Therefore, the addition of jets to the total multiplicity doesn't change the correlation strength. In essence, the beam jet associated with the hard process is just another flux tube in the high density Glasma state.

Our objective, as before, is to compute $\Delta\rho_{_{JB}}(\eta,\phi) = \int \Delta\rho_{_{JB}}(\mathbf{p}_1,\mathbf{p}_2)p_{t1}p_{t2}dp_{t1}dp_{t2}d\Phi$. To simplify, we notice that the terms containing the jet momentum, $p_{t1}$, and the jet rapidity, $y_1$, (and spatial rapidity, $\eta_1$) can factor out of (6.9) such that we can write

$$A_{p_{t1}} = \int \frac{Am_{t1}}{p_{t1}^n} p_{t1}dp_{t1} \tag{6.12}$$

$$A_{\eta_1} = \int \cosh(y_1-\eta_1)d\eta_1. \tag{6.13}$$

Moreover, we can make use of (3.33) yet again to preform the integration of $\eta_2$. The

jet-bulk correlation function in now

$$\Delta\rho_{_{JB}}(\eta,\phi) = 2a\tau^2\kappa_{_{JB}}\mathcal{R}A_{p_{t1}}A_{\eta_1}\int\int e^{\frac{-L(r_{jet},\phi_{jet})}{\ell_{abs}}}e^{\frac{\lambda r_2 p_2\cos(\phi_2)}{T}}$$

$$\times m_{t2}K_1\left(\frac{\gamma_t m_{t2}}{T}\right)\delta(r)\left(1-\frac{R_t^2}{R_A^2}\right)d^2r_1d^2r_2p_{t2}dp_{t2}d\Phi. \tag{6.14}$$

We now exploit the delta function and integrate over either of the remaining spatial variables (let's pick $r_2$). In effect, this only changes the subscript of the radial variables. To avoid confusion, let us immediately make the substitution $r_1 = x_r R_A$. Finally, the last analytical integration we perform yields $\int d\theta_1 = 2\pi$. We make more substitutions as done before in Sec. 3.3 and 5.3, where $x = \gamma_t p_{t1}/T$, and $\gamma_t v_s = \lambda R_A$ so that we have

$$\begin{aligned}\Delta\rho_{_{JB}}(\eta,\phi) &= 4\pi R_A^2 a\tau^2\kappa_{_{JB}}\mathcal{R}\left(\frac{T}{\gamma_r}\right)^3 A_{p_{t1}}A_{\eta_1}\\ &\times\int_0^{2\pi}\int_{\frac{\gamma_t}{T}p_{t1,min}}^{\infty}\int_0^1 S(x_rR_A,\Phi+\frac{\phi}{2})(1-x_r^2)^2\\ &\times\sqrt{x^2+\zeta^2}K_1(\sqrt{x^2+\zeta^2})\\ &\times e^{v_s x_r x\cos(\Phi+\phi/2)}x_r x dx_r dx d\Phi,\end{aligned} \tag{6.15}$$

with $\zeta = \gamma_t m/T$.

To determine $\rho_{ref}$, we equate $\rho_{ref} = \int\rho_{1,jet}(\mathbf{p}_1)\int\rho_{1,bulk}(\mathbf{p}_2)$. Using (6.6), (6.13), and (6.13) we find

$$\int\rho_{1,jet}(\mathbf{p}_1) = \frac{1}{\pi R_A^2}\frac{dN_{jet}}{dy}A_{p_{t1}}A_{\eta_1}\int_0^{2\pi}\int_0^1 2\pi R_A^2(1-x_r^2)S(x_rR_A,\phi_1)x_r dx_r d\phi_1. \tag{6.16}$$

We leave the factor of $2\pi R_A^2$ in the integrand to indicate it is the result of the spatial integration $\int d\theta_1 = 2\pi$, and the spatial substitution $r_1 = x_r R_A$.

$$\frac{\Delta\rho_{JB}(\eta,\phi)}{\int \rho_{1,jet}(\mathbf{p}_1)\int \rho_{1,bulk}(\mathbf{p}_2)} =$$

$$\mathcal{R}v_s \frac{\int_0^{2\pi}\int_{x_{min}}^{x_{max}}\int_0^1 S(x_r R_A,\phi_1)(1-x_r^2)^2 m_{t,x}K_1(m_{t,x})e^{v_s x_r x\cos(\phi_1)}x_r x dx_r dx d\Phi}{\left[\int_0^{2\pi}\int_0^1 (1-x_r^2)S(x_r R_A,\phi_1)x_r dx_r d\phi_1\right]\left[\int_{x_{min}}^{x_{max}} m_{t,x}K_1(m_{t,x})I_1(v_s x)dx\right]} \tag{6.17}$$

where $m_{t,x} = \sqrt{x^2 + (\gamma_t m/T)}$ and $\phi_1 = \Phi + \phi/2$ and $x_{min,max} = \gamma_t p_{t2,min,max}/T$.

We can now write (6.17) as $\Delta\rho/\rho_{ref} = \mathcal{R}F_{JB}(\phi)$ and similarly to (5.12) we have for jet-bulk correlations

$$\frac{\Delta\rho_{JB}}{\sqrt{\rho_{ref}}} = \kappa\mathcal{R}\frac{dN_{jet}}{dy}F_{JB}(\phi). \tag{6.18}$$

Here $\kappa$ is the *same* as in (5.12), and we find the jet distribution with

$$\mathcal{R}\frac{dN_{jet}}{dy} = \mathcal{R}\frac{dN_{bulk}}{dy}\frac{\int \rho_{1,jet}(\mathbf{p}_{t1})}{\int \rho_{1,bulk}(\mathbf{p}_{t1})}, \tag{6.19}$$

where $p_{t1}$ is in the jet range and

$$\int \rho_{1,jet}(\mathbf{p}_{t1}) = \int \rho_{tot}(\mathbf{p}_{t1}) - \int \rho_{1,bulk}(\mathbf{p}_{t1}). \tag{6.20}$$

Multiplying (6.18) by the jet fraction, $\int \rho_{1,jet}(p_{t1})/\int \rho_{tot}(p_{t1})$, and using (6.3) to change from $\Delta\rho/\sqrt{\rho}$ to yield, we find the jet-bulk correlation yield. To match the hard ridge measurement, we take appropriate $p_t$ limits and find the red curve in Fig.6.1. We see that the jet-bulk correlation distribution is wider than the data, but makes up only $\sim 25\%$ of the amplitude. Reference [79] also finds that the calculated width is too wide, but does not calculate the amplitude. In the following sections, we show

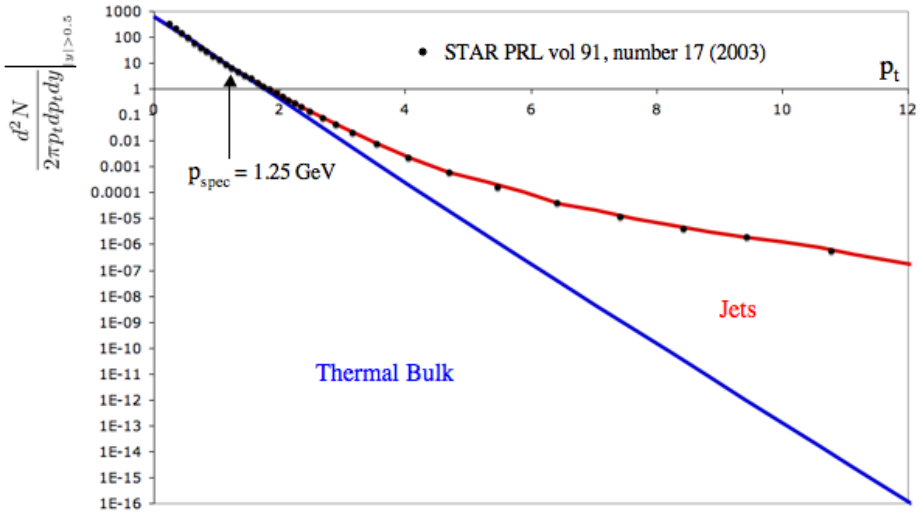


Figure 6.10: Blast wave vs jet fraction of the invariant spectrum. The blue exponential line represents the blast wave calculation with its magnitude scaled to intersect the measured spectrum at $p_s = 1.25$ GeV. The area below the exponential represents the number of thermal particles and we take the remainder to represent the number of jets.

that in adding the bulk-bulk and jet-bulk correlations, we can describe the amplitude and azimuthal width of the hard ridge quite well.

## 6.3 Bulk and Jet Fractions

In order to compute the amplitude and azimuthal width of the hard ridge in Fig.6.6, we must determine the relative contributions from both bulk-bulk and jet-bulk correlations. The measured $p_t$ spectrum follows an exponential behavior at low $p_t$ and a power law behavior at higher $p_t$ where jets play a larger role, see e.g. Ref. [52]. Our blast wave formulation describes the exponential behavior of the low $p_t$ spectrum well. The scale $p_s$ at which the spectrum begins to deviate from exponential behavior is proportional to $Q_s$ in Glasma theory, but the proportionality constant is not known. This introduces a free parameter – $p_s$ at $\sqrt{s} = 200$ GeV – that we fix below. We then find the number of jet particles by taking the difference between the total number of particles and the number of thermal particles $\rho_{1,J} = \rho_{1,tot} - \rho_{1,B}$. We take $\rho_{1,tot}$ from

the measured spectrum in Ref. [52] and $\rho_{1,B}$ from the blast wave calculation with the appropriate normalization.

If we decrease $p_s$, we effectively increase the number of jets and decrease the number of bulk particles. The resulting increase in jet-bulk correlations is less then the decrease in bulk-bulk correlations, and the total amplitude is less than the data. Conversely, if we increase $p_s$, the bulk-bulk amplitude growth is much larger than the jet-bulk reduction, and the total amplitude is then greater than the data. Even though we have introduced a free parameter into our calculation, the behavior just described indicates further that bulk-bulk correlations are a significant if not dominant contribution to the hard ridge.

## 6.4 Discussion and Predictions

We see in this chapter that, when the $p_{t,min}$ limit of correlated bulk pairs is increased, not only does the amplitude of correlations decrease, but that we are also isolating particles with larger transverse boosts. As discussed in Ch. 5, transverse flow enhances angular correlations; increasing $p_{t,min}$ is accompanied by narrowing azimuthal width. Furthermore, we find that the soft correlations contribute to $\sim 75\%$ of the hard ridge amplitude but have a slightly narrower profile. Correlations of jets with flowing particles can make up the rest of the amplitude and have a wider azimuthal profile. The combination then does a suitable job of explaining these aspects of the hard ridge. We expect that, for some $p_{t,min}$, jets should completely dominate the spectrum, and the largest contribution to long range correlations comes from jet-bulk correlations.

We now calculate the combined effect of Glasma, flow, and jets on the correlation function. Adding the bulk-bulk and jet-bulk contributions, we obtain

$$\frac{\Delta\rho}{\sqrt{\rho_{ref}}} = \kappa\mathcal{R}\frac{dN}{dy}F_{BB}(\phi)\frac{\int\rho_{1,B}(p_t)}{\int\rho_{1,tot}(p_t)} + \kappa\mathcal{R}\frac{dN_{jet}}{dy}F_{JB}(\phi)\frac{\int\rho_{1,J}(p_t)}{\int\rho_{1,tot}(p_t)}. \tag{6.21}$$

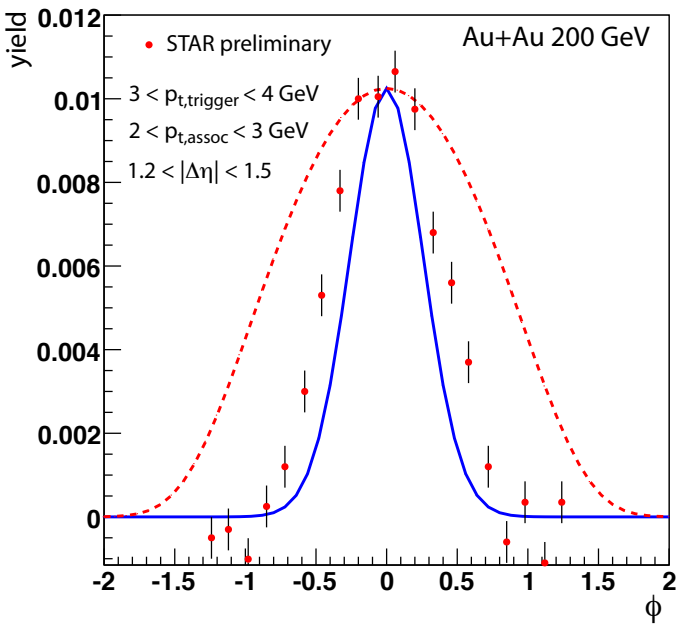


Figure 6.11: Comparison of the angular shape of the jet triggered ridge to long range bulk-bulk (blue line) and jet-bulk (dashed red line) correlations arbitrarily normalized to the measured peak height. Data from [3] (talk).

In order to compare to the yield of associated particles in the hard ridge, we combine (6.21) and (6.3) with the appropriate integration limits. We find that the agreement with the data in Fig.6.6 requires $p_s = 1.25$ GeV. The dashed red curve in Fig. 6.6 represents the contribution to the yield from correlations of jet and bulk thermal particles. This contribution is too wide. On the other hand, the bulk-bulk correlation function describing the effect of flow alone, which is given by the blue curve, is too narrow and the computed peak height is too small. To emphasize the disagreement of the angular shapes, we show the contributions normalized to the peak in Fig.6.11. The combination of the two effects shown as the black curve in Fig.6.6 gives nice agreement with both the amplitude and azimuthal width.

In Fig.6.12 and Fig.6.13, we plot predictions of the amplitude and azimuthal width vs. $p_{t,min}$ using (6.21). In each case the blue curves represent the bulk-bulk contribution that we have seen before in the lower panels of Figs.6.2, 6.3, 6.4, and 6.5 on a normal scale. We use a logarithmic scale here to highlight the the relative

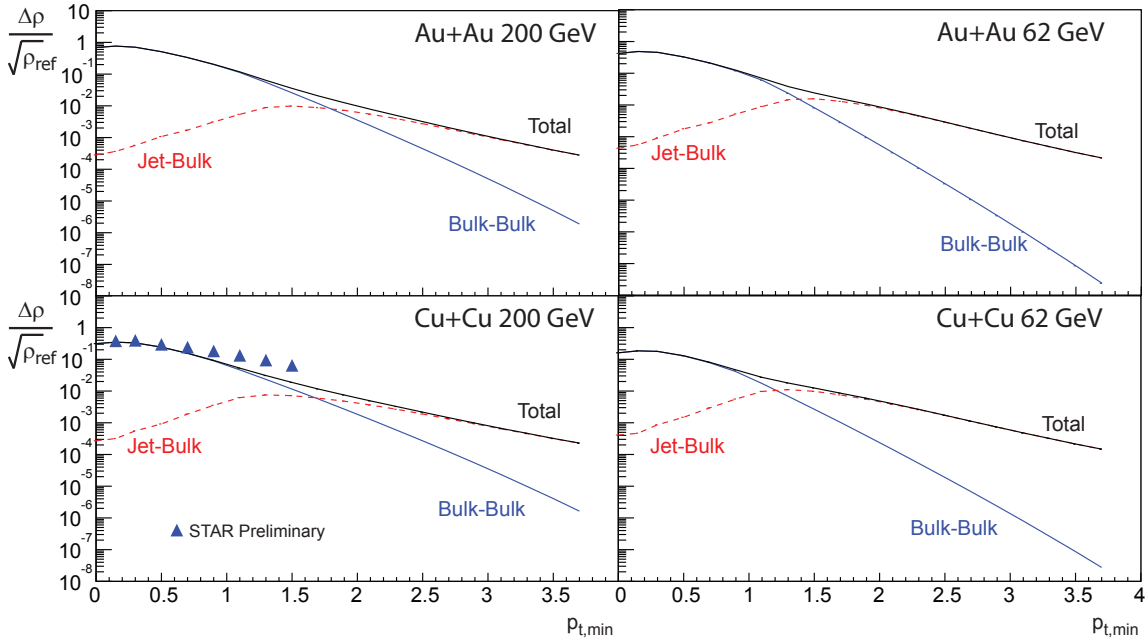


Figure 6.12: Amplitude of $\Delta\rho/\sqrt{\rho}$ highlighting the contribution for bulk-bulk and jet-bulk correlations for Au+Au and Cu+Cu 200 and 62 GeV. Caution: bulk and jet fractions determined by Au+Au 200GeV momentum spectrum only. Data from Ref.[26].

contributions of bulk-bulk and jet-bulk correlations. At low $p_{t,min}$, the contribution from jets is negligible and therefore the amplitude and width of (6.21) is determined by the bulk-bulk term. As the $p_{t,min}$ is increased, both the amplitude and the azimuthal width of the bulk-bulk term decreases, while the amplitude of the jet-bulk term increases.

The azimuthal width of jet-bulk correlations is roughly independent of $p_{t,min}$; the growth in the figures for $p_{t,min} > 1$ GeV is due to the growth of the jet fraction. Jet-bulk correlations should become a more significant fraction of the total as $p_{t,min}$ is increased, and the azimuthal width of the ridge should increase toward the jet-bulk width. The trends shown for Cu+Cu 200 GeV in Figs.6.3, 6.5, 6.12 and 6.13 follow preliminary data from Ref.[26]. The small difference may reflect the fact that our calculation omits the jet peak.

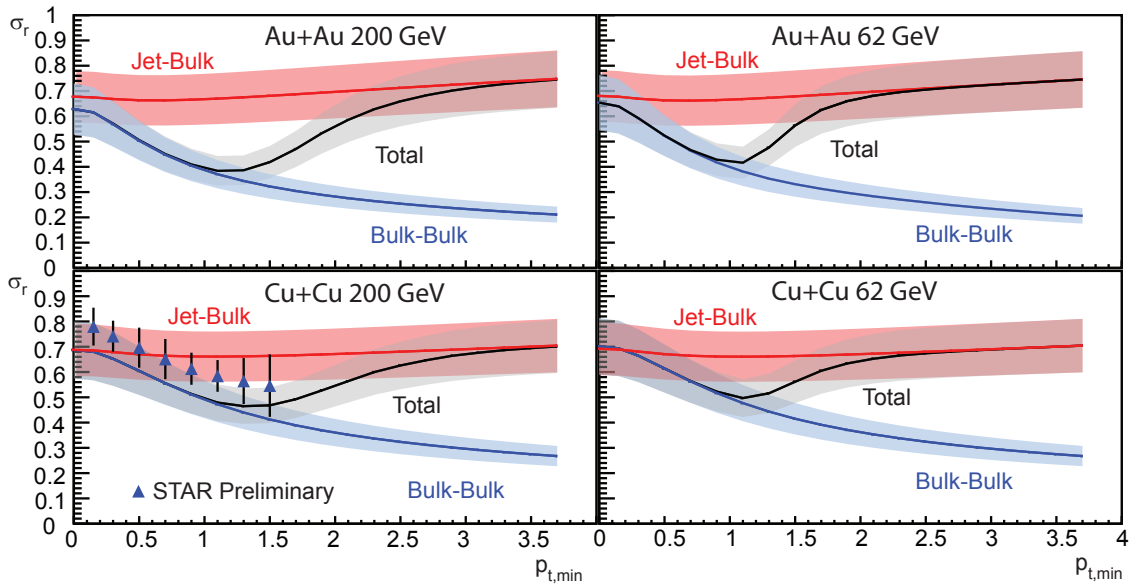


Figure 6.13: Azimuthal width of $\Delta\rho/\sqrt{\rho}$ comparing the contribution of bulk-bulk and jet-bulk correlations for Au+Au and Cu+Cu 200 and 62 GeV. Caution: bulk and jet fractions determined by Au+Au 200GeV momentum spectrum only. Data from Ref.[26].

We emphasize that the decrease of the bulk-bulk contribution to $\sigma_r$ with increasing $p_t$ in Figs.6.12 and 6.13 is a direct consequence of transverse flow and, consequently, is a firm prediction if the jet-bulk contribution is neglected. The roles of jets and other phenomena like recombination are less clear. We have chosen the model of Ref.[79] because it relies only on the well-studied phenomena of jet quenching. Our calculations using this model predict that the width should increase for higher $p_t$ ranges.

In this chapter, we make the first theoretical study of the soft ridge as a function of the pair $p_t$ range, and show that there is a significant contribution to the hard ridge from correlations of only soft particles. To include jet correlations with flux tubes, we reformulate [79], and determine the magnitude of jet-bulk correlations relative to bulk-bulk correlations. We find that we can explain the azimuthal width and amplitude of the hard ridge by combining bulk-bulk and jet-bulk correlations, and make predictions about the azimuthal width and amplitude of $\Delta\rho/\sqrt{\rho}$ for Au+Au

and Cu+Cu 200 and 62 GeV collisions. We find that transverse bulk flow and jet production affect the transverse momentum dependence of the ridge in different ways, as shown in Fig.6.13. If transverse flow is the only contribution, we predict that the azimuthal width of the near side peak $\sigma_r$ will decrease as $p_t$ increases. Jets may introduce new behavior depending on the way in which they influence the ridge.

It has been pointed out that a larger choice of $p_s$ is not outrageous, and therefore soft correlations alone can explain the total amplitude and nearly the azimuthal width of the hard ridge. This is not so terrible, since all of the long range correlation behavior depends on the rapidity reach of flux tubes, and the triggered ridge seems to show correlations at large $\eta$. In either case, our message remains that the primary cause of the ridge structure is not a medium response to jets, but a characteristic of the medium itself.

# Chapter 7

## Viscosity and the Ridge

While CGC particle production seems to provide an explanation for the long range shape of the ridge, shorter range transport effects such as shear viscosity play an integral roll in understanding the two dimensional shape of the ridge. In Chapters 5 and 6, we describe the amplitude and azimuthal shape of the near side ridge as a consequence of fluctuating initial conditions in combination with radial flow, and jet quenching. We envision that particle density fluctuations arise from CGC-Glasma flux tubes that stretch the full longitudinal extent of the collision. This condition results in a ridge resembling a flat pedestal in $\eta_r$. We recognize that the correlation structure is not flat in $\eta_r$, but rather a seemingly broad Gaussian shaped by shear viscous forces driving momentum density fluctuations toward a local equilibrium.

In Secs.7.1 and 7.2, we summarize the work of Gavin and Abdel-Aziz in Refs.[38, 153, 154] to develop the theory of viscous broadening of the ridge. The addition of viscous broadening not only adds a valuable piece of the puzzle in putting together aspects of the ridge, but also allows for measurement of the $p_t$-weighted ridge to serve as an independent measurement of the shear viscosity to entropy density ratio of the QGP. In Sec.7.3, as in Ref.[39], our contribution to this work builds on these results, and focuses on the the effects of transverse flow and freeze out in conjunction with viscous diffusion. The effects of radial flow and freeze out conditions are required to link this spatial rapidity broadening with the rapidity width of the $p_t$-weighted ridge.

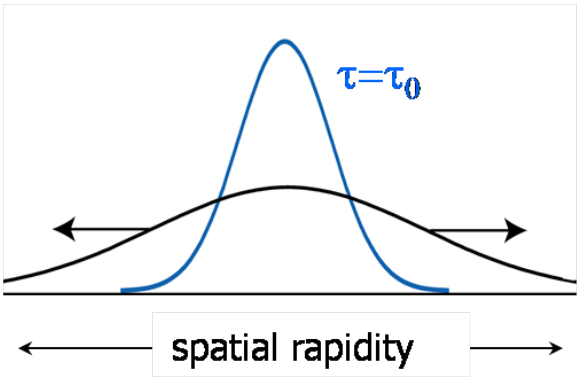


Figure 7.1: Cartoon of the broadening of the spatial rapidity correlation distribution due to shear viscosity. The blue curve is the correlation distribution at the formation of QGP at ($\tau = \tau_0$). The black curve is the distribution after some evolution, taking into account the effect of viscous diffusion.

## 7.1 Shear Viscosity, Diffusion, and Momentum Broadening

Momentum density fluctuations and the broadening of the rapidity width of the ridge can be studied in the context of the $p_t$-weighted ridge. Correlation measurements of the soft ridge, where correlated pairs are weighted by their momenta $p_{t1}p_{t2}$, amplifies the roll of momentum density on correlations [28, 53]. As a result, the azimuthal width of the $p_t$-weighted ridge will appear narrower than the soft ridge since higher $p_t$ pairs are weighted more heavily (higher $p_t$ pairs get a larger radial boost and have smaller opening angle, see Sec.5.3).

The $p_t$-weighted ridge also provides insight into the short range shape of the ridge in rapidity. Fluctuations in momentum density at early times give rise to shear viscous forces between neighboring fluid cells with different average momentum density. These viscous forces reduce the strong correlation in faster fluid cells, effectively spreading it to slower fluid cells. Figure 7.1 illustrates the effect of viscous diffusion on the initial spatial rapidity distribution (blue line), after some evolution of the system (black line). Viscosity tends to reduce fluctuations by distributing the excess momentum density over the collision volume. This effect broadens the rapidity profile fluctuations.

Nuclear collisions produce a fluid that flows outward with an average transverse

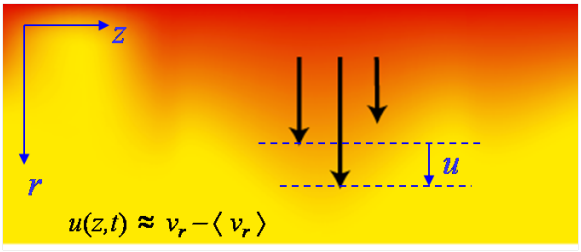


Figure 7.2: The transverse velocity deviates from the average by an amount **u** that varies throughout the collision volume. Viscosity drives this deviation toward zero.

velocity $v_r$. In the hydrodynamic description of these collision, we typically assume that $v_r$ varies smoothly with space time $(t, \mathbf{x})$ and is the same for all collisions of a fixed impact parameter. More realistically, small deviations $\mathbf{u}(\mathbf{x})$ relative to $v_r$ occur throughout the fluid, varying with each collision event. Such deviations occur, for example, because the number and location of nucleon-nucleon subcollisions varies in each event.

Viscous friction arises as neighboring fluid elements flow past each other as shown in Fig.7.2 from Sean Gavin and Mohamed Abdel-Aziz [153]. This friction drives $v_r$ toward the local average. The final size of the deviation depends on the magnitude of the viscosity, the initial temperature, and the lifetime of the fluid. In the local co-moving frame where $\langle v_r \rangle = 0$, we see the manifestation of the shear stress as the velocity deviation **u** varies as a function of longitudinal position $z$. The shear stress is defined as

$$T_{zr} = -\eta \partial u / \partial z. \tag{7.1}$$

Here, the energy-momentum conservation law $\partial_\mu T^{\mu\nu} = 0$ is satisfied by the stress-energy tensor $T^{\mu\nu} = (\epsilon + p)u^\mu u^\nu - p g^{\mu\nu} + \tau^{\mu\nu}$ where $\epsilon$ is the energy density, $p$ is the pressure, $u^\mu = \gamma(1, \mathbf{v})$ is the four-velocity of the fluid, and $\gamma = (1 - v^2)^{-1/2}$. Following Landau and Lifshitz *Fluid Mechanics*, we define our four-velocity to vanish when $T^{0i} = 0$ [155]. Then the dissipative contribution $\tau^{\mu\nu}$ depends only on viscosity

with $\tau^{00} = \tau^{0i} = 0$ and

$$\tau_{ij} = -\eta\{\nabla_i v_j + \nabla_j v_i - \frac{2}{3}\delta_{ij}\nabla\cdot\mathbf{v}\} - \zeta\delta_{ij}\nabla\cdot\mathbf{v}. \tag{7.2}$$

The bulk viscosity $\zeta$ resists compression or expansion in which $\nabla\cdot\mathbf{v} \neq 0$. We take $\zeta \ll \eta$.

The transverse momentum current of the fluid, which is generally $T_{0r} = \gamma^2(\epsilon+p)v_r$ is changed by the stress (7.1) such that $\mathrm{g}_t(\mathbf{x}) = T_{0r} - \langle T_{0r}\rangle = \delta T_{0r} \approx (\epsilon+p)u$ in the co-moving frame. Following from energy-momentum conservation, $\partial_\mu T^{\mu\nu} = 0$,

$$\partial \mathrm{g}_t/\partial t = -\partial T_{zr}/\partial z. \tag{7.3}$$

Near a point where $v_r = 0$, the momentum current $\mathrm{g}_t$ satisfies a first order diffusion equation,

$$\partial \mathrm{g}_t/\partial t = \nu\nabla^2 \mathrm{g}_t. \tag{7.4}$$

The kinematic viscosity is given by

$$\nu = \frac{\eta}{(\epsilon+p)} = \frac{\eta}{Ts} \tag{7.5}$$

where $T$ is the temperature and $s$ is the entropy density. This quantity measures the relative strength of the viscosity to the fluid's inertia, as is most apparent in the non relativistic limit where $(\epsilon+p) \to \rho$ with $\rho$ being the mass density ($c = 1$). In our relativistic system at small net baryochemical potential, $(\epsilon+p) \approx Ts$. Observe that our physically-motivated radial $\mathrm{g}(z,t)$ satisfies Eq.(7.4), as does any fluctuation $\mathrm{g}_t$ for which $\nabla\cdot\mathbf{g}_t = 0$.

Assuming Bjorken longitudinal flow in the $z$ direction coupled to radial flow $\mathbf{v}_r$ in

the transverse plane that depends only on $\mathbf{r}$ we can generalize (7.7) to

$$\frac{\partial \mathrm{g}_t}{\partial \tau} + \mathbf{v}_r \cdot \nabla_r \mathrm{g}_t + \mathbf{g}_t \cdot \nabla v_r = \nu \left( \frac{1}{\tau^2} \frac{\partial^2}{\partial \eta^2} + \nabla_r^2 \right) \mathrm{g}_t. \tag{7.6}$$

This equation can be used additionally to find the azimuthal broadening due to diffusion, and is a subject of future work.

For the purely longitudinal case, we write (7.4) in terms of spatial rapidity $\eta = 1/2 \ln((t+z)/(t-z))$ and proper time $\tau = (t^2 - z^2)^{1/2}$ e.g. (3.12) and (3.14), and find

$$\frac{\partial \mathrm{g}_t}{\partial \tau} = \frac{\nu}{\tau^2} \frac{\partial^2 \mathrm{g}_t}{\partial \eta^2}. \tag{7.7}$$

Defining the spatial rapidity width $V$ as

$$V \equiv \langle (\eta - \langle \eta \rangle)^2 \rangle = \frac{\int \eta^2 \mathrm{g}_t d\eta}{\int \mathrm{g}_t d\eta}, \tag{7.8}$$

for $\langle \eta \rangle = 0$ we follow Ref.[154], and translate momentum current diffusion (7.7) into a broadening of $V$. We multiply both sides of (7.7) by $\eta^2$ and integrate over $d\eta$ to obtain

$$\frac{dV}{d\tau} = \frac{2\nu}{\tau^2}. \tag{7.9}$$

In principle, $\eta$, T, and s can all vary with time, in which case we solve this equation numerically. As discussed in Ref.[38] we can take $\nu \approx$ *constant* and analytically compute the spatial rapidity broadening $\Delta V$ as,

$$\Delta V = \frac{2\nu}{\tau_0} \left( 1 - \frac{\tau_0}{\tau} \right) \tag{7.10}$$

where $\Delta V \equiv V - V(\tau_0)$, and $\tau_0$ is the formation time.

## 7.2 Diffusion and Correlations

We now take the information in Sec.7.1 and extend it to consider two particle correlations. In the spirit of Eq.(5.1), we write the two particle spatial correlation function

$$\mathbf{r}_g = \langle \mathrm{g}_t(\mathbf{x}_1)\mathrm{g}_t(\mathbf{x}_2)\rangle - \langle \mathrm{g}_t(\mathbf{x}_1)\rangle\langle \mathrm{g}_t(\mathbf{x}_2)\rangle \tag{7.11}$$

where the brackets indicate an ensemble of events. The difference $\Delta r_g = r_g - r_{g,eq}$, where $r_{g,eq}$ is the local equilibrium value, satisfies the diffusion equation

$$\left(\frac{\partial}{\partial\tau} - \frac{\nu}{\tau^2}\frac{\partial^2}{\partial\eta_1^2} - \frac{\nu}{\tau^2}\frac{\partial^2}{\partial\eta_2^2}\right)\Delta r_g = 0. \tag{7.12}$$

Then, $\Delta r_g = r_g - r_{g,eq}$ is broadened by momentum diffusion since diffusion spreads the rapidity of each particle in a given pair with a variance $\Delta V$. Rearranging (7.12) in to relative $\eta_r = \eta_1 - \eta_2$ and average $\eta_a = (\eta_1 + \eta_2)/2$ spatial rapidity coordinates, we have

$$\left(\frac{\partial}{\partial\tau} - \frac{2\nu}{\tau^2}\frac{\partial^2}{\partial\eta_r^2} - \frac{\nu}{\tau^2}\frac{\partial^2}{\partial\eta_a^2}\right)\Delta r_g = 0. \tag{7.13}$$

Similar to the method in the previous section, one can compute the widths of $\Delta r_g(\eta_r, \eta_a, \tau)$ in relative or average spatial rapidity, by multiplying (7.13) by $\eta_r^2$ or $\eta_a^2$ and integrating over both variables to find

$$\sigma^2 = \sigma_0^2 + 2\Delta V(\tau_f) \tag{7.14}$$

$$\Sigma^2 = \Sigma_0^2 + \Delta V(\tau_f), \tag{7.15}$$

where $\Delta\langle(\eta_r - \langle\eta_r\rangle)^2\rangle = 2\Delta V$ and $\Delta\langle(\eta_a - \langle\eta_a\rangle)^2\rangle = \Delta V$. Here, $\Delta$ represents the difference in the variance from its initial value. The result is that $\Delta r_g$, in relative spatial rapidity, grows from an initial value $\sigma_0$ where $\tau_f$ is the proper time at which

freeze out occurs. We can then take

$$\Delta r_g(\eta_r, \eta_a) \propto e^{-\eta_r^2/2\sigma^2} e^{-\eta_a^2/2\Sigma^2} \tag{7.16}$$

where (7.15) gives the width in relative rapidity and the width in average rapidity from (7.15) is $\Sigma$. Correspondingly, if one takes the 3+1D diffusion equation (7.6) for $\Delta r_g$, it takes the form

$$\Delta r_g(r_t, R_t, \eta_r, \eta_a) \propto e^{-r_t^2/2\sigma_r^2} e^{-R_t^2/2\Sigma_r^2} e^{-\eta_r^2/2\sigma^2} e^{-\eta_a^2/2\Sigma^2} \tag{7.17}$$

where the relative and average spatial transverse coordinates are $\mathbf{r}_t = \mathbf{r}_1 - \mathbf{r}_2$, $\mathbf{R} = (\mathbf{r}_1 + \mathbf{r}_2)/2$, and $\sigma_r$ and $\Sigma_r$ are the relative and average azimuthal widths respectively. As stated in Refs.[38, 39, 153, 154], $\Delta r_g$ is observable through measurement of the quantity

$$\mathcal{C} = \langle N \rangle^{-2} \langle \sum_{i \neq j} p_{ti} p_{tj} \rangle - \langle p_t \rangle = \langle N \rangle^{-2} \int \Delta r_g(\mathbf{x}_1, \mathbf{x}_2) dx_1 dx_2 \tag{7.18}$$

where brackets indicate an event average over all particles $i$ and $j$ and $\langle p_t \rangle \equiv \langle \sum p_{ti} \rangle / \langle N \rangle$.

## 7.3 Radial Flow and the Effects of Freeze Out

As we saw in Ch.5 and 6 momentum space correlations at freeze out are directly linked to initial state spatial correlations. In this section, we add the additional wrinkle that initial spatial correlations are altered by diffusion.

In Ch.5 we find that the azimuthal width of the soft ridge is enhanced (narrowed) by transverse flow. We find the same result in this section, albeit with two differences. The first difference is a consequence of the $p_t$ weighting of the soft ridge studied in this chapter. We see the second difference when we use the diffusion equation (7.6) for $\Delta r_g$ to calculate the broadening in (spatial) rapidity and transverse widths starting from some initial values which are not known.

Weighting the correlated pairs by the $p_t$ of the particles in the pair essentially suppresses the contribution from slower pairs. In the context of Ch.5, the slower pairs are those that come from fluid cells originating closer to the center of the collision volume and therefore receive less of a radial boost and have larger relative azimuthal angle. The result is that the $p_t$ -weighted ridge reflects the contribution of particle pairs with smaller azimuthal angle and therefore has a smaller azimuthal width.

In the case of the transverse distribution, we can make use of the same knowledge that lead to the CGC inspired correlation function (5.2). Here the initial relative transverse distribution takes the form of a delta function and the average transverse distribution follows (5.3) and diffusion drives them toward the form (7.17). This requires a numerical solution of (7.6) and is a subject of current investigation. Results presented in this section were obtained before determination of (5.2). Furthermore, as shown in Ref.[59], the CGC initial correlated pair distribution in relative rapidity is truly long range and approximately flat in the STAR acceptance. Long range correlations cannot be modified by shorter range effects such as diffusion since particle pairs contributing to this effect are causally disconnected. For this reason, *long range* CGC rapidity distributions do not provide information about $\sigma_0$. For the purposes of the results shown in this section, we take initial distributions to be Gaussian with widths set by those measured in peripheral collisions, where diffusion has little or no contribution.

The effect of diffusion is to spread out correlations over the volume. Given a long enough lifetime any distribution, even as sharp as a delta function, will tend toward a Gaussian shape. To include the effects of transverse flow and freeze out, we write the momentum correlation function as

$$\Delta r_g(\mathbf{p}_1,\mathbf{p}_2) = \int \Delta r_g(\mathbf{x}_1,\mathbf{x}_2)\frac{f(\mathbf{x}_1,\mathbf{p}_1)}{n_1(\mathbf{x}_1)}\frac{f(\mathbf{x}_2,\mathbf{p}_2)}{n_1(\mathbf{x}_2)}p_1^\mu d\sigma_{\mu 1}p_2^\mu d\sigma_{\mu 2}. \tag{7.19}$$

Equation (7.19) has a form consistent with (5.8), except now we replace the spatial correlation function $c(\mathbf{x}_1, \mathbf{x}_2)$ that is purely transverse with (7.17), $\Delta r_g(\mathbf{x}_1, \mathbf{x}_2)$, one that is representative of both transverse and longitudinal correlation distributions as well as the effects of diffusion. We make use of the formalism started in Ch.3, where the strength of flow is determined by fitting the measured $\langle p_t \rangle$ and elliptic flow coefficient $v_2$. The Boltzmann distribution $f(\mathbf{x}, \mathbf{p})$ follows (3.23), with Hubble-like expansion (3.1), so that $\gamma_{1,2}$ follows (3.29). Now (7.19) takes the form

$$\begin{aligned}
\Delta r_g(\mathbf{p}_1, \mathbf{p}_2) \quad = \quad & a \int e^{-\gamma_1 \frac{m_{t1}}{T} \cosh(y_1 - \eta_1)} e^{-\gamma_2 \frac{m_{t2}}{T} \cosh(y_2 - \eta_2)} \\
& \times e^{\frac{\lambda}{T}(\epsilon_x p_{x1} x_1 + \epsilon_y p_{y1} \mathrm{y}_1)} e^{\frac{\lambda}{T}(\epsilon_x p_{x2} x_2 + \epsilon_y p_{y2} \mathrm{y}_2)} \\
& \times e^{-(x_1 - x_2)^2/2\sigma_x^2 - (\mathrm{y}_1 - \mathrm{y}_2)^2/2\sigma_y^2} \\
& \times e^{-(x_1 + x_2)^2/8\Sigma_x^2 - (\mathrm{y}_1 + \mathrm{y}_2)^2/8\Sigma_y^2} \\
& \times e^{-\eta_r^2/2\sigma^2} e^{-\eta_a^2/2\Sigma^2} \\
& \times \tau_1 \tau_2 m_{t1} m_{t2} \cosh(y_1 - \eta_1) \cosh(y_2 - \eta_2) \\
& \times d\eta_1 d\eta_2 dx_1 dx_2 d\mathrm{y}_1 d\mathrm{y}_2, \qquad (7.20)
\end{aligned}$$

where $a$ is an overall normalization factor and

$$\sigma_x^2 = \sigma_r^2(1 + \alpha)/2 \qquad (7.21)$$

$$\sigma_y^2 = \sigma_r^2(1 - \alpha)/2 \qquad (7.22)$$

$$\Sigma_x^2 = \Sigma_r^2(1 + \beta)/2 \qquad (7.23)$$

$$\Sigma_y^2 = \Sigma_r^2(1 - \beta)/2, \qquad (7.24)$$

with $\alpha, \beta \approx 0$. For convenience, we rewrite all spatial coordinates in terms of relative and average coordinates so that $x = x_1 - x_2$, $X = (x_1 + x_2)/2$, and $dx_1 dx_2 = dx dX$. We apply the same convention for $\mathrm{y}_1$ and $\mathrm{y}_2$.

The gamma factor (3.29) complicates any analytic reduction of (7.20), forcing

multidimensional, resource-hungry Monte Carlo integration techniques. However, we observe the expansion factor $\lambda$ to be small at leading order, and approximate $\gamma_{1,2}$ as a constant. Now the $x$ and y terms of (7.20) factor and take the form

$$\int e^{\frac{\lambda}{2T}\epsilon_x(p_{x1}-p_{x2})x} e^{-x^2/2\sigma_x^2} dx \int e^{\frac{\lambda}{T}\epsilon_x(p_{x1}+p_{x2})X} e^{-X^2/2\Sigma_x^2} dX$$

$$= 2\pi\sigma_x\Sigma_x e^{\frac{\lambda^2}{8T^2}\epsilon_x^2(p_{x1}-p_{x2})\sigma_r^2} e^{\frac{\lambda^2}{2T^2}\epsilon_x^2(p_{x1}+p_{x2})\Sigma_r^2}, \tag{7.25}$$

and similarly for y. With some algebra we obtain

$$\begin{aligned}
\Delta r_g(\mathbf{p}_1,\mathbf{p}_2) \;=\; & a\int e^{-\gamma_1\frac{m_{t1}}{T}\cosh(y_1-\eta_1)} e^{-\gamma_2\frac{m_{t2}}{T}\cosh(y_2-\eta_2)} e^{-\eta_r^2/2\sigma^2} e^{-\eta_a^2/2\Sigma^2} \\
& \times e^{\frac{\lambda^2}{8T^2}(\Sigma_r^2(1+\alpha\epsilon)+\frac{\sigma_r^2}{4}(1+\beta\epsilon))(p_{t1}^2+p_{t_2}^2)} \\
& \times e^{\frac{\lambda^2}{4T^2}(\Sigma_r^2(1+\alpha\epsilon)-\frac{\sigma_r^2}{4}(1+\beta\epsilon))p_{t1}p_{t_2}\cos\phi} \\
& \times e^{\frac{\lambda^2}{8T^2}(\Sigma_r^2(\alpha+\epsilon)+\frac{\sigma_r^2}{4}(\beta+\epsilon))p_{t1}^2\cos(2\Phi+\phi)} \\
& \times e^{\frac{\lambda^2}{8T^2}(\Sigma_r^2(\alpha+\epsilon)+\frac{\sigma_r^2}{4}(\beta+\epsilon))p_{t2}^2\cos(2\Phi-\phi)} \\
& \times e^{\frac{\lambda^2}{4T^2}(\Sigma_r^2(\alpha+\epsilon)-\frac{\sigma_r^2}{4}(\beta+\epsilon))p_{t1}p_{t2}\cos(2\Phi)} \\
& \times \tau_1\tau_2 m_{t1}m_{t2}\cosh(y_1-\eta_1)\cosh(y_2-\eta_2)d\eta_r d\eta_a,
\end{aligned} \tag{7.26}$$

with the relative azimuthal angle $\phi = \phi_1 - \phi_2$ and the average azimuthal angle $\Phi = (\phi_1 - \phi_2)/2$.

Alternately, we solve (7.20) numerically via Monte Carlo integration with no change in the gamma factor (3.29). Using the all Monte Carlo technique, we find the quantity $\Delta\rho_{p_t}(y_r,\phi) = \int \Delta r_g(\mathbf{p}_1,\mathbf{p}_2)p_{t1}p_{t2}dp_{t1}dp_{t2}d\Phi$ and construct the short range component of $\Delta\rho/\rho_1\rho_1$ for the near side in Fig.7.3. We see that there is narrowing in azimuth due to transverse flow, but it is also important to note that transverse flow effects the rapidity width as well.

Transverse flow effects compete with those of diffusion. While diffusion tends

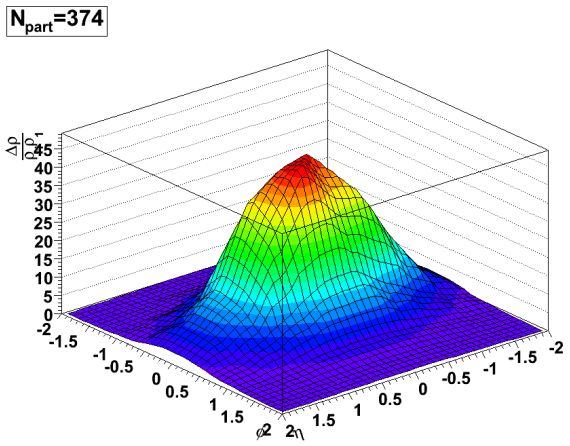


Figure 7.3: The ridge response at freeze out to viscous broadening giving widths $\sigma_\eta$ and $\sigma_\phi$ .

to spread out correlations over the volume, flow focuses correlations into a narrower phase space by increasing particle momenta based on their position. For the azimuthal case, we have describe this effect in detail in Ch.5.

Rapidity narrowing due to transverse flow is less obvious but can be seen through examination of the definition of rapidity $y = \tanh^{-1}(p_z/E)$ with $E = \sqrt{m^2 + p_t^2 + p_z^2}$. An increase in $p_t$ only will increase $E$ and not $p_z$, reducing the rapidity $y$ asymptotically toward zero. The rapidity of particles with different $p_z$ but same transverse boost will decrease at a different rate due to the $\tanh^{-1}$ behavior and the relative rapidity $y_1 - y_2$ will also tend toward zero asymptotically.

STAR measures the quantity

$$\Delta\sigma^2_{p_t:n} = \langle N\rangle^{-1}\langle\sum_{i\neq j}(p_{ti} - \langle p_t\rangle)(p_{tj} - \langle p_t\rangle)\rangle, \tag{7.27}$$

which is designed to minimize the number density contribution [28, 53]. The covariance $\mathcal{C}$ is sensitive to the variation of the $p_t$ of particles as well as their number density; both quantities effect the momentum current density. These quantities are related by $\langle N\rangle^{-1}\Delta\sigma^2_{p_t:n} = \mathcal{C} - \langle p_t\rangle^2\mathcal{R}$, where $\mathcal{R}$ measures the number density contribution (5.4). STAR employs $\Delta\sigma^2_{p_t:n}$ to construct a correlation function as a

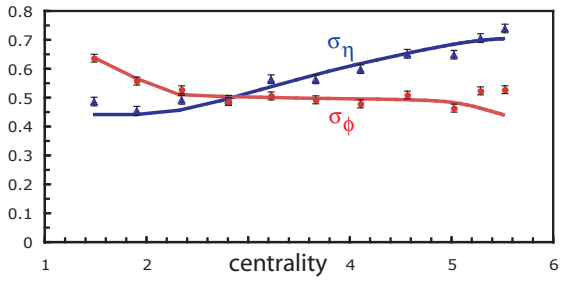


Figure 7.4: Centrality dependence of the width of the near side peak in $\phi$ and $\eta$ as a function of centrality ($2N_{col}/N_{part} = \nu$). The data is from Ref[28].

function of rapidity and azimuthal angle. In essence, they measure $\Delta\sigma^2_{p_t:n}$ in various (pseudorapidity) $\eta_r$ and $\phi$ bins and construct a correlation function $F(\eta_r, \phi)$ defined by $\Delta\sigma^2_{p_t:n} = \int F d\eta_r d\phi$ [28, 53]. Fig.7.4 shows the widths of the near side peak in azimuth $\sigma_\phi$ and rapidity $\sigma_\eta$. Fixing our notation, $\eta_r$ is relative pseudorapidity which we take to approximately be relative rapidity $y$ in (7.20). Centrality is measured using the definition $2N_{col}/N_{part} = \nu$. We find the widths taking $\sigma^2_\phi = \int \phi^2 \Delta r_g(\mathbf{p}_1, \mathbf{p}_2) p_{t1} p_{t2} d^3p_1 d^3p_2 / \int \Delta r_g(\mathbf{p}_1, \mathbf{p}_2) p_{t1} p_{t2} d^3p_1 d^3p_2$ and $\sigma^2_\eta = \int y^2 \Delta r_g(\mathbf{p}_1, \mathbf{p}_2) p_{t1} p_{t2} d^3p_1 d^3p_2 / \int \Delta r_g(\mathbf{p}_1, \mathbf{p}_2) p_{t1} p_{t2} d^3p_1 d^3p_2$. We see in Fig.7.4 that for the constant $\gamma_{1,2}$ calculation (7.26), we find nice agreement with data.

The impact of diffusion, flow, and freeze out have a complicated and intertwined relationship with the shape of the near side ridge. Consequently, information from the $p_t$ -weighted ridge and $\sigma_\phi$ and $\sigma_\eta$ can constrain the shear viscosity to entropy density ratio since they directly result from calculation of $\sigma$ and $\sigma_r$ in (7.17). This was first shown in Ref.[38]. Moreover, $\sigma$ and $\sigma_r$ are sensitive to the lifetime of the fluid and therefore can distinguish between a constant or time dependent viscosity to entropy density ratio.

# Chapter 8

## Other Aspects of the Ridge and Future Work

Thus far, our study of the 2D correlation structure has focused exclusively on the near side ridge, but the total landscape is a complicated structure with many aspects remaining to be understood. We describe the long range features of the near side with a CGC inspired model in which particles are initially correlated at the point of production. Additionally, we fold in a theory of shorter range correlations based on viscous diffusion, but together, we have yet to even describe all features of the near side. The near side appears to consist of a "jet peak" convoluted with a broader distribution, sitting on a pedestal. There is also the "away side" structure, centered at $\phi = \pi$ and normally thought of as a consequence of momentum conservation.

Thus far, we have not addressed the jet peak or the away side structures. Additionally, we have not expanded the short range in rapidity treatment to describe all available data, i.e. the unweighted soft ridge. The description of all features under one framework is the primary goal for the future. Additionally, a serious difficulty in our previous correlation studies has been a lack of access to realistic transport and full hydrodynamical models. Using the NEXSPHERIO code, ridge correlation studies along this line have begun, but have only achieved qualitative ridge shapes [65]. One could develop a competitive realistic model, with transport models using various initial conditions such as BAMPS [156, 157, 158, 159], and UrQMD with intermediate hydrodynamical evolution [160, 161, 162, 163].

## 8.1 The Jet Peak

We imagine that the jet peak sitting on the ridge is due to jet fragmentation outside of the medium. Similarities in the azimuthal and rapidity width of the jet peak with that of an isolated jet are evidence of this. Additionally, the amplitude of the jet peak does not seem to grow with centrality. Following from this, we should be able to reproduce the jet peak using PYTHIA or fragmentation models. The simplest next step is to directly add these correlations as a continuation of (6.21) where

$$\Delta\rho(\mathbf{p}_1,\mathbf{p}_2) = \Delta\rho_{_{BB}}(\mathbf{p}_1,\mathbf{p}_2) + \Delta\rho_{_{JB}}(\mathbf{p}_1,\mathbf{p}_2) + \Delta\rho_{_{JJ}}(\mathbf{p}_1,\mathbf{p}_2). \tag{8.1}$$

Here the subscripts $B$ and $J$ correspond to the correlation of a bulk or jet particle distributions. We remark that the long range behavior of the ridge is due mostly to the production and flow of bulk particles rather than the modification of the medium by the jet. As a result, the strength of the correlation then scales with soft particle production, where the last term in (8.1) is due entirely to correlations between jet fragments.

We observe, however, that the jet peak is not simply sitting on a flat pedestal, but more like a broad Gaussian. This broad Gaussian structure evolves from an initial distribution that may or may not be related to the passage of a jet. Viscous corrections to this initial distribution may be enough to explain the soft ridge width in central collisions without the presence of the jet (i.e. the jet contribution is small), but for other centralities and other $p_t$ ranges including the hard ridge the interplay of jet-medium modifications and viscous diffusion could become important.

## 8.2 The Away Side

The away side structure at $\phi = \pi$ must be explainable within the same correlation framework. A hydrodynamic explanation of the near side ridge would demand a struc-

ture at the away side to conserve momentum. Indeed, such a structure is observed, but its observed magnitude and behavior with centrality are yet to be explained. This issue can have profound consequences for all correlation probes, including HBT measurements, and may also affect single particle observables. Aside from its intrinsic interest, understanding of the away-side region can shed light on jet-triggered correlations, as the proposed Mach cone sits atop just such an away side structure.

In an individual event, the vector sum of transverse momenta must vanish. Causality limits the transport of momenta depending on the size and time frame of the system. A momentum diffusion length would determine the scale of causally connected domains in which any particle could transfer momentum to any other particle in the same domain.

Momentum conservation should modify the correlation function following $\Delta\rho(\mathbf{p}_1, \mathbf{p}_2) \rightarrow \Delta\rho(\mathbf{p}_1, \mathbf{p}_2) + \Delta\rho_{mom}(\mathbf{p}_1, \mathbf{p}_2)$, where

$$\Delta\rho_{mom}(\mathbf{p}_1, \mathbf{p}_2) = -\mathcal{A}\cos(\phi) \tag{8.2}$$

$$\mathcal{A} = \frac{2}{\langle N\rangle\langle p_t\rangle}\int p(\mathbf{x}_1, \mathbf{x}_2) f(\mathbf{x}_1, \mathbf{p}_1) f(\mathbf{x}_2, \mathbf{p}_2) p_1^\mu d\sigma_{\mu 1} p_2^\mu d\sigma_{\mu 2}, \tag{8.3}$$

and $p(\mathbf{x}_1, \mathbf{x}_2)$ is the probability that both particles come from the the same causally connected domain. We assume that the system is large and in local equilibrium. Borghini et al. first addressed the affect of momentum conservation on correlations, but considered a globally-equilibrated fireball in which all of the particles share momentum [164, 165, 166, 167, 168]. In that extreme case, $p \equiv 1$. Chajecki and Lisa apply Borghini-type corrections to HBT data, and find disagreement with data [169, 170]. They introduced the notion of causally-connected sub-volumes, and argued empirically that these sub-volumes contain only $\sim 200 - 300$ particles in central Au+Au collisions.

In parallel, we plan to study how well (8.2) and (8.3) explain data for $\eta - \phi$ correlations, HBT,and other signals. Preliminary indications are that (8.3) can describe the STAR measurements of $\mathcal{A}$ as a function of centrality, but quantitative comparison requires detailed understanding of the experimental analysis method. Lastly, this calculation will expand a framework that can be tested in transport and hydrodynamical models which inherently include the concept of momentum conservation.

## 8.3 Rapidity Dependence

Ref.[65] obtains long range correlations using NEXUS initial conditions. The principle ideas behind the formation of the ridge remain the same; initial parton density fluctuations that are long in relative rapidity are modified by hydrodynamical flow. The major differences from our model are the transverse size and parton distribution of the fluctuation, and the prescription for radial expansion. We argue in [36, 37] that our quantitative agreement with data largely reflects the choice of initial conditions, but we take a simple prescription of transverse expansion. Ref.[65], however, implements full 3+1 hydrodynamics through the SPHERIO code and obtains a ridge-like structure, but does not quantitativly reproduce the data.

In our picture, the longitudinal extent of the ridge depends on the distribution of lengths of flux tubes. In [36, 37], we have approximated the flux tubes to have infinite length, thus producing a flat ridge. Ref.[59] has shown that in the CGC picture, two gluon cumulants from early stage color flux tubes exist out at relative rapidity separations larger than that observed by experiment, but do die off at large rapidities. We plan to relate this to flux tube lengths and adopt phenomenological string fragmentation methods to describe the growth in the $\eta$ width of the ridge with centrality. Merging such a model of initial state fluctuations with a full viscous hydrodynamical approach would be a major step in understanding the full correlation landscape.

# Chapter 9

# Discussion and Conclusions

In this chapter, we remark on other ridge models with intent on comparison to our own. All models have advantages and shortcomings that are illuminated by careful comparison to data [29]. We then summarize the results presented in this work.

## 9.1 Other Models

Theoretical interpretations of the near side ridge fall into three categories. The first category attributes the ridge to the medium response to the passage of a jet. A variety of mechanisms are given, including momentum broadening [67, 68, 69, 74] and transfers of energy via successive momentum kicks from the jet parton [73, 75, 76]. The second category of ridge models couples the formation of hot spots, bubbles, or flux tubes with hydrodynamical transverse flow [25, 60, 62, 65, 79]. Our model falls into this category. The third category attributes the ridge to parton recombination or coalescence [70, 71].

Jets can loose energy in the dense medium by Bremsstrahlung radiation of gluons. Refs. [67, 68, 69, 74] argue that momentum broadening of this radiation occurs either by strong collective flow or turbulent color fields. These calculations do find a broadening in relative rapidity $\eta$, however smaller than seen in experiment. Refs.[67, 69] find Gaussian widths of $\sigma_\eta = 0.4 - 0.5$, where STAR preliminary results find $\sigma_\eta \sim 1.4$ [3], and PHOBOS results suggest the ridge extends even further [4, 5]. These models

Figure 9.1: At Quark Matter 2009, Jamie Nagle "kills" ridge models, using this image of the grim reaper, while discussing what can be learned in the process [29].

would further predict a reduction in broadening with the increase in the $p_t$ of the trigger and cannot describe the soft ridge in which jets play a minimal role.

In the "Momentum Kick" model [73, 75, 76], bulk medium particles suffer initial interactions with a jet and receive momentum kicks in the direction of the jet particle. These kicked particles, depending on the strength of a momentum transfer parameter, account for the ridge yield and slightly flatter thermal spectrum. The shape of the ridge seems to depend on the $p_t$ and rapidity distributions of the kicked partons. This model finds a wider width in relative azimuthal angle $\sigma_\phi \sim 0.5 - 0.7$ where STAR measures a width $\sigma_\phi \sim 0.25 - 0.4$. Again, this model would also not be able to explain the soft ridge.

The work presented here fits into the second category of ridge theories. Correlated partons arise from a common transverse fluctuation in parton density. These fluctuations or "hot spots" extend longitudinally but are small in transverse size. Azimuthal correlations arise due to the relationship between hot spots and their transverse boost vector, an idea originally proposed by Voloshin [60]. Ref. [25], incorporates this ra-

dial boost model with a description of hot spots using CGC-Glasma theory. This description finds general agreement with the soft ridge amplitude vs. centrality for Au+Au 200 GeV collisions, but does not explain the azimuthal shape or behavior with centrality. Furthermore, this model does not provide any connection to the hard ridge.

In this work, we improve this theory, finding that the Glasma+flow conditions can indeed describe the azimuthal profile of both the soft and hard ridges. Additionally, we show that the Glasma conditions allow for common descriptions of the soft ridge for different collision systems and energies. However, our approximations lead to a flat ridge in relative rapidity $\eta$ for all centralities. STAR data shows, however, that the ridge width grows with centrality [1, 26, 51].

Although produced by different mechanisms, jet triggers and thermal partons gain correlations based on a common location in the transverse plane. An idea presented by Shuryak [79] and discussed in detail in Sec. 6.2, Ref. [79] gives no explanation of the longitudinal extent of the fluctuation and is therefore unable to estimate the magnitude of the effect, but calculates an azimuthal distribution that is wider than the measured data. In this work we address and incorporate these features. We both find the magnitude of this contribution to the hard ridge and show that this wide correlation in azimuth, when combined with narrow soft ridge correlations, improves our agreement with the hard ridge.

The parton bubble model (PBM) [62] relies on a similar mechanism, where transversely boosted bubbles or clusters of partons from the PBM event generator are correlated with HIJING jet events. This model finds a stinkingly similar looking correlation structure to the hard ridge. They further decompose the near side, showing that the broad ridge structure is still seen after removing all particle pairs except those that come from the same bubble. Conversely after removing all background pairs as well as all bubble particles, a jet peak is seen. Further, more quantitative,

comparisons to data could be exciting.

Additional qualitative support for this category of ridge models is found in Ref. [65]. Correlation analysis is preformed using the NEXSPHERIO event generator and full hydrodynamical code. Here initial conditions taken from NEXUS [171] strings produce hot spots that evolve following hydrodynamics from the SPHERIO code [172]. They find both a long range ridge and what looks like a jet peak, though no jets are present. Although further quantitative comparison is needed, it is precisely this approach that would provide a full description of the correlation landscape since hydrodynamics automatically accounts for energy and momentum conservation.

The recombination model [70, 71] fills the final category for ridge explanations. This model attempts to address both ridges as the same phenomenon. The authors explain that ridges arise because thermal partons are enhanced by semi-hard scatterings at early times and form hadrons at late times via recombination. They note, however, that in the absence of a theoretical framework to calculate the enhancement, the thermal distributions of ridge particles is extracted from data. This work points out the importance of late stage effects such as hadronization, as well as the consequences of the geometrical orientation of jet triggers on measured ridge yields.

## 9.2 Conclusions

In this work, we develop a beginning theoretical framework for understanding some of the features of the ridge seen in two particle correlation studies at RHIC. Specifically, we explore the near side ridge, its long range behavior, and the connection between the soft and hard ridge measurements. Our original interest in the ridge, however, stems from the viscous broadening seen in the $p_t$ -weighted ridge from which Gavin and Abdel-Aziz extracted a shear viscosity to entropy density estimate [38]. Our ultimate goal is to expand the work presented here to understand the full $(\eta - \phi)$ correlation landscape.

Possibly the most striking feature of the ridge is that two particle correlations seemingly extend to a long range in $\eta$. Causality limits the influence of transport dynamics past $\sim 1-2$ units in $\eta$, but the PHOBOS measurement indicates a ridge in the interval $-4 < \eta < 2$ [4, 5]. These long range correlations, then must arise at the earliest stages of the collision when the first partons are produced. At the instant of a collision, CGC theory predicts the formation of longitudinal flux tubes with small transverse size. In our simple view, rapid longitudinal expansion stretches these tubes to long distance, and the tubes then thermalize into partons. Realistically, tube desolation begins before before longitudinal expansion is complete. Although now causally separated, partons coming from the same tube, no matter the rapidity difference, are correlated by their common spatial (radial) origin. Transverse flow then builds and provides a transverse boost to particle density fluctuations (emerging from tubes) based on their initial radial position. Combining these two aspects, we find that we can explain the amplitude and azimuthal width of the soft ridge (away from the jet peak). In particular, we find that the azimuthal shape of the ridge is due to transverse flow, which we include via a blast wave model. We fix the amplitude in 200 GeV Au+Au collisions only, and find that we cannot explain the changes with centrality or collision energy without the inclusion of CGC-Glasma conditions. Additionally, we are able to predict the soft ridge azimuthal width and amplitude for Cu+Cu systems only through appropriate adjustment of the CGC parameter $Q_s$.

The differences between the soft and hard ridges is another debated question, since the soft ridge is intended to study bulk effects, where the hard ridge is intended to study medium modifications from the passage of a jet. To test our model in the context of the hard ridge, we perform our soft ridge calculation for increasingly higher $p_t$ ranges. We find that as the soft ridge becomes harder, the amplitude drops and the azimuthal width narrows. This behavior is expected since the $p_t$ limits eliminate the lower momentum pairs, lowering the correlation strength and isolating pairs with

higher $p_t$ and narrower relative azimuthal angle. These trends are supported by STAR measurements [26]. Performing our soft ridge calculation with the hard ridge asymmetric $p_t$ limits, we find a soft contribution to the hard ridge that accounts for $\sim 75\%$ of the hard ridge amplitude, but has a narrow azimuthal profile.

Following ideas in Ref. [79], we include incidental correlations of jets with flux tubes based on common production positions. Measured jet emissions from the bulk are biased either toward the surface or toward radial emission due to quenching, while radial flow pushes bulk particles toward more radial trajectories. The angular correlation between the jet and bulk particles is too wide to explain the data alone, and makes up only $\sim 25\%$ of the amplitude. The combination of Bulk-Bulk and Jet-Bulk correlations provides nice agreement with the hard ridge central amplitude and azimuth width. We conclude from this that the soft and hard ridges arise mainly from the same phenomenon, an idea that surprises some [173, 174].

The azimuthal profile of the ridge could then be used to distinguish between bulk and jet effects. As seen in Fig. 6.13, as the minimum $p_t$ of the soft ridge is increased the azimuthal width should decrease until the effects of jets becomes dominant at which point the width should increase again.

Thus far we have largely neglected the rapidity dependence of the ridge. However, shear viscosity can broaden the rapidity correlations of momentum current correlations as seen in Ref. [28]. As suggested by Gavin and Abdel-Aziz in Ref. [38], measuring $\mathcal{C}$ allows access to the momentum correlation function $\Delta r_g$. This work is underway, see e.g.[175, 176]. Freeze out effects and radial flow link the spatial widths after diffusion with the momentum widths taken from the ridge shape. Information on $\sigma_\phi$ and $\sigma_\eta$ can then constrain the shear viscosity to entropy density ratio extracted from $\mathcal{C}$. Further constraint would come from determining the initial widths before viscous diffusion.

Lastly, we remark that there is still much work to be done before we can fully

explain all features of the ridge. We must focus on descriptions of both the jet peak as well as the away side in the context of our framework. To a larger extent a complete description of the ridge would entail a combination of a theoretical description of rapidity and azimuthal widths at the QGP formation time (i.e. with CGC theory), with a more realistic full hydrodynamical model.

# Appendix A

## Appendix A: Kinematic Variables

In this Appendix, I will review some useful kinematic variables common to relativistic heavy ion collisions. They are defined in such a way that they have simple properties under Lorentz transformations. We also make use of natural units so $c = \hbar = 1$.

The space-coordinates of a point are defined by the 4-vector

$$x^\mu = (x^0, x^1, x^2, x^3) = (t, \vec{x}) = (t, x, y, z). \tag{A.1}$$

Similarly, the momentum vector is

$$p^\mu = (p^0, p^1, p^2, p^3) = (E, \vec{p}) = (E, p_x, p_y, p_z). \tag{A.2}$$

These covariant vectors transform with the space-time metric tensor

$$g_{\mu,\nu} = \begin{pmatrix} 1 & 0 & 0 & 0 \\ 0 & -1 & 0 & 0 \\ 0 & 0 & -1 & 0 \\ 0 & 0 & 0 & -1 \end{pmatrix}$$

such that $g_{\mu\nu}x^\mu = x_\nu$.

## A.1 Light Cone Variables

The light-cone coordinates are defined as

$$x^{\pm} = (t \pm z)/\sqrt{2}. \tag{A.3}$$

Similarly the light-cone momentum is

$$p^{\pm} = (p^0 \pm p^z)/\sqrt{2}. \tag{A.4}$$

The scalar product in these coordinates becomes

$$x \cdot p = x^+ p^- - x^- p^+ - x_t \cdot p_t \tag{A.5}$$

so the uncertainty principle is now

$$x^{\pm} p^{\mp} \geq 1. \tag{A.6}$$

## A.2 Rapidity

The rapidity variable, $y$, is defined in terms of the total energy and longitudinal momentum of a particle such that

$$y = \frac{1}{2} \ln \left( \frac{p_0 + p_z}{p_0 - p_z} \right). \tag{A.7}$$

It can be thought of as the ratio of the forward light-cone momentum to the backward light-cone momentum. Rapidity is a convenient way of expressing the longitudinal energy of a particle, since it only requires an additive constant to change frames of reference. Other relations of the rapidity, energy, and longitudinal momentum

include,

$$y = \tanh^{-1} \frac{p_z}{E} \tag{A.8}$$

$$p_z = m_t \sinh y \tag{A.9}$$

$$E = m_t \cosh y \tag{A.10}$$

with $m_t = \sqrt{m^2 + p_t^2}$.

Experimentally, it is more difficult to measure the energy of a particle than the momentum. Therefore, experiments often report the pseudorapidity variable

$$\eta = -\ln[\tan(\theta/2)] \tag{A.11}$$

which depends on the angle, $\theta$, the particle makes with the beam (longitudinal) axis. Its relation to rapidity is more clear when written in the form

$$\eta = \frac{1}{2} \ln \left( \frac{|\vec{p}| + p_z}{|\vec{p}| - p_z} \right). \tag{A.12}$$

Like the rapidity variable, there are further relations of with total momentum and longitudinal momentum that are useful:

$$\eta = \tanh^{-1} \frac{p_z}{|\vec{p}|} \tag{A.13}$$

$$p_z = p_t \sinh \eta \tag{A.14}$$

$$|\vec{p}| = p_t \cosh \eta \tag{A.15}$$

taking $p_t = \sqrt{\vec{p}^2 - p_z^2}$. The relationship between $y$ and $\eta$ is even more clear when one compares equations (A.9) and (A.14) . At very large $p_z$, the two quantities are essentially the same.

We can also define a space-time rapidity

$$\eta_s = \frac{1}{2} \ln \left( \frac{x^+}{x^-} \right). \tag{A.16}$$

In terms of the space-time position, the variable $\eta_s$ also transforms with an additive constant. After a longitudinal boost we have

$$\frac{z}{t} = \tanh \eta_s \tag{A.17}$$

$$z = \tau \sinh \eta_s \tag{A.18}$$

$$t = \tau \cosh \eta_s. \tag{A.19}$$

Here $\tau = \sqrt{t^2 - z^2}$ is the proper time, which is invariant under longitudinal boost. Note that by the uncertainty principle, a particle will have $m_t \sim 1/\tau$, and that up to a constant of order one, rapidity is defined as

$$y = \frac{1}{2} \ln \left( \frac{p^+}{p^-} \right) \sim \ln \left( \frac{p^+}{m^t} \right) \sim \ln \left( \frac{x^+}{\tau} \right) \sim \eta_s. \tag{A.20}$$

Thus, all rapidities in momentum space and coordinate space are of the same order of magnitude. [18]

## A.3 Momentum Fractions

Quantum field theory approaches relativistic scattering as interactions of fermions through the transfer of a virtual vector boson. Deep inelastic scattering, experiments for example probe the structure of a proton through high a high energy collision with an electron. The electron has 4-momentum $k$ and scatters elastically with a quark inside the proton. The collision with the proton is inelastic; the remaining quarks and the kicked quark must fragment into hadrons. The electron collision with the quark however is elastic, and we can determine the momentum transfer in the collision $q$

by measuring only the final momentum of the electron. The electron moves off with some new momentum $k'$ and the momentum transfer to the kicked quark is defined as

$$q = k - k'. \tag{A.21}$$

If the original momentum of the kicked quark $p$ is some fraction $x$ of the total momentum of the proton $P$, so $p = xP$ then its final momentum is $p + q = xP + q$. The invariant mass of the scattered quark is then

$$m_q^2 = (p+q)^2 = 2\vec{p}\cdot\vec{q} + q^2. \tag{A.22}$$

Defining the momentum transfer $Q^2 \equiv -q^2$ and assuming that the parton mass is much less than $Q^2$, (A.22) becomes

$$0 = 2\vec{p}\cdot\vec{q} - Q^2 = 2x\vec{P}\cdot\vec{q} - Q^2, \tag{A.23}$$

and

$$x = \frac{Q^2}{2\vec{P}\cdot\vec{q}} = \frac{Q^2}{2M\nu} \tag{A.24}$$

where $M$ is the proton mass and $\nu = E - E'$ is the energy transfer. Finally, taking the Mandelstam variable $\hat{s}$ we have

$$\hat{s} = (p+k)^2 = 2\vec{p}\cdot\vec{k} = 2x\vec{P}\cdot\vec{k} = xs \tag{A.25}$$

where the electron and proton masses have been neglected and $s$ is the center of mass energy of the collision.

## Appendix B

## Appendix B: The Glauber Geometric Approach to Nucleus-Nucleus Collisions

In this appendix, we review the Glauber model of nuclear collisions following [20, 87, 88, 177].

At high enough energies in nuclear collisions, the paths of colliding nucleons can be approximated by straight lines. However, depending on the density of the colliding nuclei, and the geometry of the collision, a nucleon in the projectile nucleus can suffer multiple scatterings during its passage through the target nucleus. The Glauber approach approximates nuclear collisions through the interactions of individual baryons with a nucleon-nucleon inelastic cross-section $\sigma_{in}$ [20, 87, 88, 177]. This method characterizes nuclear collisions with several geometrically dependent quantities. Here we will briefly discuss some of the more common quantities used throughout this work.

As we will develop in this Appendix, in nucleus-nucleus collisions, the number of nucleons that suffer inelastic collisions depends largely on the impact parameter $\vec{b}$ of the collisions. The impact parameter is defined as the transverse separation of the centers of the colliding nuclei as shown in Fig.B.1. Experimentally this parameter cannot be directly measured, however a Zero Degree Calorimeter positioned on the beam axis can measure the energy of the nucleons that did not participate in the collisions called "spectators". "Participant" nucleons are those that suffer at least one inelastic scattering during the collision. They are also called "wounded" nucleons

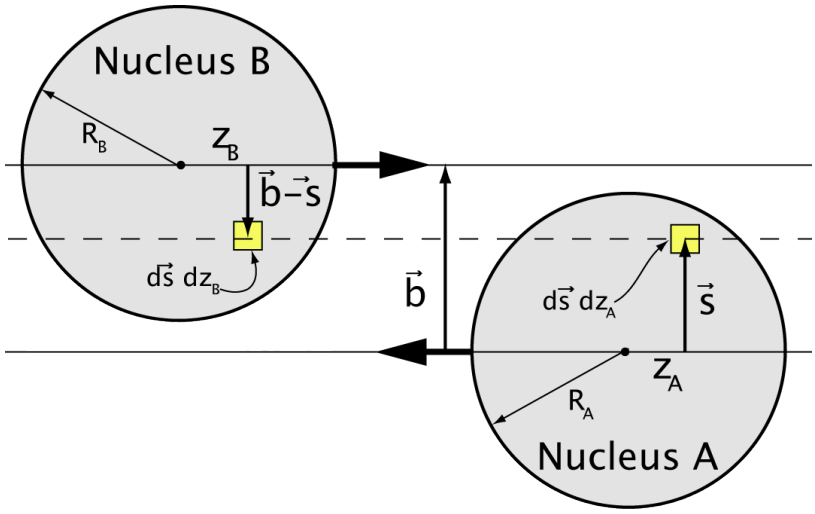


Figure B.1: A geometrical description of Nucleus-Nucleus collisions.

since they fragment into secondary particles after the collision. Wounded nucleons do not make it to the Zero Degree Calorimeter as baryons, so the measurement of spectators is related to the centrality of the collision.

As is briefly discussed in Ch.(4), the observed total multiplicity of hadrons produced in nuclear collisions is related to the number of participants, $N_{part}$, as well as number of binary nucleon-nucleon collisions, $N_{coll}$. For this reason, it is common to study emerging phenomenon as functions of centrality via $N_{part}$ and $N_{coll}$.

We would like to calculate the probability of inelastic baryon-baryon collisions (with cross section $\sigma_{in}$) given the densities and overlap regions of the nuclei. The probability of finding a baryon in nucleus A within the volume element $d\vec{s}\, dz_{_A}$ is $\rho_{_A}(s, z_{_A})$, normalized so that

$$\int \rho_{_A}(\vec{s}, z_{_A}) d\vec{s}\, dz_{_A} = A, \tag{B.1}$$

where A is the number of baryons in the nucleus. We take a Woods-Saxon density profile of nucleons in a nucleus

$$\rho_{_A}(r) = \frac{\rho_0}{1 + e^{(r-\langle r\rangle)/\epsilon}} \tag{B.2}$$

where $\langle r \rangle$ is the average nuclear radius, $\epsilon = 0.545$ controls the sharpness of the edges of the nucleus, and $\rho_0$ is the density normalization factor. The elemental probability $dP$ that a baryon found in the volume element $d\vec{s}\, dz_{_A}$ at position $(\vec{s}, z_{_A})$ of nucleus A will have a collision with a baryon in nucleus B found in the volume $d\vec{s}\, dz_{_B}$ at the position $(|\vec{b} - \vec{s}|, z_{_B})$ is

$$dP = \frac{\rho_{_A}(\vec{s}, z_{_A})}{A} \frac{\rho_{_B}(|\vec{b} - \vec{s}|, z_{_B})}{B} \sigma_{in}\ d\vec{s}\, dz_{_A}\ dz_{_B}, \tag{B.3}$$

where $\sigma_{in}$ is the cross section for an inelastic collision.

It is convenient to write the thickness function of nucleus A as

$$T_{_A}(\vec{s}) = \int \rho_{_A}(\vec{s}, z_{_A})\ dz_{_A} \tag{B.4}$$

where

$$\int T_{_A}(s) d^2 s = A \tag{B.5}$$

and similarly for nucleus B. The total probability for a baryon-baryon collision at impact parameter $\vec{b}$ is $\sigma_{in} T_{_{AB}}(\vec{b})/AB$ where

$$T_{_{AB}}(\vec{b}) = \int T_{_A}(s) T_{_B}(|\vec{b} - \vec{s}|) d^2 s\ dz_{_A}\ dz_{_B}, \tag{B.6}$$

with

$$\int T_{_{AB}}(b) d^2 b = AB. \tag{B.7}$$

We can always change our view of the collision so that $\vec{b}$ aligns with the $\hat{x}$ direction and so from now on, we will take $\vec{b} \to b$.

With the thickness functions and $T_{_{AB}}$, we can write down the probability for

exactly $n$ baryon-baryon collisions at an impact parameter $b$ as

$$P(n,b) = \left( \begin{array}{c} AB \\ n \end{array} \right) \left[ \frac{T_{_{AB}}(b)\sigma_{in}}{AB} \right]^n \left[ 1 - \frac{T_{_{AB}}(b)\sigma_{in}}{AB} \right]^{AB-n}, \tag{B.8}$$

where the first factor on the right hand side is the number of combinations for finding $n$ out of $AB$ possible collisions

$$\left( \begin{array}{c} AB \\ n \end{array} \right) = \frac{(AB)!}{n!(AB-n)!}. \tag{B.9}$$

The second factor is the probability of exactly $n$ baryon-baryon collisions and the third factor is the probability of exactly $AB - n$ misses. From this, we can find the total probability of an inelastic event during the collision of nucleus A with nucleus B at impact parameter $b$. This probability is the sum of (B.8) from $n = 1$ to $n = AB$ as follows,

$$\frac{d\sigma_{in}^{AB}}{d^2b} = \sum_{n=1}^{AB} P(n,b) = 1 - \left[ 1 - \frac{T_{_{AB}}(b)\sigma_{in}}{AB} \right]^{AB}, \tag{B.10}$$

and the total cross section is then

$$\sigma_{in}^{AB} = \int \left( 1 - \left[ 1 - \frac{T_{_{AB}}(b)\sigma_{in}}{AB} \right]^{AB} \right) \, d^2b. \tag{B.11}$$

Also, the average number of nucleon-nucleon collisions, $N_{coll}$, is then

$$N_{coll}(b) = T_{_{AB}}(b)\sigma_{in}. \tag{B.12}$$

Since it is possible for each nucleon to suffer zero, one, or more collisions during its travel through the opposing nucleus, it is also interesting to know the total number of nucleons that (participate) have at least one inelastic collision for a given impact parameter. Let us first assume a p+A collision and find the number of collisions.

Now B=1 and (B.8) reduces to

$$P_{_{pA}}(n,b) = \left( \begin{array}{c} A \\ n \end{array} \right) \left[\frac{T_{_A}(b)\sigma_{in}}{A}\right]^n \left[1 - \frac{T_{_A}(b)\sigma_{in}}{A}\right]^{A-n}, \tag{B.13}$$

which is the probability of the proton having $n$ inelastic events with a "row" ($T_{_A}(b)$) of nucleons in nucleus A. We have the probability of any event as

$$\frac{d\sigma_{in}^{pA}}{d^2b} = \sum_{n=1}^{A} P_{_{pA}}(n,b) = 1 - \left[1 - \frac{T_{_A}(b)\sigma_{in}}{A}\right]^A \approx 1 - e^{-\sigma_{in}T_{_A}(b)}. \tag{B.14}$$

Now instead of a single proton, we imagine a row of nucleons intersecting the same row in nucleus A. To find the probability of a collision for this scenario, we need only multiply (B.14) by the number of nucleons in the incoming row, $T_{_B}(|b-s|)$, and find $T_{_B}(|b-s|)[1-\exp(-\sigma_{in}T_{_A}(b))]$. The same idea follows for a row of nucleons in nucleus A intersecting nucleus B. The number of nucleons participating in the collision is then

$$N_{part}(b) = \int d^2s \left[T_{_A}(s)\left(1 - e^{-\sigma_{in}T_{_B}(|b-s|)}\right) + T_{_B}(|b-s|)\left(1 - e^{-\sigma_{in}T_{_A}(s)}\right)\right]. \tag{B.15}$$

We can also calculate the average density of participants. Equation (B.15) has two terms in the integrand, the number of nucleons in nucleus A that participate in collisions with nucleus B, and vice versa. Since these values are found from nucleon densities we can write (B.15) in the terms $n_{part}(b,s) = n_{part,_A}(b,s) + n_{part,_B}(b,s)$ where $n_{part,_A}(b,s) = T_{_A}(s)(1 - \exp[-\sigma_{in}T_{_B}(|b-s|)])$, and $n_{part,_B}(b,s) = T_{_B}(|b-s|)(1 - \exp[-\sigma_{in}T_{_A}(s)])$, such that $\int n_{part}(b,s)d^2s = N_{part}(b)$. With these definitions we can calculate the average density of participants in nucleus A as

$$\rho_{part}(b) = \frac{\int d^2s\ n_{part,_A}(b,s)\ n_{part}(b,s)}{\int d^2s\ n_{part}(b,s)} \tag{B.16}$$

and similarly for the average density of participants in nucleus B. If A and B are

symmetric, identical nuclei, then the density of participants in A will be the same as in B. This would not be true, however, for a Monte Carlo Glauber simulation. The method presented here has smooth density distributions and adds up fractions of participants where MC simulations have individual nucleons that sometimes participate and sometimes not. Over an average of an ensemble of events, the two methods will agree.

# REFERENCES


[1] M. Daugherity, ( STAR collaboration ), "Anomalous centrality variation of minijet angular correlations in Au-Au collisions at 62 and 200 GeV from STAR," J. Phys. **G35** (2008) 104090, arXiv:0806.2121 [nucl-ex].

[2] . B. I. Abelev, ( STAR collaboration ), "Long range rapidity correlations and jet production in high energy nuclear collisions," arXiv:0909.0191 [nucl-ex].

[3] J. Putschke, "Intra-jet correlations of high-$p_t$ hadrons from STAR," J. Phys. **G34** (2007) S679–684, arXiv:nucl-ex/0701074.

[4] B. Alver et al., ( PHOBOS collaboration ), "High transverse momentum triggered correlations over a large pseudorapidity acceptance in Au+Au collisions at $\sqrt{s_{NN}} = 200GeV$," Phys. Rev. Lett. **104** (2010) 062301, arXiv:0903.2811 [nucl-ex].

[5] B. Alver et al., ( PHOBOS collaboration ), "High $p_T$ Triggered Delta-eta,Delta-phi Correlations over a Broad Range in Delta-eta," J. Phys. **G35** (2008) 104080, arXiv:0804.3038 [nucl-ex].

[6] T. Ludlam et al., "Future Science at the Relativistic Heavy Ion Collider." *DOE Scientific and Technical Information*.

[7] J. Adams et al., ( STAR collaboration ), "Evidence from d + Au measurements for final-state suppression of high p(T) hadrons in Au + Au

collisions at RHIC," Phys. Rev. Lett. **91** (2003) 072304, arXiv:nucl-ex/0306024.

[8] S. S. Adler et al., ( PHENIX collaboration ), "Identified charged particle spectra and yields in Au + Au collisions at s(NN)**(1/2) = 200-GeV," Phys. Rev. **C69** (2004) 034909, arXiv:nucl-ex/0307022.

[9] J. Adams et al., ( STAR collaboration ), "Experimental and theoretical challenges in the search for the quark gluon plasma: The STAR collaboration's critical assessment of the evidence from RHIC collisions," Nucl. Phys. **A757** (2005) 102–183, arXiv:nucl-ex/0501009.

[10] T. Ludlam and L. McLerran, "What have we learned from the Relativistic Heavy Ion Collider?," Phys. Today **56N10** (2003) 48–54.

[11] L. McLerran, "The Color Glass Condensate and Glasma," arXiv:0804.1736 [hep-ph].

[12] J. Breitweg et al., ( ZEUS collaboration ), "ZEUS results on the measurement and phenomenology of F2 at low x and low Q**2," Eur. Phys. J. **C7** (1999) 609–630, arXiv:hep-ex/9809005.

[13] L. McLerran, "Theoretical Concepts for Ultra-Relativistic Heavy Ion Collisions," arXiv:0911.2987 [hep-ph].

[14] L. McLerran, "Gluon Saturation and the Formation Stage of Heavy Ion Collisions," arXiv:0807.4095 [hep-ph].

[15] L. McLerran, "RHIC physics: The quark gluon plasma and the color glass condensate: 4 lectures," arXiv:hep-ph/0311028.

[16] D. Kharzeev and E. Levin, "Manifestations of high density QCD in the first RHIC data," Phys. Lett. **B523** (2001) 79–87, arXiv:nucl-th/0108006.

[17] B. B. Back et al., "The significance of the fragmentation region in ultrarelativistic heavy ion collisions," Phys. Rev. Lett. **91** (2003) 052303, arXiv:nucl-ex/0210015.

[18] L. McLerran, "A Brief Introduction to the Color Glass Condensate and the Glasma," arXiv:0812.4989 [hep-ph].

[19] D. Kharzeev and M. Nardi, "Hadron production in nuclear collisions at RHIC and high density QCD," Phys. Lett. **B507** (2001) 121–128, arXiv:nucl-th/0012025.

[20] D. Kharzeev, E. Levin, and M. Nardi, "Color glass condensate at the LHC: Hadron multiplicities in p p, p A and A A collisions," Nucl. Phys. **A747** (2005) 609–629, arXiv:hep-ph/0408050.

[21] T. Hirano and Y. Nara, "Hydrodynamic afterburner for the color glass condensate and the parton energy loss," Nucl. Phys. **A743** (2004) 305–328, arXiv:nucl-th/0404039.

[22] S. Eidelman et al., ( Particle Data Group collaboration ), "Review of particle physics," Phys. Lett. **B592** (2004) 1.

[23] B. B. Back et al., ( PHOBOS collaboration ), "Charged particle multiplicity near mid-rapidity in central Au + Au collisions at $S^{(1/2)}$ = 56-A/GeV and 130- A/GeV," Phys. Rev. Lett. **85** (2000) 3100–3104, arXiv:hep-ex/0007036.

[24] N. Armesto and C. Pajares, "Central rapidity densities of charged particles at RHIC and LHC," Int. J. Mod. Phys. **A15** (2000) 2019–2052, arXiv:hep-ph/0002163.

[25] A. Dumitru, F. Gelis, L. McLerran, and R. Venugopalan, "Glasma flux tubes

and the near side ridge phenomenon at RHIC," Nucl. Phys. **A810** (2008) 91, arXiv:0804.3858 [hep-ph].

[26] L. C. De Silva, ( STAR collaboration ), "Evolution of structures in two particle correlations in RHIC Cu+Cu collisions as a function of centrality and momentum," arXiv:0910.5938 [nucl-ex].

[27] A. Kiyomichi, Study of identified hadron spectra and yields at mid- rapidity in s(NN)**(1/2) = 200-GeV Au + Au collisions. PhD thesis, 2005.

[28] J. Adams et al., ( STAR collaboration ), "Transverse-momentum p(t) correlations on (eta,Phi) from mean-p(t) fluctuations in Au - Au collisions at s(NN)**(1/2) = 200-GeV," J. Phys. **G32** (2006) L37–L48, arXiv:nucl-ex/0509030.

[29] J. L. Nagle, "Ridge, Bulk, and Medium Response: How to Kill Models and Learn Something in the Process," arXiv:0907.2707 [nucl-ex].

[30] I. Arsene et al., ( BRAHMS collaboration ), "Quark Gluon Plasma an Color Glass Condensate at RHIC? The perspective from the BRAHMS experiment," Nucl. Phys. **A757** (2005) 1–27, arXiv:nucl-ex/0410020.

[31] B. B. Back et al., ( PHOBOS collaboration ), "The PHOBOS perspective on discoveries at RHIC," Nucl. Phys. **A757** (2005) 28–101, arXiv:nucl-ex/0410022.

[32] K. Adcox et al., ( PHENIX collaboration ), "Formation of dense partonic matter in relativistic nucleus nucleus collisions at RHIC: Experimental evaluation by the PHENIX collaboration," Nucl. Phys. **A757** (2005) 184–283, arXiv:nucl-ex/0410003.

[33] T. J. Tarnowsky, "Long-Range Multiplicity Correlations in Relativistic Heavy Ion Collisions as a Signal for Dense Partonic Matter," arXiv:0807.1941 [nucl-ex].

[34] S. Haussler, M. Abdel-Aziz, and M. Bleicher, "Forward-backward charge fluctuations at RHIC energies," AIP Conf. Proc. **881** (2007) 263–266.

[35] T. Lappi and L. McLerran, "Long range rapidity correlations as seen in the STAR experiment," arXiv:0909.0428 [hep-ph].

[36] S. Gavin, L. McLerran, and G. Moschelli, "Long Range Correlations and the Soft Ridge in Relativistic Nuclear Collisions," Phys. Rev. **C79** (2009) 051902, arXiv:0806.4718 [nucl-th].

[37] G. Moschelli and S. Gavin, "Soft Contribution to the Hard Ridge in Relativistic Nuclear Collisions," Nucl. Phys. **A836** (2010) 43–58, arXiv:0910.3590 [nucl-th].

[38] S. Gavin and M. Abdel-Aziz, "Measuring Shear Viscosity Using Transverse Momentum Correlations in Relativistic Nuclear Collisions," Phys. Rev. Lett. **97** (2006) 162302, arXiv:nucl-th/0606061.

[39] S. Gavin and G. Moschelli, "Viscosity and the Soft Ridge at RHIC," J. Phys. **G35** (2008) 104084, arXiv:0806.4366 [nucl-th].

[40] S. A. Voloshin, A. M. Poskanzer, and R. Snellings, "Collective phenomena in non-central nuclear collisions," arXiv:0809.2949 [nucl-ex].

[41] I. Arsene et al., ( BRAHMS collaboration ), "Transverse momentum spectra in Au + Au and d + Au collisions at s(NN)**(1/2) = 200-GeV and the pseudorapidity dependence of high p(T) suppression," Phys. Rev. Lett. **91** (2003) 072305, arXiv:nucl-ex/0307003.

[42] C. Adler et al., ( STAR collaboration ), "Disappearance of back-to-back high $p_T$ hadron correlations in central Au+Au collisions at $\sqrt{s_{NN}}$ = 200-GeV," Phys. Rev. Lett. **90** (2003) 082302, arXiv:nucl-ex/0210033.

[43] S. S. Adler et al., ( PHENIX collaboration ), "Absence of suppression in particle production at large transverse momentum in s(NN)**(1/2) = 200-GeV d + Au collisions," Phys. Rev. Lett. **91** (2003) 072303, arXiv:nucl-ex/0306021.

[44] B. B. Back et al., ( PHOBOS collaboration ), "Centrality dependence of charged hadron transverse momentum spectra in d + Au collisions at s(NN)**(1/2) = 200-GeV," Phys. Rev. Lett. **91** (2003) 072302, arXiv:nucl-ex/0306025.

[45] G. Sterman, "Partons, factorization and resummation," arXiv:hep-ph/9606312.

[46] J. C. Collins, D. E. Soper, and G. F. Sterman, "Factorization of Hard Processes in QCD," Adv. Ser. Direct. High Energy Phys. **5** (1988) 1–91, arXiv:hep-ph/0409313.

[47] J.-w. Qiu and G. F. Sterman, "QCD and rescattering in nuclear targets," Int. J. Mod. Phys. **E12** (2003) 149, arXiv:hep-ph/0111002.

[48] C. Nattrass, "Energy and system dependence of high-$p_T$ triggered two-particle near-side correlations," Eur. Phys. J. **C62** (2009) 265–269, arXiv:0809.5261 [nucl-ex].

[49] C. Nattrass, "System and energy dependence of strange and non-strange particle correlations in STAR at RHIC," arXiv:0804.4683 [nucl-ex].

[50] C. E. Nattrass, "System size dependence of strange particle correlations in Cu+Cu and Au+Au collisions at $\sqrt{s_{NN}}$ = 200 GeV in STAR at RHIC," J. Phys. **G35** (2008) 044063, arXiv:0804.4558 [nucl-ex].

[51] M. Daugherity, ( STAR collaboration ), "Angular correlations in STAR," PoS **CFRNC2006** (2006) 005, arXiv:nucl-ex/0611032.

[52] J. Adams et al., ( STAR collaboration ), "Transverse momentum and collision energy dependence of high p(T) hadron suppression in Au + Au collisions at ultrarelativistic energies," Phys. Rev. Lett. **91** (2003) 172302, arXiv:nucl-ex/0305015.

[53] J. Adams et al., ( STAR collaboration ), "Minijet deformation and charge-independent angular correlations on momentum subspace (eta, phi) in Au-Au collisions at s(NN)**(1/2) = 130-GeV," Phys. Rev. **C73** (2006) 064907, arXiv:nucl-ex/0411003.

[54] J. Adams et al., ( STAR collaboration ), "Incident energy dependence of p(t) correlations at RHIC," Phys. Rev. **C72** (2005) 044902, arXiv:nucl-ex/0504031.

[55] D. Adamova et al., ( CERES collaboration ), "Scale-dependence of transverse momentum correlations in Pb-Au collisions at 158A GeV/c," Nucl. Phys. **A811** (2008) 179–196, arXiv:0803.2407 [nucl-ex].

[56] L. D. McLerran and R. Venugopalan, "Computing quark and gluon distribution functions for very large nuclei," Phys. Rev. **D49** (1994) 2233–2241, arXiv:hep-ph/9309289.

[57] L. D. McLerran and R. Venugopalan, "Gluon distribution functions for very large nuclei at small transverse momentum," Phys. Rev. **D49** (1994) 3352–3355, arXiv:hep-ph/9311205.

[58] T. Lappi and L. McLerran, "Some features of the glasma," Nucl. Phys. **A772** (2006) 200–212, arXiv:hep-ph/0602189.

[59] K. Dusling, F. Gelis, T. Lappi, and R. Venugopalan, "Long range two-particle rapidity correlations in A+A collisions from high energy QCD evolution," arXiv:0911.2720 [hep-ph].

[60] S. A. Voloshin, "Transverse radial expansion in nuclear collisions and two particle correlations," Phys. Lett. **B632** (2006) 490–494, arXiv:nucl-th/0312065.

[61] K. Dusling, D. Fernandez-Fraile, and R. Venugopalan, "Three-particle correlation from glasma flux tubes," Nucl. Phys. **A828** (2009) 161–177, arXiv:0902.4435 [nucl-th].

[62] S. J. Lindenbaum and R. S. Longacre, "Parton bubble model for two-particle angular correlations at RHIC/LHC," Eur. Phys. J. **C49** (2007) 767–782.

[63] P. Sorensen, "Interpreting Near-side Correlations," arXiv:0811.2959 [nucl-ex].

[64] T. Peitzmann, "The ridge laboratory," arXiv:0903.5281 [nucl-th].

[65] J. Takahashi et al., "Topology studies of hydrodynamics using two particle correlation analysis," Phys. Rev. Lett. **103** (2009) 242301, arXiv:0902.4870 [nucl-th].

[66] C. A. Pruneau, S. Gavin, and S. A. Voloshin, "Transverse Radial Flow Effects on Two- and Three-Particle Angular Correlations," Nucl. Phys. **A802** (2008) 107–121, arXiv:0711.1991 [nucl-ex].

[67] N. Armesto, C. A. Salgado, and U. A. Wiedemann, "Measuring the collective flow with jets," Phys. Rev. Lett. **93** (2004) 242301, arXiv:hep-ph/0405301.

[68] P. Romatschke, "Momentum broadening in an anisotropic plasma," Phys. Rev. **C75** (2007) 014901, arXiv:hep-ph/0607327.

[69] A. Majumder, B. Muller, and S. A. Bass, "Longitudinal Broadening of Quenched Jets in Turbulent Color Fields," Phys. Rev. Lett. **99** (2007) 042301, arXiv:hep-ph/0611135.

[70] C. B. Chiu and R. C. Hwa, "Pedestal and peak structure in jet correlation," Phys. Rev. **C72** (2005) 034903, arXiv:nucl-th/0505014.

[71] R. C. Hwa, "Hadron Correlations in Jets and Ridges through Parton Recombination," arXiv:0904.2159 [nucl-th].

[72] A. Dumitru, Y. Nara, B. Schenke, and M. Strickland, "Jet broadening in unstable non-Abelian plasmas," Phys. Rev. **C78** (2008) 024909, arXiv:0710.1223 [hep-ph].

[73] C.-Y. Wong, "Ridge Structure associated with the Near-Side Jet in the (Delta phi)-(Delta eta) Correlation," Phys. Rev. **C76** (2007) 054908, arXiv:0707.2385 [hep-ph].

[74] R. Mizukawa, T. Hirano, M. Isse, Y. Nara, and A. Ohnishi, "Search for a Ridge Structure Origin with Shower Broadening and Jet Quenching," J. Phys. **G35** (2008) 104083, arXiv:0805.2795 [nucl-th].

[75] C.-Y. Wong, "Momentum Kick Model Analysis of PHENIX Near-Side Ridge Data and Photon Jet," Phys. Rev. **C80** (2009) 034908, arXiv:0901.0726 [hep-ph].

[76] C.-Y. Wong, "The Momentum Kick Model Description of the Near-Side Ridge and Jet Quenching," Phys. Rev. **C78** (2008) 064905, arXiv:0806.2154 [hep-ph].

[77] V. S. Pantuev, "'Jet-Ridge' effect in heavy ion collisions as a back splash from stopped parton," arXiv:0710.1882 [hep-ph].

[78] T. A. Trainor, "The RHIC azimuth quadrupole: 'perfect liquid' or gluonic radiation?," Mod. Phys. Lett. **A23** (2008) 569–589, arXiv:0708.0792 [hep-ph].

[79] E. V. Shuryak, "On the Origin of the 'Ridge' phenomenon induced by Jets in Heavy Ion Collisions," Phys. Rev. **C76** (2007) 047901, arXiv:0706.3531 [nucl-th].

[80] C. Amsler et al., ( Particle Data Group collaboration ), "Review of particle physics," Phys. Lett. **B667** (2008) 1.

[81] J. D. Bjorken, "Highly Relativistic Nucleus-Nucleus Collisions: The Central Rapidity Region," Phys. Rev. **D27** (1983) 140–151.

[82] F. Karsch, "Lattice QCD at high temperature and density," Lect. Notes Phys. **583** (2002) 209–249, arXiv:hep-lat/0106019.

[83] F. Karsch, "Lattice results on QCD thermodynamics," Nucl. Phys. **A698** (2002) 199–208, arXiv:hep-ph/0103314.

[84] F. Karsch, "News from lattice QCD on heavy quark potentials and spectral functions of heavy quark states," J. Phys. **G30** (2004) S887–S894, arXiv:hep-lat/0403016.

[85] T. Matsui and H. Satz, "J/psi Suppression by Quark-Gluon Plasma Formation," Phys. Lett. **B178** (1986) 416.

[86] J. Rafelski and B. Muller, "Strangeness Production in the Quark - Gluon Plasma," Phys. Rev. Lett. **48** (1982) 1066.

[87] C.-Y. Wong, Introduction to High-Energy Heavy-Ion Collisions. World Scientific, New Jersey, 1994.

[88] R. Vogt, Ultrarelativistic Heavy-Ion Collisions. Elsevier Science B.V., Amsterdam, 2007.

[89] S. Voloshin and Y. Zhang, "Flow study in relativistic nuclear collisions by Fourier expansion of Azimuthal particle distributions," Z. Phys. **C70** (1996) 665–672, arXiv:hep-ph/9407282.

[90] D. Teaney, "Effect of shear viscosity on spectra, elliptic flow, and Hanbury Brown-Twiss radii," Phys. Rev. **C68** (2003) 034913, arXiv:nucl-th/0301099.

[91] D. A. Teaney, "Viscosity and thermalization," J. Phys. **G30** (2004) S1247–S1250, arXiv:nucl-th/0403053.

[92] M. Luzum and P. Romatschke, "Conformal Relativistic Viscous Hydrodynamics: Applications to RHIC results at $\sqrt{(}s_{NN}) = 200GeV$," Phys. Rev. **C78** (2008) 034915, arXiv:0804.4015 [nucl-th].

[93] M. Luzum, J. G. Cramer, and G. A. Miller, "Understanding the Optical Potential in HBT Interferometry," Phys. Rev. **C78** (2008) 054905, arXiv:0809.0520 [nucl-th].

[94] M. Luzum and G. A. Miller, "Elliptic flow from final state interactions in the DWEF model," Phys. Rev. **C79** (2009) 024902, arXiv:0810.1550 [nucl-th].

[95] M. Luzum and P. Romatschke, "Viscous Hydrodynamic Predictions for Nuclear Collisions at the LHC," Phys. Rev. Lett. **103** (2009) 262302, arXiv:0901.4588 [nucl-th].

[96] M. Luzum, "Relativistic Heavy Ion Collisions: Viscous Hydrodynamic Simulations and Final State Interactions," arXiv:0908.4100 [nucl-th].

[97] N. K. Pruthi, ( STAR collaboration ), "Elliptic flow and the high $p_T$ ridge in Au+Au collisions," Eur. Phys. J. **C62** (2009) 165–167, arXiv:0810.3530 [nucl-ex].

[98] S. S. Adler et al., ( PHENIX collaboration ), "Centrality dependence of direct photon production in s(NN)**(1/2) = 200-GeV Au + Au collisions," Phys. Rev. Lett. **94** (2005) 232301, arXiv:nucl-ex/0503003.

[99] P. J. Siemens and J. O. Rasmussen, "Evidence for a blast wave from compress nuclear matter," Phys. Rev. Lett. **42** (1979) 880–887.

[100] E. Schnedermann, J. Sollfrank, and U. W. Heinz, "Thermal phenomenology of hadrons from 200-A/GeV S+S collisions," Phys. Rev. **C48** (1993) 2462–2475, arXiv:nucl-th/9307020.

[101] F. Cooper and G. Frye, "Comment on the Single Particle Distribution in the Hydrodynamic and Statistical Thermodynamic Models of Multiparticle Production," Phys. Rev. **D10** (1974) 186.

[102] L. V. Gribov, E. M. Levin, and M. G. Ryskin, "Semihard Processes in QCD," Phys. Rept. **100** (1983) 1–150.

[103] A. H. Mueller and J.-w. Qiu, "Gluon Recombination and Shadowing at Small Values of x," Nucl. Phys. **B268** (1986) 427.

[104] J. P. Blaizot and A. H. Mueller, "The Early Stage of Ultrarelativistic Heavy Ion Collisions," Nucl. Phys. **B289** (1987) 847.

[105] L. D. McLerran and R. Venugopalan, "Green's functions in the color field of a large nucleus," Phys. Rev. **D50** (1994) 2225–2233, arXiv:hep-ph/9402335.

[106] L. D. McLerran and R. Venugopalan, "Fock space distributions, structure functions, higher twists and small x," Phys. Rev. **D59** (1999) 094002, arXiv:hep-ph/9809427.

[107] A. Ayala, J. Jalilian-Marian, L. D. McLerran, and R. Venugopalan, "Quantum corrections to the Weizsacker-Williams gluon distribution function at small x," Phys. Rev. **D53** (1996) 458–475, arXiv:hep-ph/9508302.

[108] E. Iancu and L. D. McLerran, "Saturation and universality in QCD at small x," Phys. Lett. **B510** (2001) 145–154, arXiv:hep-ph/0103032.

[109] Y. V. Kovchegov, "Non-Abelian Weizsaecker-Williams field and a two-dimensional effective color charge density for a very large nucleus," Phys. Rev. **D54** (1996) 5463–5469, arXiv:hep-ph/9605446.

[110] A. Krasnitz and R. Venugopalan, "The initial energy density of gluons produced in very high energy nuclear collisions," Phys. Rev. Lett. **84** (2000) 4309–4312, arXiv:hep-ph/9909203.

[111] E. Levin and K. Tuchin, "Solution to the evolution equation for high parton density QCD," Nucl. Phys. **B573** (2000) 833–852, arXiv:hep-ph/9908317.

[112] I. Balitsky, "Operator expansion for high-energy scattering," Nucl. Phys. **B463** (1996) 99–160, arXiv:hep-ph/9509348.

[113] Y. V. Kovchegov, "Small-x F2 structure function of a nucleus including multiple pomeron exchanges," Phys. Rev. **D60** (1999) 034008, arXiv:hep-ph/9901281.

[114] E. Iancu, A. Leonidov, and L. D. McLerran, "Nonlinear gluon evolution in the color glass condensate. I," Nucl. Phys. **A692** (2001) 583–645, arXiv:hep-ph/0011241.

[115] E. Ferreiro, E. Iancu, A. Leonidov, and L. McLerran, "Nonlinear gluon evolution in the color glass condensate. II," Nucl. Phys. **A703** (2002) 489–538, arXiv:hep-ph/0109115.

[116] D. Kharzeev, E. Levin, and M. Nardi, "The onset of classical QCD dynamics in relativistic heavy ion collisions," Phys. Rev. **C71** (2005) 054903, arXiv:hep-ph/0111315.

[117] D. Kharzeev, E. Levin, and L. McLerran, "Parton saturation and N(part) scaling of semi-hard processes in QCD," Phys. Lett. **B561** (2003) 93–101, arXiv:hep-ph/0210332.

[118] D. Kharzeev, Y. V. Kovchegov, and K. Tuchin, "Cronin effect and high-p(T) suppression in p A collisions," Phys. Rev. **D68** (2003) 094013, arXiv:hep-ph/0307037.

[119] D. Kharzeev, Y. V. Kovchegov, and K. Tuchin, "Nuclear modification factor in d + Au collisions: Onset of suppression in the color glass condensate," Phys. Lett. **B599** (2004) 23–31, arXiv:hep-ph/0405045.

[120] M. Froissart, "Asymptotic behavior and subtractions in the Mandelstam representation," Phys. Rev. **123** (1961) 1053–1057.

[121] J. Jalilian-Marian, A. Kovner, L. D. McLerran, and H. Weigert, "The intrinsic glue distribution at very small x," Phys. Rev. **D55** (1997) 5414–5428, arXiv:hep-ph/9606337.

[122] A. H. Mueller, "Parton saturation at small x and in large nuclei," Nucl. Phys. **B558** (1999) 285–303, arXiv:hep-ph/9904404.

[123] Y. V. Kovchegov, "Quantum structure of the non-Abelian

Weizsaecker-Williams field for a very large nucleus," Phys. Rev. **D55** (1997) 5445–5455, arXiv:hep-ph/9701229.

[124] V. A. Khoze, A. D. Martin, M. G. Ryskin, and W. J. Stirling, "The spread of the gluon k(t)-distribution and the determination of the saturation scale at hadron colliders in resummed NLL BFKL," Phys. Rev. **D70** (2004) 074013, arXiv:hep-ph/0406135.

[125] F. Gelis, A. M. Stasto, and R. Venugopalan, "Limiting fragmentation in hadron hadron collisions at high energies," Eur. Phys. J. **C48** (2006) 489–500, arXiv:hep-ph/0605087.

[126] A. Kovner, L. D. McLerran, and H. Weigert, "Gluon production at high transverse momentum in the McLerran-Venugopalan model of nuclear structure functions," Phys. Rev. **D52** (1995) 3809–3814, arXiv:hep-ph/9505320.

[127] A. Kovner, L. D. McLerran, and H. Weigert, "Gluon production from nonAbelian Weizsacker-Williams fields in nucleus-nucleus collisions," Phys. Rev. **D52** (1995) 6231–6237, arXiv:hep-ph/9502289.

[128] A. Krasnitz and R. Venugopalan, "Non-perturbative computation of gluon mini-jet production in nuclear collisions at very high energies," Nucl. Phys. **B557** (1999) 237, arXiv:hep-ph/9809433.

[129] T. Lappi, "Production of gluons in the classical field model for heavy ion collisions," Phys. Rev. **C67** (2003) 054903, arXiv:hep-ph/0303076.

[130] E. Iancu, K. Itakura, and L. McLerran, "Geometric scaling above the saturation scale," Nucl. Phys. **A708** (2002) 327–352, arXiv:hep-ph/0203137.

[131] A. H. Mueller and D. N. Triantafyllopoulos, "The energy dependence of the saturation momentum," Nucl. Phys. **B640** (2002) 331–350, arXiv:hep-ph/0205167.

[132] D. N. Triantafyllopoulos, "The energy dependence of the saturation momentum from RG improved BFKL evolution," Nucl. Phys. **B648** (2003) 293–316, arXiv:hep-ph/0209121.

[133] M. Gyulassy and L. D. McLerran, "Yang-Mills radiation in ultrarelativistic nuclear collisions," Phys. Rev. **C56** (1997) 2219–2228, arXiv:nucl-th/9704034.

[134] Y. V. Kovchegov and D. H. Rischke, "Classical gluon radiation in ultrarelativistic nucleus nucleus collisions," Phys. Rev. **C56** (1997) 1084–1094, arXiv:hep-ph/9704201.

[135] A. Krasnitz and R. Venugopalan, "The initial gluon multiplicity in heavy ion collisions," Phys. Rev. Lett. **86** (2001) 1717–1720, arXiv:hep-ph/0007108.

[136] A. Krasnitz, Y. Nara, and R. Venugopalan, "Coherent gluon production in very high energy heavy ion collisions," Phys. Rev. Lett. **87** (2001) 192302, arXiv:hep-ph/0108092.

[137] D. Kharzeev, R. D. Pisarski, and M. H. G. Tytgat, "Possibility of spontaneous parity violation in hot QCD," Phys. Rev. Lett. **81** (1998) 512–515, arXiv:hep-ph/9804221.

[138] D. Kharzeev, R. D. Pisarski, and M. H. G. Tytgat, "Parity odd bubbles in hot QCD," arXiv:hep-ph/9808366.

[139] D. E. Kharzeev, R. D. Pisarski, and M. H. G. Tytgat, "Aspects of parity, CP, and time reversal violation in hot QCD," arXiv:hep-ph/0012012.

[140] D. Kharzeev, A. Krasnitz, and R. Venugopalan, "Anomalous chirality fluctuations in the initial stage of heavy ion collisions and parity odd bubbles," Phys. Lett. **B545** (2002) 298–306, arXiv:hep-ph/0109253.

[141] D. E. Kharzeev, L. D. McLerran, and H. J. Warringa, "The effects of topological charge change in heavy ion collisions: 'Event by event P and CP violation'," Nucl. Phys. **A803** (2008) 227–253, arXiv:0711.0950 [hep-ph].

[142] K. Fukushima, D. E. Kharzeev, and H. J. Warringa, "The Chiral Magnetic Effect," Phys. Rev. **D78** (2008) 074033, arXiv:0808.3382 [hep-ph].

[143] Y. V. Kovchegov, "Classical initial conditions for ultrarelativistic heavy ion collisions," Nucl. Phys. **A692** (2001) 557–582, arXiv:hep-ph/0011252.

[144] A. H. Mueller, "Toward equilibration in the early stages after a high energy heavy ion collision," Nucl. Phys. **B572** (2000) 227–240, arXiv:hep-ph/9906322.

[145] A. D. Martin, R. G. Roberts, W. J. Stirling, and R. S. Thorne, "Estimating the effect of NNLO contributions on global parton analyses," Eur. Phys. J. **C18** (2000) 117–126, arXiv:hep-ph/0007099.

[146] K. J. Golec-Biernat and M. Wusthoff, "Saturation effects in deep inelastic scattering at low Q**2 and its implications on diffraction," Phys. Rev. **D59** (1999) 014017, arXiv:hep-ph/9807513.

[147] K. J. Golec-Biernat and M. Wusthoff, "Saturation in diffractive deep inelastic scattering," Phys. Rev. **D60** (1999) 114023, arXiv:hep-ph/9903358.

[148] A. M. Stasto, K. J. Golec-Biernat, and J. Kwiecinski, "Geometric scaling for the total gamma* p cross-section in the low x region," Phys. Rev. Lett. **86** (2001) 596–599, arXiv:hep-ph/0007192.

[149] B. B. Back et al., ( PHOBOS collaboration ), "Charged particle pseudorapidity density distributions from Au+Au collisions at $\sqrt{s_{NN}}$ = 130-GeV," Phys. Rev. Lett. **87** (2001) 102303, arXiv:nucl-ex/0106006.

[150] F. Abe et al., ( CDF collaboration ), "Pseudorapidity distributions of charged particles produced in $\bar{p}p$ interactions at $\sqrt{s} = 630$ GeV and 1800 GeV," Phys. Rev. **D41** (1990) 2330.

[151] D. Kettler, ( STAR collaboration ), "Universal centrality and collision energy trends for v(2) measurements from 2D angular correlations," Eur. Phys. J. **C62** (2009) 175–181.

[152] C. Pruneau, S. Gavin, and S. Voloshin, "Methods for the study of particle production fluctuations," Phys. Rev. **C66** (2002) 044904, arXiv:nucl-ex/0204011.

[153] S. Gavin and M. Abdel-Aziz, "Measuring shear viscosity using correlations," Braz. J. Phys. **37** (2007) 1023–1030.

[154] M. A. Aziz and S. Gavin, "Causal diffusion and the survival of charge fluctuations in nuclear collisions," Phys. Rev. **C70** (2004) 034905, arXiv:nucl-th/0404058.

[155] L. D. Landau and E. M. Lifshitz, Fluid mechanics / by L.D. Landau and E.M. Lifshitz ; translated from the Russian by J.B. Sykes and W.H. Reid. Pergamon Press ; Addison-Wesley, London : Reading, Mass. :, 1959.

[156] Z. Xu and C. Greiner, "Thermalization of gluons in ultrarelativistic heavy ion collisions by including three-body interactions in a parton cascade," Phys. Rev. **C71** (2005) 064901, arXiv:hep-ph/0406278.

[157] Z. Xu and C. Greiner, "Elliptic flow of gluon matter in ultrarelativistic heavy-ion collisions," Phys. Rev. **C79** (2009) 014904, arXiv:0811.2940 [hep-ph].

[158] Z. Xu, L. Cheng, A. El, K. Gallmeister, and C. Greiner, "QCD Matter Thermalization at RHIC and LHC," J. Phys. **G36** (2009) 064035, arXiv:0812.3839 [hep-ph].

[159] Z. Xu and C. Greiner, "Transport rates and momentum isotropization of gluon matter in ultrarelativistic heavy-ion collisions," Phys. Rev. **C76** (2007) 024911, arXiv:hep-ph/0703233.

[160] Q.-f. Li, J. Steinheimer, H. Petersen, M. Bleicher, and H. Stocker, "Effects of a phase transition on HBT correlations in an integrated Boltzmann+Hydrodynamics approach," Phys. Lett. **B674** (2009) 111–116, arXiv:0812.0375 [nucl-th].

[161] H. Petersen, M. Bleicher, S. A. Bass, and H. Stocker, "UrQMD-2.3 - Changes and Comparisons," arXiv:0805.0567 [hep-ph].

[162] H. Petersen, J. Steinheimer, G. Burau, M. Bleicher, and H. Stocker, "A Fully Integrated Transport Approach to Heavy Ion Reactions with an Intermediate Hydrodynamic Stage," Phys. Rev. **C78** (2008) 044901, arXiv:0806.1695 [nucl-th].

[163] H. Petersen and M. Bleicher, "Eccentricity fluctuations in an integrated hybrid approach: Influence on elliptic flow," arXiv:1002.1003 [nucl-th].

[164] N. Borghini, "Multiparticle correlations from momentum conservation," Eur. Phys. J. **C30** (2003) 381–385, arXiv:hep-ph/0302139.

[165] N. Borghini, "Multiparticle correlations and momentum conservation in

nucleus-nucleus collisions," PoS **LHC07** (2007) 013, arXiv:0707.0436 [nucl-th].

[166] N. Borghini, P. M. Dinh, J.-Y. Ollitrault, A. M. Poskanzer, and S. A. Voloshin, "Effects of momentum conservation on the analysis of anisotropic flow," Phys. Rev. **C66** (2002) 014901, arXiv:nucl-th/0202013.

[167] N. Borghini, P. M. Dinh, and J.-Y. Ollitrault, "Are flow measurements at SPS reliable?," Phys. Rev. **C62** (2000) 034902, arXiv:nucl-th/0004026.

[168] N. Borghini, "Momentum conservation and correlation analyses in heavy- ion collisions at ultrarelativistic energies," Phys. Rev. **C75** (2007) 021904, arXiv:nucl-th/0612093.

[169] Z. Chajecki and M. Lisa, "Conservation Laws and the Multiplicity Evolution of Spectra at the Relativistic Heavy Ion Collider," Phys. Rev. **C79** (2009) 034908, arXiv:0807.3569 [nucl-th].

[170] Z. Chajecki and M. Lisa, "Global Conservation Laws and Femtoscopy of Small Systems," Phys. Rev. **C78** (2008) 064903, arXiv:0803.0022 [nucl-th].

[171] H. J. Drescher, S. Ostapchenko, T. Pierog, and K. Werner, "Initial condition for QGP evolution from NEXUS," Phys. Rev. **C65** (2002) 054902, arXiv:hep-ph/0011219.

[172] C. E. Aguiar, Y. Hama, T. Kodama, and T. Osada, "Event-by-event fluctuations in hydrodynamical description of heavy-ion collisions," Nucl. Phys. **A698** (2002) 639–642, arXiv:hep-ph/0106266.

[173] *Private Communication.*

[174] *Private Communication.*

[175] C. Pruneau and M. Sharma. *Talk at the Winter Workshop on Nuclear Dynamics, Ocho Rios, Jamaica, January 2-9 2010.*

[176] M. Sharma, ( STAR collaboration ), "Estimation of shear viscosity based on transverse momentum correlations," Nucl. Phys. **A830** (2009) 813c–816c, arXiv:0907.4731 [nucl-ex].

[177] D. Kharzeev, C. Lourenco, M. Nardi, and H. Satz, "A quantitative analysis of charmonium suppression in nuclear collisions," Z. Phys. **C74** (1997) 307–318, arXiv:hep-ph/9612217.

# ABSTRACT

## TWO-PARTICLE CORRELATIONS AND THE RIDGE IN RELATIVISTIC HEAVY ION COLLISIONS

by

**GEORGE MOSCHELLI**

**AUGUST 2010**

**Advisor**: Dr. Sean Gavin

**Major**: Physics

**Degree**: Doctor of Philosophy

Measurements at the Relativistic Heavy Ion Collider (RHIC) find an enhancement of two particle correlations in relativistic heavy ion collisions, not present in proton-proton collisions. Because the correlation structure is wide in relative pseudorapidity and narrow in relative azimuthal angle, it is known as the ridge. The most striking feature of the ridge is that it seems to extend to a long range in relative pseudorapidity, where causality limits interaction. Similar ridge structures are observed in correlations of particles associated with and without a jet trigger. We argue that the untriggered ridge arises when particles formed in an early Glasma stage later manifest transverse flow. We extend this study to address the triggered ridge in the same context. Finally we address the effects of shear viscosity on our correlation formalism.

# AUTOBIOGRAPHICAL STATEMENT

| | |
|---|---|
| 13 March, 1981 | Born in Warren<br>Michigan, USA |
| 1999 – 2003 | B.S. Physics<br>Lawrence Technological University<br>Southfield, Michigan, USA |
| 2003 – 2010 | Graduate Research Assistant<br>High Energy Nuclear Physics Group<br>Wayne State University<br>Detroit, MI, USA |